Theoretical and Observational Studies of Small-Scale Flares and Associated Mass Ejections / Jets

Yuji Kotani

A thesis presented for the degree of

Doctor of Science

Department of Astronomy

Kyoto University

Japan

6th January 2023

Theoretical and Observational Studies of Small-Scale Flares and Associated Mass Ejections / Jets

Yuji Kotani

Abstract

In the Sun and stars, sudden brightening phenomena (flares) and accompanying plasma eruptions have been observed on various scales. Theoretical and observational studies of a typical solar flare ($10^{29} - 10^{32}\,\mathrm{erg}$) have been performed actively. Through these studies, standard models have been developed that describe the thermodynamic and hydrodynamic response of the atmosphere during solar flares, which result from the release of magnetic energy through magnetic reconnection. In contrast, smaller flares ($10^{24} - 10^{29}\,\mathrm{erg}$) and plasma eruptions frequently occur on the Sun. These small flares have been observed in all layers of the solar atmosphere (photosphere, chromosphere, and corona) and share some qualitative properties with typical solar flares. However, it has not been fully understood, either theoretically or observationally, whether the same physical mechanisms as typical solar flares can also explain small flares on the Sun. The physical mechanisms of small flares in the Sun are of interest not only for the scale dependence of magnetic reconnection, but also as a basis for discussing the effects of heating and dynamics on the solar atmosphere. In this thesis, I have performed theoretical and observational studies to reveal the physical mechanisms underlying small flares and associated plasma ejections on the Sun, focusing on comparisons with theories of typical solar flares.

In Chapter 2, I analyzed 25 small flares in the quiet Sun of the corona, focusing on their thermodynamic properties, using imaging observations with extreme ultraviolet (EUV) and imaging spectroscopy with the Hα line. The Hα lines were observed using solar full-disk data from the Solar Dynamics Doppler Imager (SDDI) on the Solar Magnetic Activity Research Telescope (SMART) at the Hida Observatory of Kyoto University. My analysis showed that redshifts associated with Hα line-center brightening were observed in more than half of the events, corresponding to the brightening in the EUV of coronal temperatures. I also found that the emission measure and temperature in the corona derived from the EUV data are consistent with the scaling laws examined for large flares. The coronal magnetic field strength estimated from the scaling law was $5 - 15\,\mathrm{G}$, which agreed with the average magnetic field strength of the quiet Sun of the corona. Furthermore, the temperature reached a maximum value prior to the electron density in more than half of the events. These results suggest that chromospheric evaporation/condensation occurs in small flares in the quiet Sun, as is the case with typical solar flares. This study presents evidence for similarities between small and typical solar flares and suggests thermal properties and effective detection methods for nanoflares as a potential coronal heating source.

In Chapter 3, for these 25 small flares in the quiet Sun, I studied the correlation between the physical quantities of the associated cool ejections and the flare energy. I compared them with ejections at chromospheric temperature associated with larger solar/stellar flares. The results showed that the ejecta mass was roughly proportional to the 2/3 power of the flare energy. Moreover, from simple assumptions, I succeeded in theoretically deriving a scaling law that explained the power-law index. The velocity and kinetic energy of the ejecta were also correlated with the flare energy. These results provide basic quantitative relationships for understanding the nature of plasma eruptions at chromospheric temperatures associated with stellar flares. This research has potential applications in the study of the exploration of stellar flares and their associated ejecta.

In Chapter 4, I aimed at a unified understanding of the dynamics caused by magnetic reconnection in the corona, chromosphere, and photosphere. I performed the first 3D magnetohydrodynamics simulations of magnetic reconnection in an environment assuming a photosphere for this purpose. As a result, magnetic reconnection occurred as in the numerical simulation assuming a corona. However, in contrast to the coronal simulation case, a collimated flow along the ambient magnetic field (referred to as a jet) did not occur due to the interaction between the flow or shock associated with reconnection and the ambient plasma. Instead, the density increased along the elongated structure due to the slow shock formed by the reconnection. In other words, the jet-like elongated structure appeared due to shock propagation, not collimated flow. In addition, the waves generated by reconnection in this numerical simulation had enough energy to affect chromospheric heating and spicule formation. Through this study, I have established the basis for a unified view of dynamics associated with flare (magnetic reconnection) in the corona, chromosphere, and photosphere.

In Chapter 5, I summarize the properties of small flares and associated plasma ejections on the Sun obtained throughout this thesis. I also discuss them in a unified viewpoint with the large-scale flares. In addition, I discuss future prospects for solar and stellar studies based on the results of this thesis.

Supervisors: Ayumi Asai and Kazunari Shibata

Acknowledgements

Contents

List of Figures

List of Tables

General Introduction

1.1 Solar atmosphere

The solar atmosphere is the stellar atmosphere we can observe in the most detail. Many spatially resolved plasma dynamics and heating have been observed in the solar atmosphere (Sections 1.2 and 1.3). The key to these dynamics and heating is the magnetic field. Studying the solar atmosphere is important for understanding the interaction between astrophysical plasma and magnetic fields.

The solar atmosphere is divided into three main layers from the surface according to its temperature distribution: photosphere, chromosphere, and corona (Figure 1.1). The bottom photosphere corresponds to the solar surface observed in visible light and is defined as the height at which the optical thickness $\tau_{500\,\text{nm}}$ at a wavelength of $500\,\text{nm}$ equals 1.0. The typical temperature and mass density at the bottom of the photosphere are $6000\,\text{K}$ and $10^{-7}\,\text{g}\,\text{cm}^{-3}$. Since the Sun's energy source is nuclear fusion at its core, the temperature decreases with distance from the core. This continues even above the solar surface (base of the photosphere). However, the temperature gradient changes its sign at around the height of $500\,\text{km}$ from negative to positive. The layer with a positive temperature gradient just above the photosphere is called the chromosphere. The physical quantities in the chromosphere show a significant variation depending on the height. The typical temperature and density in the lower part of the layer are about $4000\,\text{K}$ and $10^{-9}\,\text{g}\,\text{cm}^{-3}$, while in the upper part, they are about $10^4\,\text{K}$ and $10^{-13}\,\text{g}\,\text{cm}^{-3}$. The corona is a layer whose temperature is about 100 times higher than the chromosphere through the transition region and is the outermost part of the solar atmosphere. The corona has a temperature of $10^6\,\text{K}$ and a density of $10^{-15}\,\text{g}\,\text{cm}^{-3}$. Active events due to magnetic fields have been observed in all these layers (Sections 1.2 and 1.3).

In the solar atmosphere, typical values of plasma β (ratio of gas pressure to magnetic pressure), in addition to temperature, significantly depend on the height (Figure 1.2).
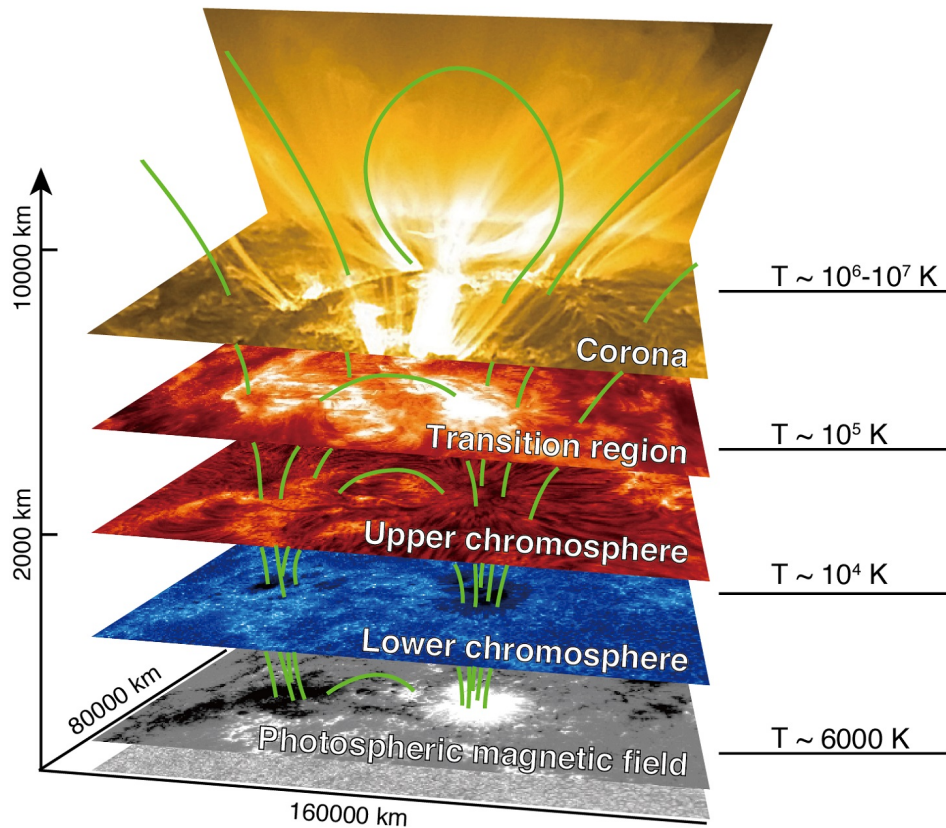
Figure 1.1: The structure of the solar atmosphere. The vertical axis indicates the height from the solar surface. The green lines indicate the magnetic field lines connected to the various layers of the solar atmosphere (from https://solar-c.nao.ac.jp/en/science.html).

Plasma β is typically greater than 1 in the photosphere and lower chromosphere in non-magnetic regions. In other words, gas pressure plays a more critical role on average in the solar photosphere and lower chromosphere. In contrast, plasma β is smaller than 1 in the upper chromosphere and corona. Thus, magnetic fields can easily affect the plasma dynamics and heating in these upper atmospheres. From the above, we can say that the effect of the magnetic field on the plasma varies with the height of the solar atmosphere.

In addition to the above three layers, the solar atmosphere is broadly divided into active regions and the quiet Sun (or quiet regions) (Figure 1.3). The distinction between active and quiet regions comes from the magnetic field strength in the region. Active regions have larger magnetic field strengths than their surroundings and exhibit bright structures in the corona. The quiet Sun refers to the area outside active regions. The highly dark areas in the corona of the quiet Sun are called coronal holes. While the typical and most energetic solar flares occur in active regions, activity due to magnetic fields can also be observed in the quiet Sun (Sections 1.2 and 1.3). These regions also exhibit different
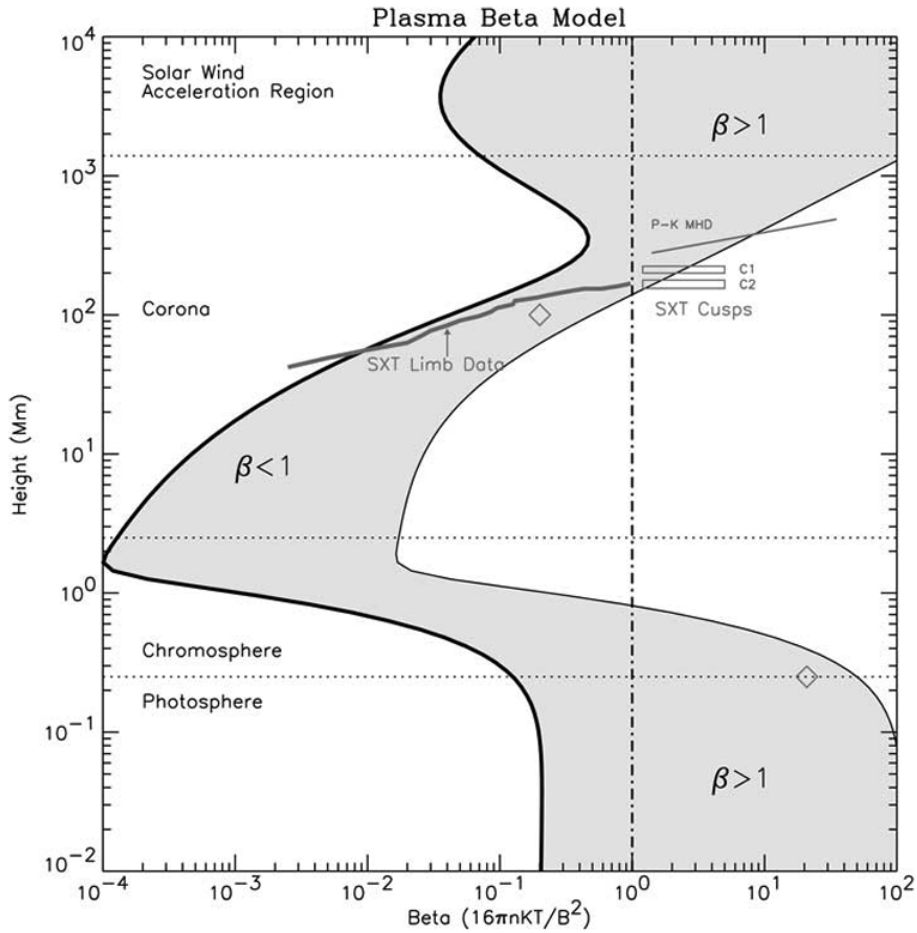
Figure 1.2: Typical plasma β values over an active region. (from Gary, 2001)

values in other physical quantities (such as temperature and density) due to differences in the strength and morphology of the magnetic field (Maltby et al., 1986). Therefore, it is essential to differentiate between these regions to perform a quantitative discussion of solar phenomena.

- Coronal/Chromospheric heating -

As introduced earlier, some heating mechanisms must occur because the temperature increases as the height increases in the upper layer than the photosphere. The problem in which the physical mechanism causing this heating is unknown is called the chromospheric/coronal heating problem. The chromospheric/coronal heating problem has been one of the most important problems in solar physics for about 80 years since the corona was found to be a million degrees (Edlén, 1943).

I summarize the average energy fluxes required to heat the chromosphere/corona in Table 1.1. These values are less than 0.1 times the value of the turbulent energy flux
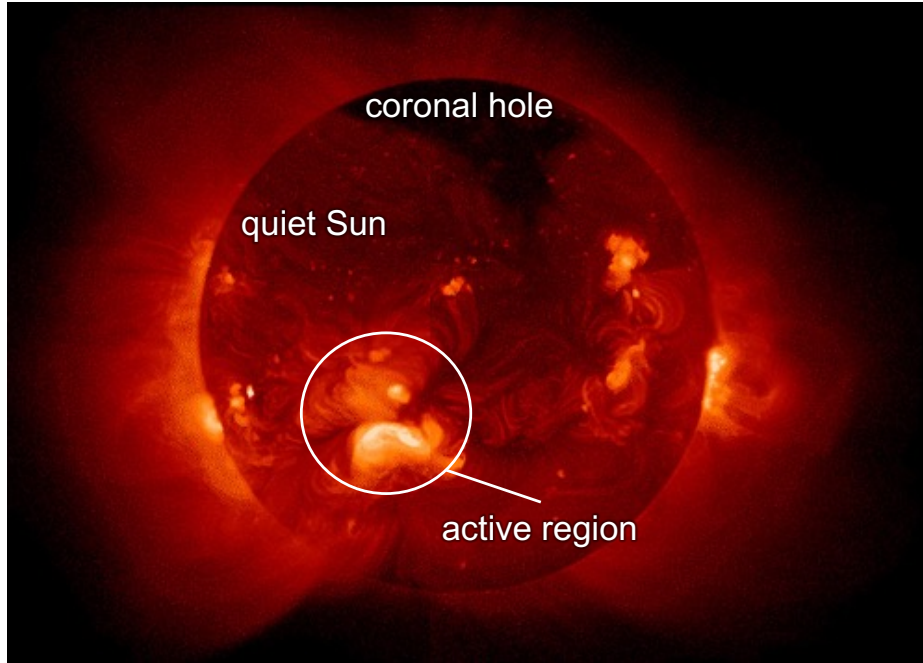
Figure 1.3: Solar corona observed by soft X-ray (from https://www.isas.jaxa.jp/j/forefront/2005/shimizu/).

Table 1.1: Chromospheric and coronal energy losses (from Withbroe & Noyes, 1977)

Parameter	Quiet Sun	Coronal hole	Active region
Coronal energy losses ($\mathrm{erg\,cm^{-2}\,s^{-1}}$)			
Conduction flux	2×10^5	6×10^4	10^5 to 10^7
Radiative flux	10^5	10^4	5×10^6
Solar wind flux	$\lesssim 5 \times 10^4$	7×10^5	$< 10^5$
Total corona loss	3×10^5	8×10^5	10^7
Chromospheric radiative losses ($\mathrm{erg\,cm^{-2}\,s^{-1}}$)			
Low chromosphere	2×10^6	2×10^6	$\gtrsim 10^7$
Middle chromosphere	2×10^6	2×10^6	10^7
Upper chromosphere	4×10^6	4×10^6	2×10^7
Total chromospheric loss	$10^4 - 10^5$	$100 - 10^3$	$10^3 - 10^4$

of convection at the base of the photosphere (about $10^8\,\mathrm{erg\,cm^{-2}\,s^{-1}}$, Schwarzschild, 1948). Therefore, if turbulent energy at the surface is somehow transported to the upper atmosphere, it is possible to heat the chromosphere/corona in terms of energy balance.

The magnetic field is the key to transporting turbulent energy on the solar surface to the upper layers. Poynting flux is generated by the turbulent motion of the magnetic field on the solar surface, which transports energy to the upper layers. The theory of chromospheric/coronal heating can be broadly classified into direct current (DC) or nanoflare
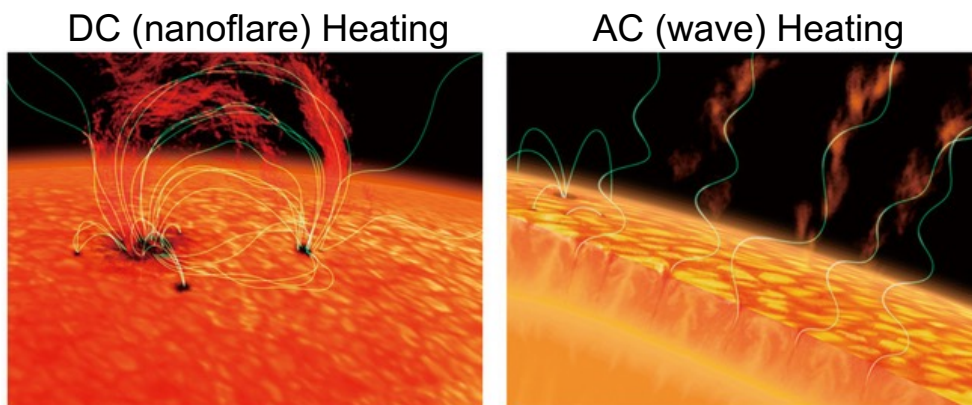
Figure 1.4: Schematic diagrams of AC/DC heating (from https://www.isas.jaxa.jp/en/feature/forefront/160229.html).

heating and alternating current (AC) or wave heating, depending on the speed of motion of magnetic field lines due to turbulence (Figure 1.4). In DC heating, the slow motion of the magnetic field lines accumulates torsion and is eventually dissipated by small magnetic reconnection (nanoflare) in the upper atmosphere. In AC heating, the magnetic field lines move fast enough to propagate energy as a wave to the upper layers, where it is eventually dissipated by some means. We have no consensus on whether DC or AC heating is the dominant mechanism. The latest realistic simulations report a dominance of DC heating (Rempel, 2017). In contrast, some studies have shown that AC heating becomes dominant when the resolution of numerical simulations is improved (Kuniyoshi et al., 2021), and further research is needed. In this thesis, I focus the discussion on DC heating in particular.

1.2 Solar flare and coronal mass ejection / filament eruption

1.2.1 Solar flare

Solar flares are explosions that occur in active regions of the Sun. Their energies are approximately $10^{29} - 10^{32}$ erg, the most energetic active phenomena in the solar system. Flares were first observed in the 1800s in white light (Carrington, 1859; Hodgson, 1859). As giant explosions in the Sun, flares are studied for their astronomical and plasma physics interest and their impact on human society.

Flares are believed to be caused by magnetic reconnection, whereby magnetic energy is converted into thermal and kinetic energy. One of the observational evidence for magnetic reconnection is that the distance between the two-ribbon structures seen in the Hα lines increases with time (Svestka, 1976; Zirin, 1988) (Figure 1.5a). Observations of soft and hard X-rays by the Yohkoh satellite (Ogawara et al., 1991) provided more robust evidence
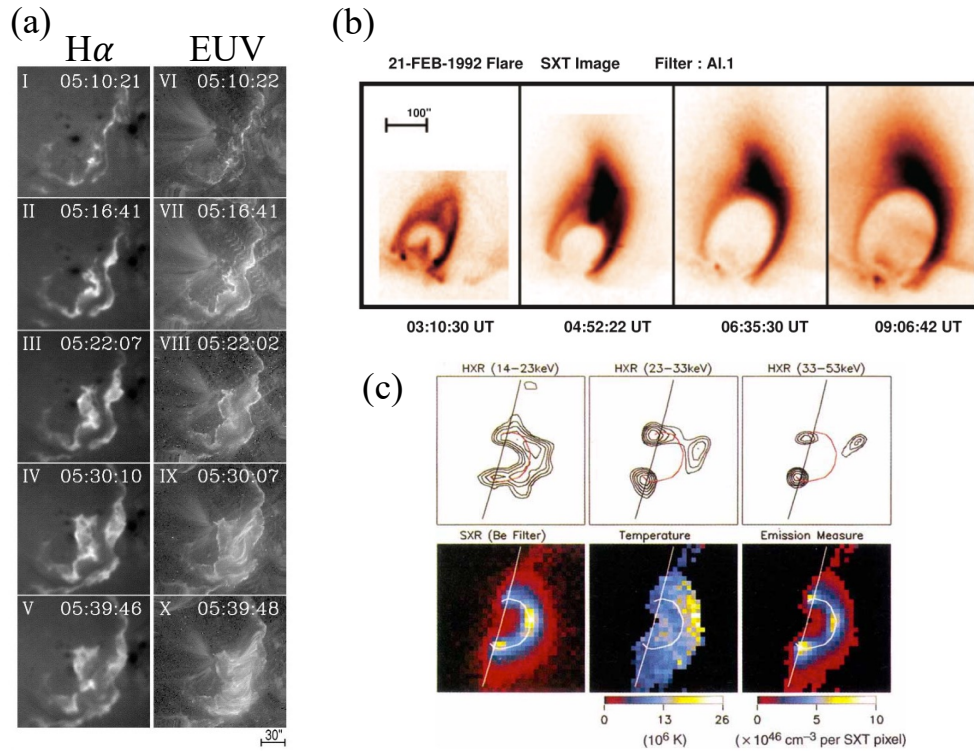
Figure 1.5: Observational evidence of magnetic reconnection for solar flare. (a) two-ribbon (from Asai et al., 2003). (b) cusp-shape (from Tsuneta et al., 1992a; Tsuneta, 1996; Shibata & Magara, 2011). (c) loop-top source (from Masuda et al., 1994).

for the reconnection. Tsuneta et al. (1992a) found cusp-shaped loop structures of flares (Figure 1.5b). Masuda et al. (1994) found that hard X-ray emission sources appear at the loop top of a flare (Figure 1.5c). These observations can be explained by the fact that magnetic reconnection occurs above the flare loops (Shibata & Magara, 2011).

During flares, brightenings are observed in various layers of the solar atmosphere, and each has its characteristic properties (Kane, 1974) (Figure 1.6). At wavelengths corresponding to hard X-rays, microwaves, and white light, the intensity increases sharply and then decays rapidly. In contrast, soft X-rays, Hα, and coronal EUV lines show a gradual increase in intensity followed by decay over a long time. The hard X-ray brightening phase is called the "impulsive phase." After the end of hard X-ray brightening, the phase in which soft X-rays gradually brighten/decay is called the "gradual phase." Also, the hard X-ray light curve roughly corresponds to the time derivative of the soft X-ray light curve, which is called the Neupert effect (Neupert, 1968). Spectra of two ribbons observed with chromospheric lines such as the Hα line usually show red-shifted emissions (Ichimoto & Kurokawa, 1984). This redshift is called "red asymmetry."

The above features of flare brightening are believed to be explained by chromospheric
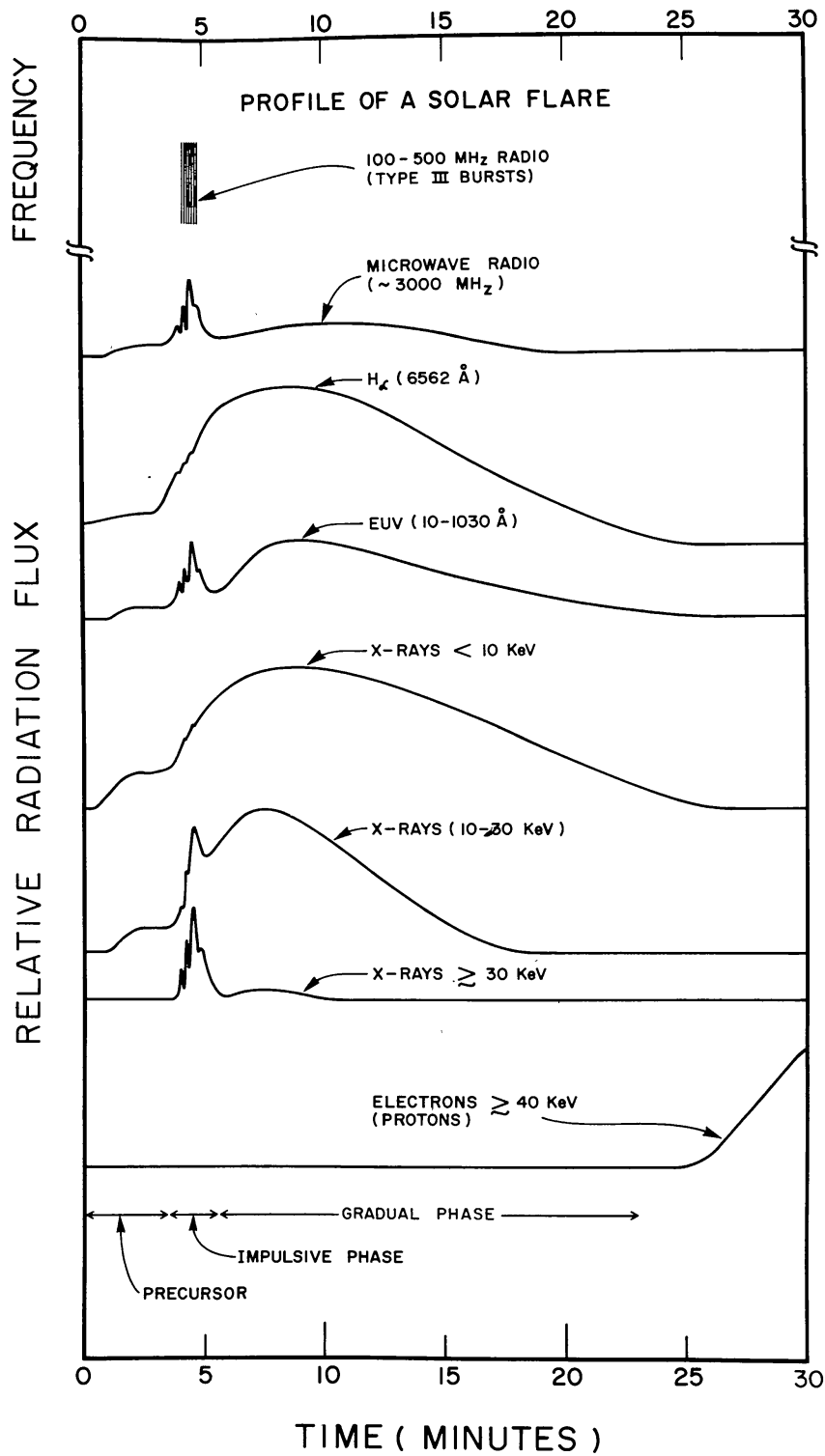
Figure 1.6: Light curves of solar flares at various wavelengths (from Kane, 1974).
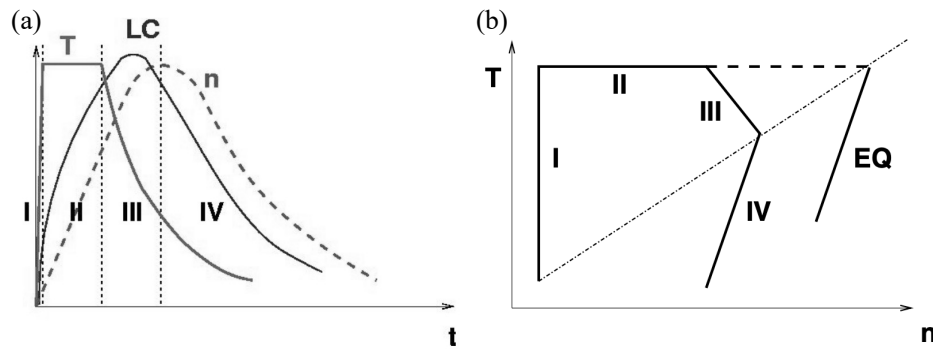
Figure 1.7: (a) Schematic diagram of the time evolution of temperature (T, thick solid line), soft X-ray light curve (LC, thin solid line), and density (n, dashed line) during a flare. (b) Schematic diagram of the flare evolution of Figure 1.7a in a temperature-density diagram. The dashed-dotted line shows a loop in the equilibrium. (from Reale, 2007)

evaporation/condensation. This model's essence is that the heat generated by coronal reconnection is transported to the chromosphere by some mechanism, resulting in sudden chromospheric heating. As a result of the rapid heating of the chromosphere, which increases the gas pressure, high-temperature and high-density plasma is driven into the corona. The rise of the heated chromospheric plasma is called "chromospheric evaporation." The process of heating the chromosphere increases the intensity of hard X-rays, and evaporated plasma increases the intensity of soft X-rays. In the soft X-ray enhancement model by chromospheric evaporation, a time difference in the peak time of the coronal temperature and density necessarily appears (Figure 1.7). While the sudden heating in the chromosphere produces evaporation, it also produces a downward propagating supersonic flow with a shock. The dense chromospheric plasma behind the downward propagating shock is called "chromospheric condensation" (Fisher et al., 1985). The chromospheric condensation plasma is denser than evaporation plasmas, and radiation cooling works very well, keeping its temperature around 10^4 K. Hence, red asymmetry can be observed in the chromospheric lines. I discuss in Chapter 2 whether this evaporation/condensation picture holds for smaller flares in the quiet Sun of the corona.

1.2.2 Coronal mass ejections / Filament eruption

- Coronal mass ejection-

Various magnetized plasma eruptions have been observed in the Sun. Coronal mass ejections (CMEs) are a prime example: the ejection of plasma from the solar corona into interplanetary space (Figure 1.7). CMEs were first discovered in the 1970s by coronagraphic observations from space (Tousey, 1973). They are still observed mainly by coronagraphs from space and are actively studied, including their effects on the Earth.
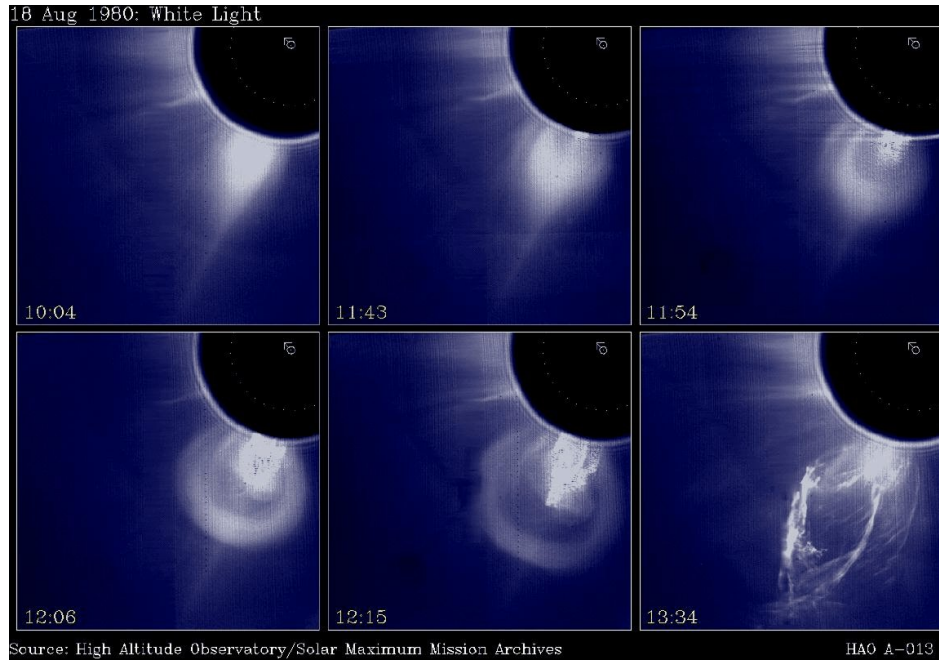
Figure 1.8: A coronal mass ejection that occurred in August 1980. (from https://www.windows2universe.org/sun/images/aug1980cme.jpg)
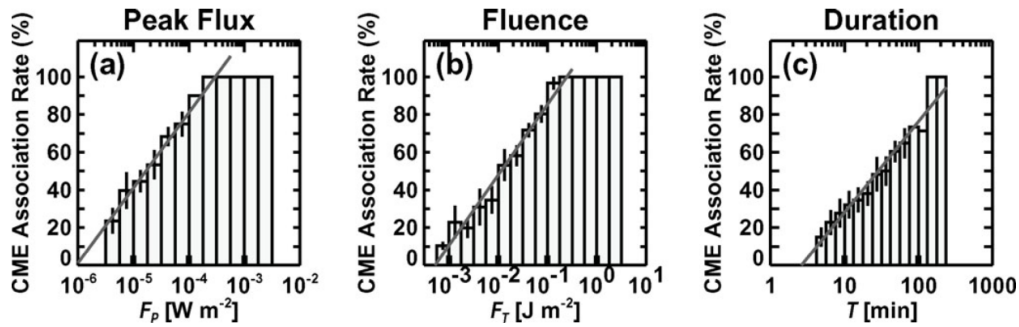
Figure 1.9: Solar flares association rate with CMEs (from Yashiro & Gopalswamy, 2009)

The nature of CMEs has been well investigated by many statistical studies (e.g., Yashiro & Gopalswamy, 2009). CMEs have velocities and masses of about $100-2000 \, \mathrm{km \, s^{-1}}$ and $10^{13} - 10^{17} \, \mathrm{g}$, respectively. The kinetic energy of CMEs is about $10^{28} - 10^{32} \, \mathrm{erg}$, which is comparable to the energy of a solar flare. It is also known that flares often accompany CMEs, and the stronger the energy, the more frequently CMEs are accompanied by flares (Figure 1.9).

Correlations between the physical quantity of CMEs and the energy of flares associated with CMEs have been studied to investigate the relationship between CMEs and flares. The power-law index between the CMEs mass M_{CME} and the flare X-ray flux/fluence

is reported to be approximately $0.59 - 0.70$ (Aarnio et al., 2011; Drake et al., 2013). As for the kinetic energy, it is roughly proportional to the flare energy. Takahashi et al. (2016) derived theoretical scaling laws between the physical quantity of CMEs and the flare energy E_{flare}. They showed $M_{\text{CME}} \propto E_{\text{flare}}^{2/3}$ for the CMEs masses M_{CME}. This power-law index of $2/3$ is close to the observational values mentioned earlier. They also showed $v_{\text{CME}} \propto E_{\text{flare}}^{1/6}$ for CMEs velocities v_{CME}. This relation agrees with the upper limit of the observed value.

- Filament eruption -

Filaments/prominences are plasmas at chromospheric temperatures floating in the solar corona. Those in the solar disk as seen from the earth are called "filaments," while those out of the solar disk are called "prominences." Filaments are located above magnetic neutral lines, and the magnetic forces support the cool plasma against gravity. Filaments in active regions and those in the quiet Sun have different properties and are called active region filaments and quiescent filaments, respectively. Active region filaments are short in length, have a short lifetime, and erupt in about one day. On the other hand, quiescent filaments are long and long-lived, with the longest existing for about a month. See the review by Labrosse et al. (2010) for more details on the physical quantities of filaments.

Filaments are known to erupt often. It is believed that filament eruptions with velocities above a certain level do not fall due to gravity and eventually become the CMEs core. In other words, the filament eruption corresponds to the beginning of the time evolution of CMEs. Because accelerations by magnetic forces cause filament eruptions, their magnetic field structure has been vigorously investigated by observation and numerical modeling (see the review of Mackay et al., 2010). However, there is currently no consensus on the magnetic field structure and instability mechanism that causes the eruption.

The details of the evolutionary process from filament eruption to CMEs are an open question. This is because filaments are observed at lower heights ($< 1.5 R_{\text{Sun}}$) by chromospheric lines, whereas CMEs are observed at $> 4 R_{\text{Sun}}$ by coronagraphs. The filament advances upward under acceleration. This acceleration is confirmed by the fact that the speed of the CMEs cores is faster than the speed of the corresponding filaments (Figure 1.10). However, no data existed to discuss how filaments evolve. Regarding this problem, the Solar Orbiter (Müller et al., 2020) recently performed extremely wide-field observations, which captured the filament's acceleration process as it erupted from the solar surface to ($> 6 R_{\text{Sun}}$) (Mierla et al., 2022). More examples of such ultra-wide-field-of-view observations are expected to improve our understanding of how filament eruptions evolve into CMEs in the future.

- Plasmoid ejection -

In some cases, plasma blobs at coronal temperatures, rather than filaments at chromo-
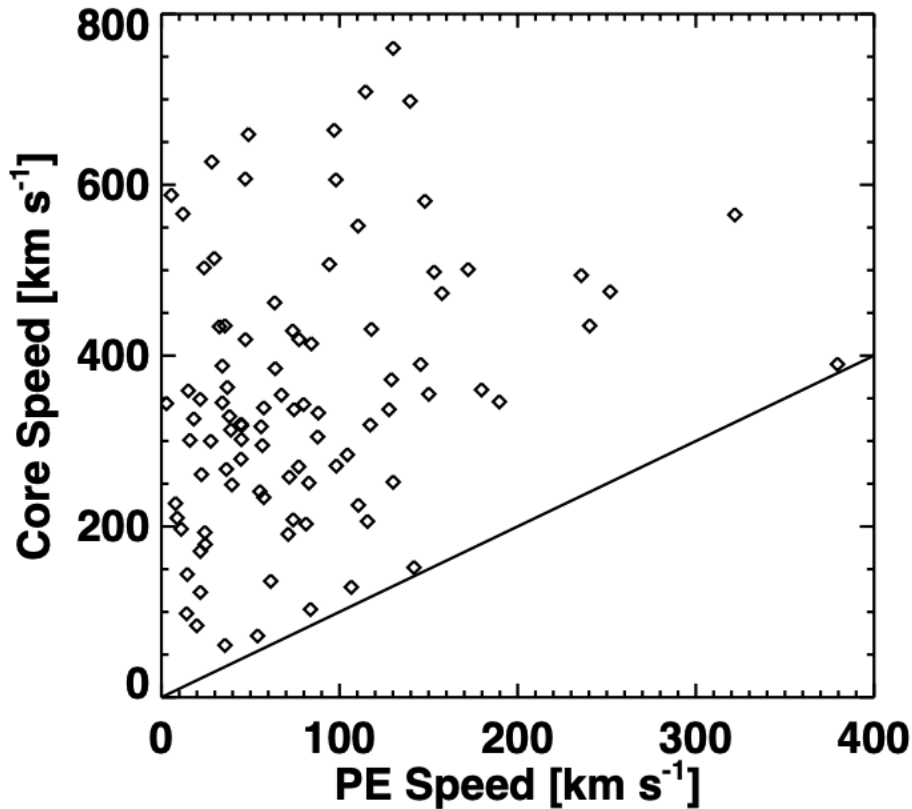
Figure 1.10: Comparison of CMEs and filament (prominence) velocities (from Gopalswamy et al., 2003).

spheric temperatures, are observed to erupt in association with flares (Figure 1.11a). The plasma blob at coronal temperature is called a "plasmoid." Plasmoids were discovered in soft X-ray images taken by the Yohkoh satellite (Shibata et al., 1995; Ohyama & Shibata, 1998). Ohyama & Shibata (1998) estimated the plasmoid temperature to be $10.6\pm3.6\,\mathrm{MK}$ and the electron density to be $(8-16)\times10^9\,\mathrm{cm}^{-3}$. They also report their mass as $(2-4)\times10^{13}\,\mathrm{g}$. Plasmoids erupt in the impulsive phase and are considered to have an essential relationship with flare triggers.

Theoretically, plasmoids are considered magnetic islands formed by tearing instability in the current sheet of magnetic reconnection. Therefore, plasmoids have attracted attention as the key to achieving fast reconnection. Takasao et al. (2012) found the first observational evidence of tearing instability occurring fractally in the flare current sheet. In the future, more detailed physical quantities of plasmoids obtained by Solar-C/EUVST will help us better understand why fast magnetic reconnection occurs in solar flares.
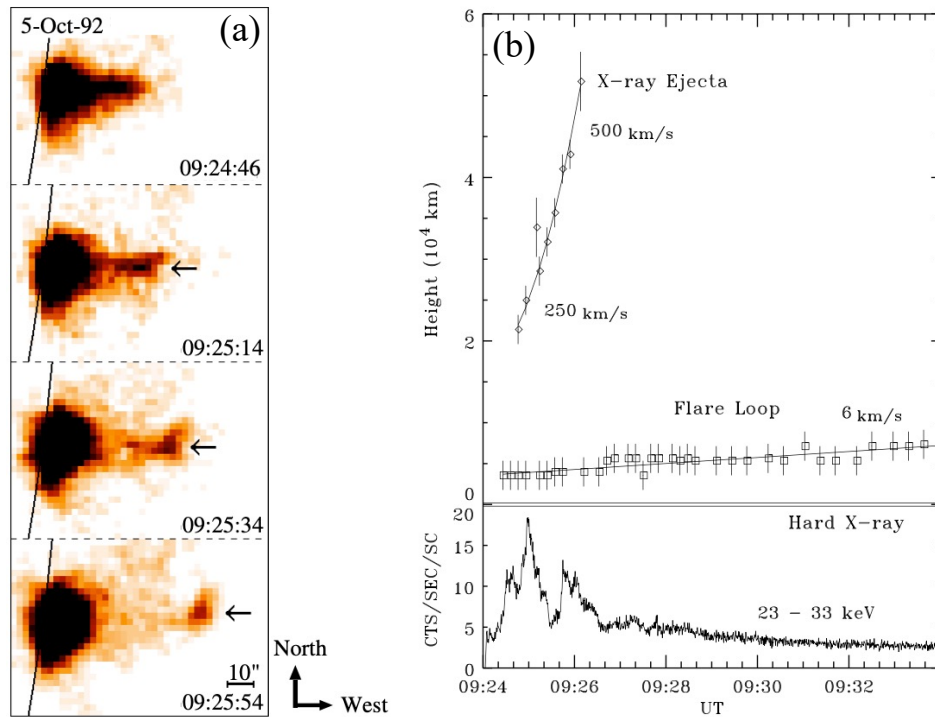
Figure 1.11: An overview of plasmoid ejection (from Ohyama & Shibata, 1998). (a) Soft X-ray images of a plasmoid ejection. (b) Time evolution of the plasmoid height compared to the hard X-ray light curve and the flare loop height.

1.2.3 Standard flare model

The standard flare model has been proposed to explain the properties of flares and associated ejecta (CMEs/filaments/plasmoids) as introduced earlier (Shibata et al., 1995). This model is also called the "CSHKP model" (Carmichael, 1964; Sturrock, 1966; Hirayama, 1974; Kopp & Pneuman, 1976). In this model, a mass ejection is a key to achieving fast magnetic reconnection. Mass ejection decreases the plasma near the current sheet, resulting in a strong reconnection inflow into the current sheet. With a strong inflow, fast reconnection is achieved, resulting in a flare. This scenario is consistent with the fact that plasmoid ejections coincide with the impulsive phase (Figure 1.11b).

The standard flare model is suggested to apply to flare/mass ejection phenomena in other scales (Shibata, 1999). I will cover this topic in more detail later (Sections 1.3.1 and 1.3.2).
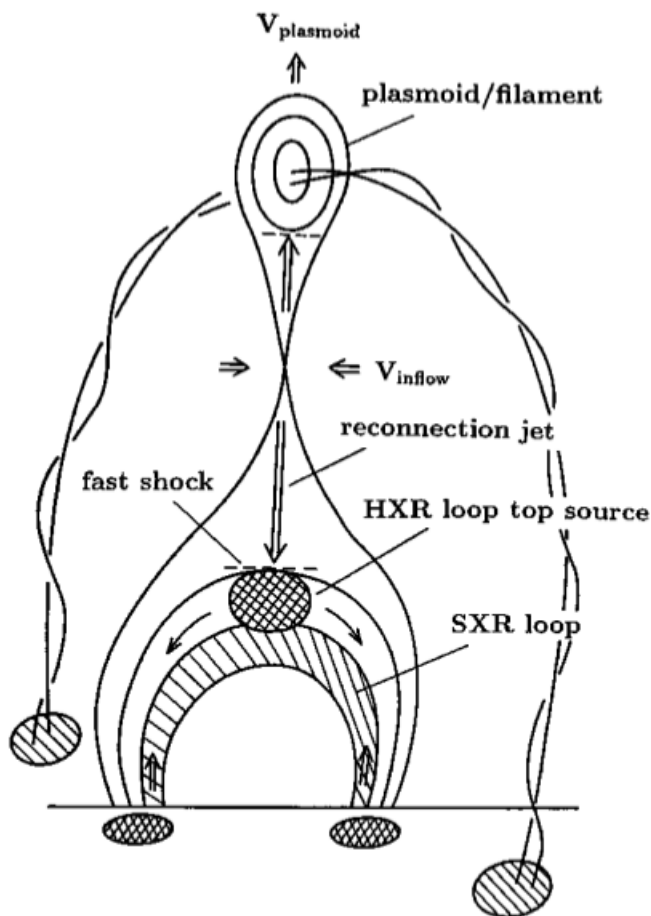
Figure 1.12: Schematic diagram of the standard flare model (from Shibata et al., 1995).

1.2.4 Giant arcade

Large arcades with cusp-like structures are often observed in the quiet Sun of the solar corona (Tsuneta et al., 1992b; McAllister et al., 1992, 1996; Hanaoka et al., 1994) (Figure 1.13). They are called "giant arcades." Filament eruptions and CMEs often accompany giant arcades. The typical loop length is $> 10^{10}$ cm, the temperature is $4\,\mathrm{MK}$, and the electron density is $10^8\,\mathrm{cm^{-3}}$ (Yamamoto et al., 2002).

Although a giant arcade has a different soft X-ray intensity, its physical mechanism is believed to be magnetic reconnection, similar to solar flares. Tsuneta et al. (1992b) found that cusp-shaped loops appear in giant arcades. They also found that the giant arcade was accompanied by filament eruptions and that the height of the arcade loop increased with time. These properties are common to solar flares. In addition, Yamamoto et al. (2002) showed that its temperature and emission measure (EM) are roughly consistent with the scaling law of solar flares (Shibata & Yokoyama, 1999, 2002). These results support that
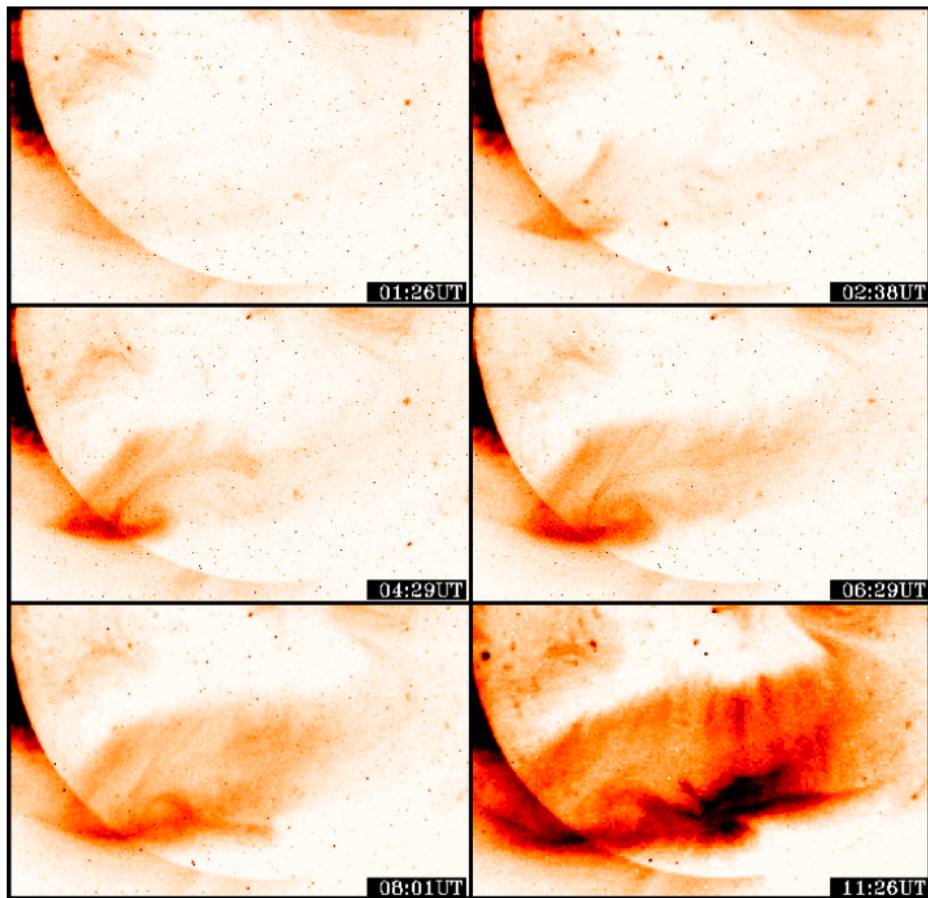
Figure 1.13: A giant arcade observed in the soft X-ray in April 1994 (from McAllister et al., 1996; Shibata & Magara, 2011).

magnetic reconnection occurs even in the quiet Sun.

1.3 Flares and Mass Ejections in Various Scale

In the Sun, brightening and mass ejections have been found even on a smaller scale than the flare/mass ejections described in Section 1.2. These small phenomena have been found in the corona and the chromosphere/photosphere. In addition, flares with greater energy than solar flares have been found in stars. This section presents a comprehensive overview of active phenomena that occur on scales other than those typical solar flares/mass ejections.

1.3.1 Solar microflare and coronal jet

- Micro/nano flare in the active region-

Small flares frequently occur in active regions of the solar corona. Assuming 10^{32} erg as the largest flare energy in the Sun, small flares with energies of about $10^{26} - 10^{29}$ erg are called "microflares," and those with energies of about $10^{23} - 10^{26}$ erg are called "nanoflares."

Microflares were discovered in the 1980s with soft X-rays (Schadee et al., 1983) and hard X-rays (Lin et al., 1984). In the 1990s, the Yohkoh / soft X-ray telescope (SXT: Tsuneta et al., 1991) discovered numerous microflares, and the statistical properties of microflares became clear. Shimizu (1995) reported the following physical quantities of microflares in active regions based on the results of statistical analysis: temperatures, $4 - 8 \times 10^6$ K; volume EM, $10^{44.5} - 10^{47.5}$ cm^{-3}; electron densities, $2 \times 10^9 - 2 \times 10^9$ cm^{-3}; gas pressure, $5 - 20$ dyn cm^{-2}; loop length, $5 \times 10^3 - 4 \times 10^4$ km; loop width, $2 \times 10^3 - 7 \times 10^3$ km; duration, $2 - 7$ min; and flare energy, $10^{25} - 10^{29}$ erg. They also found that the relationship between flare frequency and energy is roughly the same as for solar flares.

In the 2000s, the *Reuven Ramaty High Energy Solar Spectroscopic Imager* (RHESSI: Lin et al., 2002) observations revealed a comprehensive picture of the hard X-ray emissions of microflares (Hannah et al., 2011). Neupert effect was also found to appear in microflares. By taking spectra over a wide range of energies, the thermal and power-law components of the microflares were obtained simultaneously (Hannah et al., 2008). Hannah et al. (2008) also reported that the temperature of the thermal component was typically around 13 MK. The spatially resolved microflare structure by RHESSI indicates higher energy hard X-ray emission at the loop footpoint (Krucker et al., 2002; Liu et al., 2004; Hannah et al., 2008). These results show that non-thermal electrons are injected into the chromosphere in microflares, similar to solar flares.

Small flares have been actively studied for their contribution to coronal heating. The energy of the currently discovered small flares is insufficient to heat the corona. Thus, a power-law index α between flare frequency dN/dE and energy E has been investigated in many studies to understand the contribution of smaller energy flares to coronal heating. From the following simple calculation, flares with small energies could have a dominant contribution to coronal heating if the power-law index α is less than -2 (Hudson, 1991):

$$P = \int_{E_{\min}}^{E_{\max}} \frac{dN}{dE} E \, dE = \frac{A}{\alpha + 2}(E_{\max}^{\alpha+2} - E_{\min}^{\alpha+2}), \qquad (1.1)$$

where P is the total energy released by all flares and A is a constant. For microflares in active regions, the power-law index is reported to be larger than -2 ($-1.5 \sim -1.6$, Shimizu, 1995). However, smaller energy flares have also been found on the Sun, and it is important to investigate their power-law index.

With recent instrument performance improvements, smaller nanoflares are detected in active regions. The FOXSI-2 (Glesener et al., 2016; Christe et al., 2016) observed
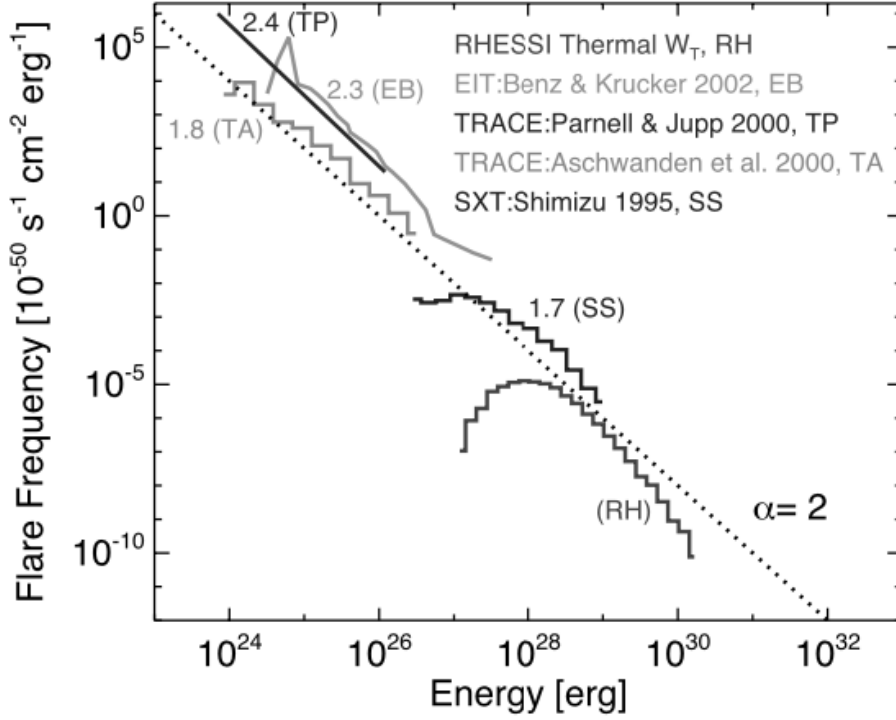
Figure 1.14: Flare frequency vs flare energy (from Hannah et al., 2008). Note that the definition of the sign of α is different from that in equation (1.1).

more than 10 MK of plasma, despite no brightening in soft X-rays in a quiescent active region (Ishikawa et al., 2017). Small brightening in braiding forms has also been found in loops (Cirtain et al., 2013), and small jets expected to accompany them have been found (Antolin et al., 2021). Future studies are expected to investigate the effects of these events on coronal heating.

- Micro/nano flare in the quiet Sun-

Small flares have also been found in the quiet Sun of the corona. They are observed mainly in the EUV. Aschwanden et al. (2000) reported their typical physical quantities as follows: temperatures, $< 2 \times 10^6$ K; EM, $10^{25} - 5 \times 10^{26}$ cm^{-5}; electron densities, $2 \times 10^8 - 10^9$ cm^{-3}; gas pressure, $0.1 - 0.4$ dyn cm^{-2}; spatial scale, $2 \times 10^3 - 10^4$ km; and thermal energy, $5 \times 10^{23} - 5 \times 10^{26}$ erg. These values indicate that small flares in the quiet Sun have smaller temperatures and densities than microflares in active regions (Shimizu, 1995).

Small flares in the quiet Sun typically have less energy than those in active regions and have been actively studied for their contribution to coronal heating. The energy of the currently discovered small flares of the quiet Sun is not enough to heat the corona (Chitta et al., 2021a). The power-law index of the frequency and energy of small flares in the quiet
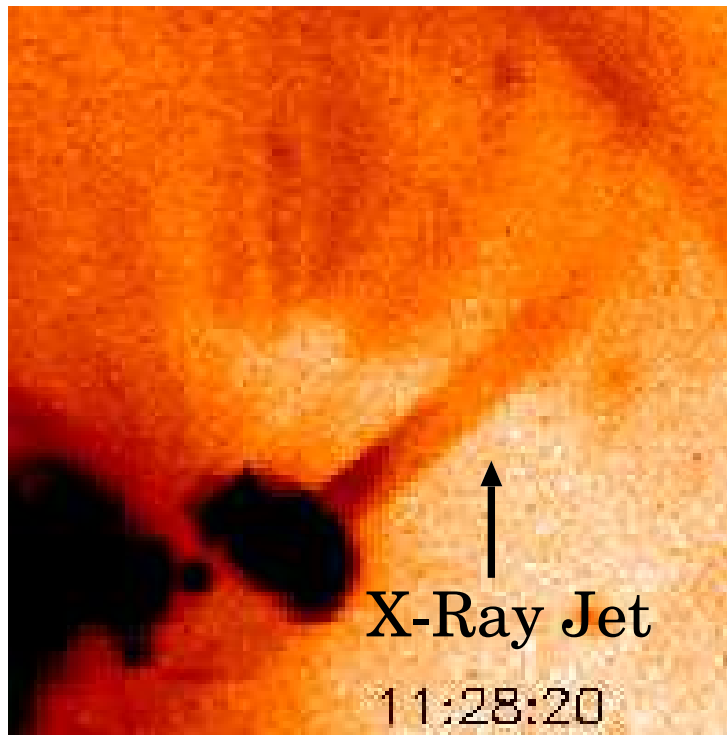
Figure 1.15: A typical example of coronal jets (from Shibata et al., 1992).

Sun has been investigated in many studies; however, its value varies from study to study (e.g., Aschwanden et al., 2000; Parnell & Jupp, 2000; Benz & Krucker, 2002; Joulin et al., 2016; Chitta et al., 2021a; Purkhart & Veronig, 2022) (Figure 1.14). Since several studies have used the same telescopes, the indefiniteness of this power-law index may not be due to a lack of resolution but to some problem with the analysis method.

Small flares in the quiet Sun are known to have many other characteristic properties, such as occasional accompanying eruptions of cool plasma and occurring at network boundaries. In addition, smaller flares than conventional ones have been discovered in recent Solar Orbiter/Extreme Ultraviolet Imager (Rochus et al., 2020) observations. I introduce these topics in more detail in Section 2.1.

- Coronal jet-

A collimated flow (jet) is often associated with micro/nano flares in the solar corona (Figure 1.15). Coronal jets were first discovered in the 1980s (Brueckner & Bartoe, 1983). Many coronal jets were discovered in Yohkoh/SXT in the 1990s, and their statistical properties became clear (Shibata et al., 1992; Shimojo et al., 1996). Shibata et al. (1992) and Shimojo et al. (1996) summarize the basic parameters of coronal jets as follows: jet length, $5 \times 10^3 - 4 \times 10^5$ km; jet width, $5 \times 10^3 - 10^5$ km; lifetime, $100 - 3 \times 10^4$ sec; translational velocity, $30 - 300 \, \mathrm{km \, s^{-1}}$; and kinetic energy, $10^{25} - 10^{28}$ erg. Shimojo & Shibata
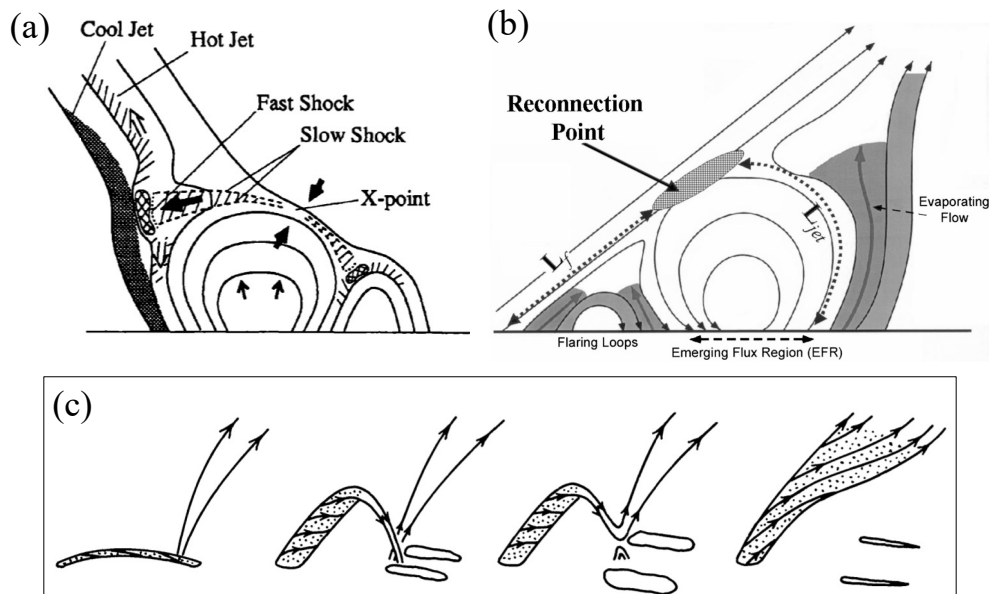
Figure 1.16: Schematic diagrams of coronal jet's acceleration mechanisms. (a): Acceleration by enhanced gas pressure due to a fast shock (hot jet) and by whip-like motion (cool jet) (from Yokoyama & Shibata, 1996). (b): Chromospheric evaporation (from Shimojo & Shibata, 2000). (c): Acceleration by magnetic pressure due to non-linear Alfvén waves (from Shibata & Uchida, 1986). Note that Shibata & Uchida (1986) originally used this idea to explain filament eruption, but the idea is applicable to coronal jets.

(2000) later reported the thermodynamic quantities of coronal jets as follows: temperatures, $3 - 8 \times 10^6$ K; electron densities, $7 \times 10^8 - 4 \times 10^9$ cm^{-3}; and thermal energy, $10^{27} - 10^{29}$ erg. The values of these thermodynamic quantities are roughly similar to those of footpoint microflares of a jet.

Coronal jets are known to have other characteristic properties. Shibata et al. (1992) found that coronal jets are often accompanied by jets of chromospheric temperature. Shimojo et al. (1996) found that many jets show constant or converging shapes. Shimojo et al. (1998) studied the polarity of the magnetic field at the footpoint of coronal jets and reported that 72 % were in mixed polarities. These two studies imply that the jets erupt from the region near the magnetic neutral point. Some coronal jets have also been reported to be accompanied by type III radio bursts (Aurass et al., 1994; Kundu et al., 1995). All these features support the idea that coronal jets result from magnetic reconnection.

Numerical simulations played a significant role in understanding the acceleration mechanism of coronal jets (Figure 1.16). Yokoyama & Shibata (1996) performed 2D magneto-hydrodynamics (MHD) simulations and investigated acceleration mechanisms for hot and cool components of coronal jets (Figure 1.16a). In their calculations, the hot jet was accelerated by the gas pressure enhanced by the terminal fast shock created by the reconnection
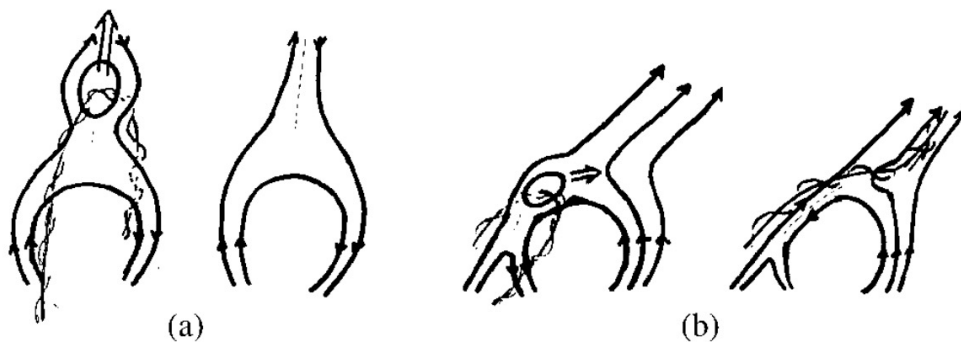
Figure 1.17: Schematic diagrams of the unified model of solar flares and coronal jets (from Shibata, 1999). (a) solar flares. (b) coronal jets.

outflow. In contrast, the cool jet was accelerated by magnetic-centrifugal force. Shimojo et al. (2001) performed 1D numerical simulations and showed that chromospheric evaporation flows form coronal jets (Figure 1.16b). Miyagoshi & Yokoyama (2004) performed 2D MHD simulations considering thermal conduction and showed that two types of jets are formed simultaneously: a low-density jet caused by enhanced gas pressure due to a fast shock and an evaporation jet. While the above numerical simulation contributed significantly to our understanding of the acceleration mechanism of coronal jets, it was not a 3D simulation and thus could not verify whether acceleration due to the release of magnetic twist occurs in coronal jets (Shibata & Uchida, 1985, 1986) (Figure 1.16c). 3D simulations of coronal jets have recently addressed this problem, and these studies have confirmed acceleration by magnetic pressure due to non-linear Alfvén waves (Pariat et al., 2009; Wyper et al., 2018). Determining which acceleration mechanism works in real coronal jets is one of the remaining challenges for observational studies (Sako et al., 2014).

Motivated by much evidence that coronal jets are formed by magnetic reconnection, Shibata (1999) proposed a unified model of jets and solar flares (Figure 1.17). In the unified model, magnetic reconnection is triggered by plasmoid/filament ejection, as in the standard flare model, even in the case of coronal jets. In the case of a jet, unlike solar flares, the plasmoid/filament eruption immediately collides with the ambient magnetic field. This collision causes a new reconnection, and the twisting motion released from the reconnection propagates along the ambient magnetic field. This collision occurs on a timescale of about Alfvén time $(10 - 100\,\mathrm{s})$. Thus, no plasmoid/filament ejections were observed in coronal jets in the Yohkoh/SXT era. However, small-scale filaments (called minifilaments) and plasmoids have begun to be observed in recent *Atmospheric Imaging Assembly* onboard the *Solar Dynamics Observatory* (SDO/AIA) (Pesnell et al., 2012; Lemen et al., 2012) high temporal resolution observations (Sterling et al., 2015; Kumar et al., 2019). These observations support the unified model of coronal jets and solar flares.
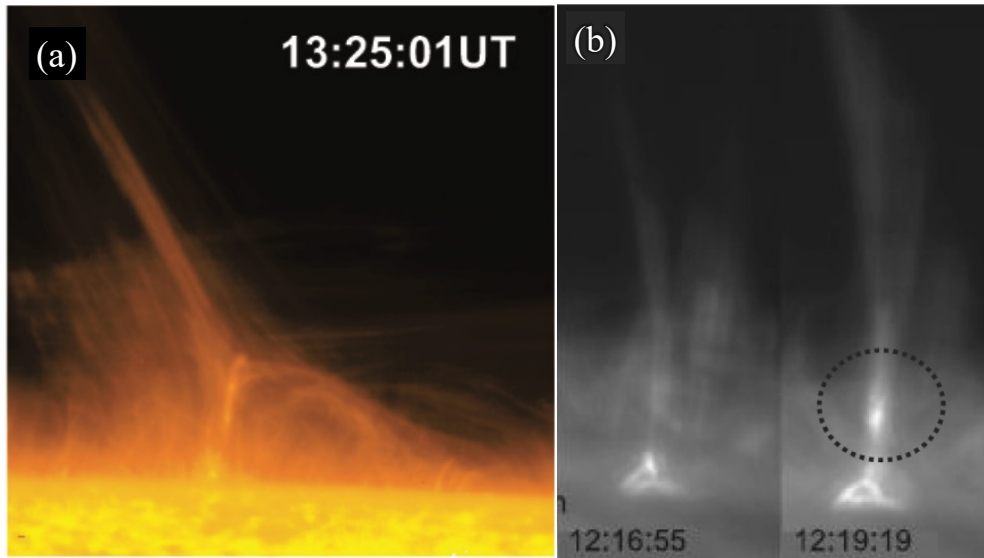
Figure 1.18: (a) A typical example of chromospheric anemone jets (from Nishizuka et al., 2008). (b) A plasmoid ejection in the chromospheric anemone jet (from Singh et al., 2011).

1.3.2 Chromospheric/Photospheric flare/jet

- Chromospheric anemone jet-

In the chromosphere, magnetic reconnection has been confirmed as brightening accompanied by jets (Shibata et al., 2007; Nishizuka et al., 2008) (Figure 1.18a). High-resolution observations with the Solar Optical Telescope (SOT: Tsuneta et al., 2008) onboard Hinode (Kosugi et al., 2007) first discovered these jets. These jets in the chromosphere have a brightening at the footpoint, and the characteristic inverted-Y shape is very similar to coronal jets. Thus, they are called "chromospheric anemone jets," corresponding to the anemone jets in the corona (Shibata et al., 1994). Nishizuka et al. (2011) performed a statistical study of chromospheric anemone jets and summarized their physical quantities as follows: jet length, $1 \times 10^3 - 4 \times 10^3 \, \text{km}$; jet width, $100 - 400 \, \text{km}$; duration, $100 - 500 \, \text{s}$; and translational velocity, $5 - 20 \, \text{km s}^{-1}$. Note that the velocity of the chromospheric anemone jet is comparable to the Alfvén velocity in the middle chromosphere. As further evidence of magnetic reconnection, plasmoid ejections have been found with chromospheric anemone jets (Shibata et al., 2007; Singh et al., 2011) (Figure 1.18b).

The acceleration mechanism of chromospheric anemone jets was investigated by numerical simulation. Takasao et al. (2013) performed 2D MHD simulations to investigate the acceleration mechanism of chromospheric anemone jets. They found that the formation mechanism of chromospheric jets depends on whether magnetic reconnection occurs in the photosphere or near the transition region. When reconnection occurs in the photosphere, a slow mode wave generated by the reconnection propagates to the upper
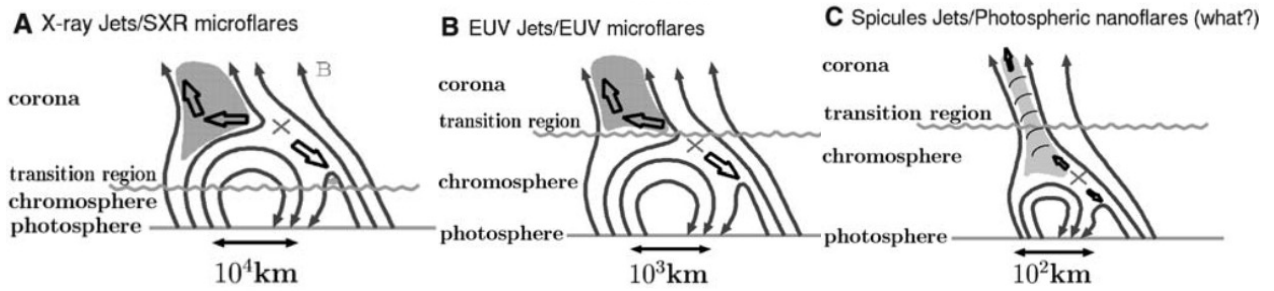
Figure 1.19: Schematic diagrams of magnetic reconnections that occur at various heights (from Shibata et al., 2007).

atmosphere and grows into a slow shock. This slow shock lifts the transition region and generates a chromospheric jet. In contrast, when magnetic reconnection occurs near the transition region, the Lorentz force accelerates the chromospheric plasma. This plasma is further accelerated by the interaction of the slow shock formed by reconnection with the transition region. These acceleration mechanisms are common to coronal jets in that magnetic reconnection is the origin of the jet. However, these acceleration mechanisms differ from those of coronal jets in that the interaction between the transition region and the slow shock is important.

The discovery of chromospheric anemone jets suggests that magnetic reconnection takes place at any height in the solar atmosphere. In other words, it suggests that magnetic reconnection occurs and jets are universally generated in similar magnetic field morphology, although the spatial scales are different (Shibata, 1997; Shibata et al., 2007). This idea could extend the unified model of flares and jets to smaller spatial scales. However, jets' acceleration mechanism is expected to differ depending on the height at which magnetic reconnection occurs. When reconnection occurs in the corona (Figure 1.19A), chromospheric evaporation flow is expected to mix with the jet. In contrast, when reconnection occurs in the lower atmosphere, such as in the photosphere, the plasma is expected to rise only about a scale height (Shibata et al., 2007). Instead, the MHD waves generated by reconnection are expected to propagate into the upper layers and grow into shocks, forming another jet (Figure 1.19C). Note that little numerical simulation exists for the dynamics of magnetic reconnection in the photosphere, and no observational examples exist. Therefore, the dynamics resulting from reconnection in the lower atmosphere is an open question for the future, and I will discuss this topic in Section 4.

- Spicule -

Spicules are universally generated jets throughout the chromosphere and are observed near the solar limb (Figure 1.20). Spicules were first observed by Secchi (1875). Beckers (1972) summarized their typical properties as follows: temperatures, $9000 - 17000\,\mathrm{K}$; densities, $10^{10} - 10^{11}\,\mathrm{cm}^{-3}$; maximum height, $4 \times 10^3 - 10^4\,\mathrm{km}$; and velocity, $20 -$
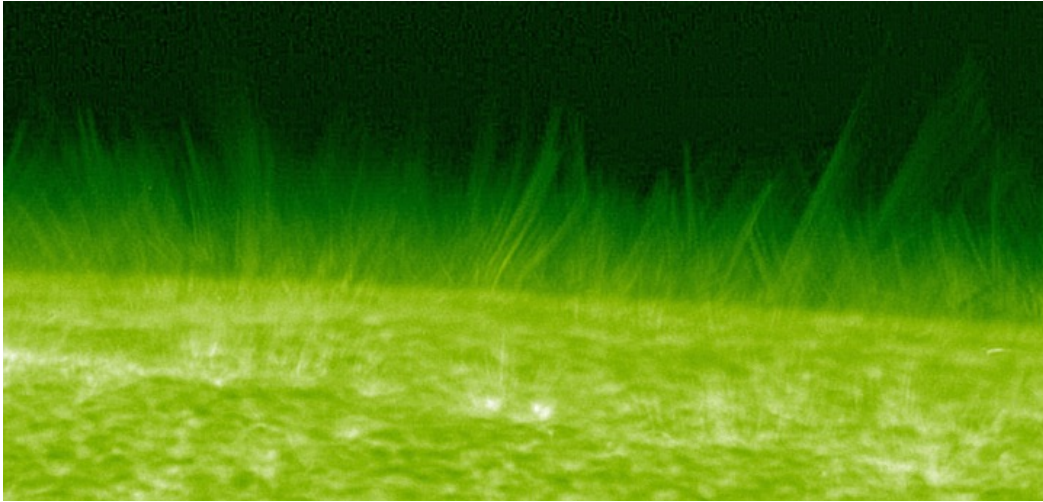
Figure 1.20: A typical example of spicules (from `https://hinode.nao.ac.jp/gallery/`, ©NAOJ/JAXA).

$100\,\mathrm{km\,s^{-1}}$. Note that these physical quantities vary slightly depending on the region of the Sun (active regions, quiet Sun, and coronal hole) where the spicule is observed (Zhang et al., 2012; Pereira et al., 2012; Iijima & Yokoyama, 2015).

The most popular theory for the formation mechanism of spicules is that sound waves generated by convective motion propagate into the upper layers and grow into shocks, lifting the transition region (Suematsu et al., 1982; Suematsu, 1990; De Pontieu et al., 2004). However, the Hinode/SOT observations began to find spicules larger than those explained by the above theory (De Pontieu et al., 2007b). Various theories have been proposed for the formation mechanism of these large spicules and are highly controversial, but magnetic energy conversion through magnetic reconnection is one leading hypothesis. This reconnection hypothesis corresponds to Figure 1.19C. Samanta et al. (2019) found that spicule activity increased when opposite-polarity magnetic fields appeared. This result indirectly supports the magnetic reconnection theory. The formation process of spicules is expected to be verified by higher-resolution observations and numerical simulations.

- Ellerman bomb -

Ellerman bombs are short-lived brightenings in the wings of chromospheric lines observed in the active region. In particular, they refer to brightenings in the Hα line wing. Ellerman bombs were first discovered in the 1910s (Ellerman, 1917). As the instrument capability has improved, smaller Ellerman bombs have been discovered, and their properties have been studied (e.g., Georgoulis et al., 2002; Nelson et al., 2013). Nelson et al. (2013) performed a statistical analysis of Ellerman bombs and reported their properties as follows: spatial scale, $10^2 - 10^3\,\mathrm{km}$; duration, $0.45 - 30\,\mathrm{min}$; and energy,

$2 \times 10^{22} - 2 \times 10^{25}$ erg. Ellerman bombs are considered heating phenomena that occur in the photosphere or lower chromosphere because of the appearance of brightening at the wing (Kitai, 1983).

The most plausible mechanism for the Ellerman bombs is the magnetic reconnection in the photosphere / lower chromosphere. Pariat et al. (2004) performed magnetic field extrapolation and examined the magnetic field morphology of 47 Ellerman bombs. They found that Ellerman bombs are located in structures with elongated flux tubes that undulate aperiodically. Based on its magnetic field characteristics, they proposed that the Ellerman bomb results from magnetic reconnection between different undulation peaks. Numerical simulations confirm that magnetic reconnection occurs in magnetic field morphologies similar to this hypothesis (Isobe et al., 2007; Danilovic, 2017). Watanabe et al. (2011) performed high-resolution observations of Ellerman bombs using the *Swedish 1-m Solar Telescope/Crisp Imaging Spectropolarimeter* (SST/CRISP) (Scharmer et al., 2003, 2008). They found that Ellerman bombs have extended like jets, some of which have an inverted Y shape. The result suggests similarities between Ellerman bombs and coronal/chromospheric anemone jets (Shibata et al., 1994, 2007).

Recent high-resolution ground-based observations have found the same type of spectral variations as Ellerman bombs, even in the quiet Sun (Rouppe van der Voort et al., 2016). They are called "quiet Sun Ellerman bombs" (QSEBs). Joshi et al. (2020) performed Hβ line observations and found that more than 500,000 QSEBs occur in the Sun every second. These studies suggest that magnetic reconnection occurs more universally in the solar lower atmosphere than previously believed.

1.3.3 Stellar flares and stellar filament eruption

- Stellar flare -

Flares have been observed in stars other than the Sun. They are called "stellar flares." Stellar flares were first discovered in the 1920s with observations by white light (Hertzsprung, 1924). In the 1990s, their properties began to be investigated by radio and X-ray observations (e.g., Koyama et al., 1996; Tsuboi et al., 1998). Stellar flares examined at these wavelengths usually show more significant variability than solar flares.

The statistical properties of stellar flares in late-type G-type stars like the Sun were revealed by the *Kepler* space telescope (Koch et al., 2010). Maehara et al. (2012) found 365 stellar flares in 148 G-type main-sequence stars (Figure 1.21). These stellar flares were found with quasi-periodic modulations. In addition, the maximum energy of stellar flares does not correlate with the stellar rotation period, but the faster rotation period stars have more frequent flares. These observations suggest that stars have giant spots (called
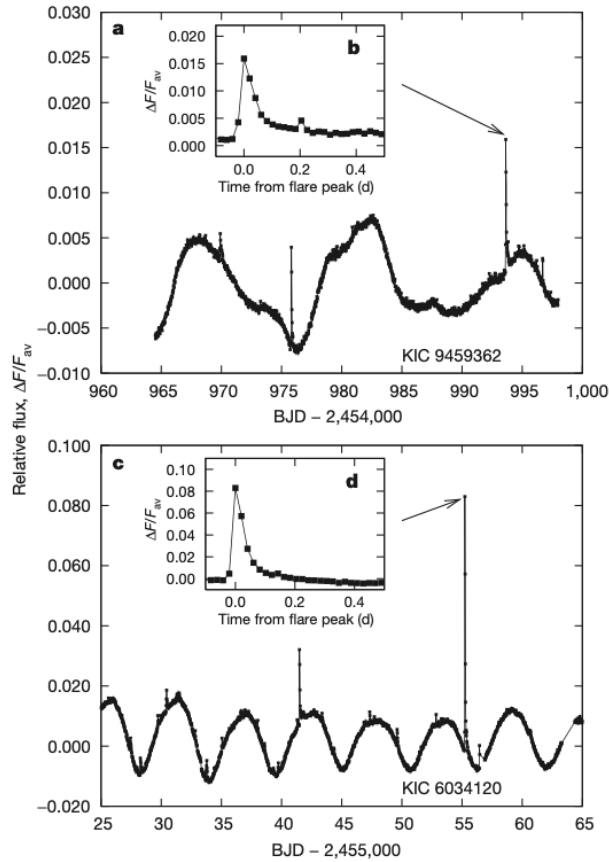
Figure 1.21: A typical example of stellar flares and quasi-periodic brightness modulations due to star spots (from Maehara et al., 2012).

"star spots," see reviews of Berdyugina, 2005; Strassmeier, 2009) and that stellar flares result from magnetic reconnection in star spots by a physical mechanism similar to that of solar flares. This picture is being established through further statistical analysis and studies of the time evolution of star spots (Shibayama et al., 2013; Maehara et al., 2015; Notsu et al., 2019; Namekata et al., 2019, 2020; Okamoto et al., 2021).

- Scaling laws applicable in solar and stellar flares -

One powerful tool in exploring the physical mechanisms of stellar flares is to compare them with scaling laws established for solar flares. Because stellar flares, unlike solar flares, cannot be spatially resolved, logical inferences from the physical laws are a valuable research tool. I briefly summarize a comparison of stellar and solar flares using the scaling laws below.

Motivated by Feldman et al. (1995), which compared X-ray observations of solar and stellar flares, Shibata & Yokoyama (1999) derived the following scaling law between emis-
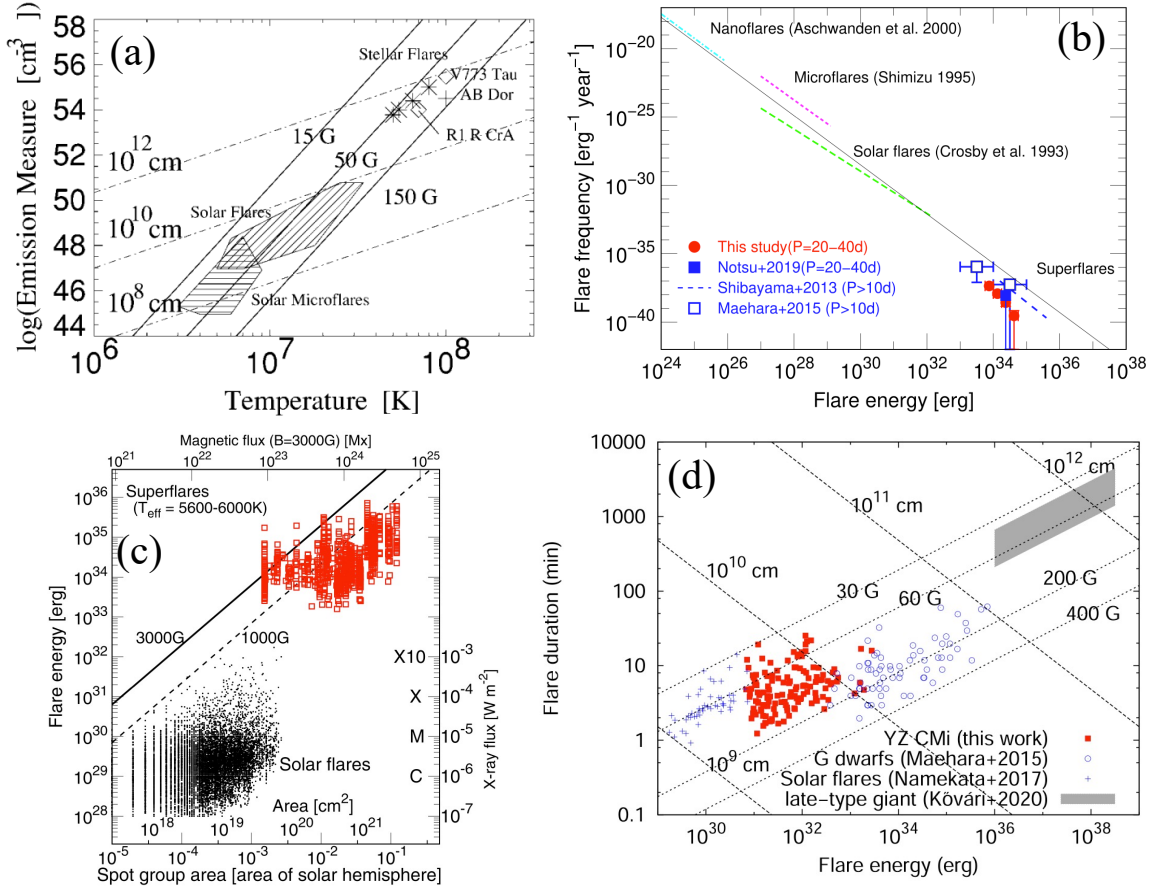
Figure 1.22: Various examples of scaling laws for solar/stellar flares. (a) Scaling law for temperatures vs emission measures (from Shibata & Yokoyama, 1999). (b) Flare frequency vs flare energy (from Okamoto et al., 2021). (c) Spot group area vs flare energy (from Okamoto et al., 2021). (d) Flare duration vs flare energy (from Maehara et al., 2021).

sion measure and temperature:

$$EM_v \simeq 10^{48} \left(\frac{B_{\mathrm{corona}}}{50\,\mathrm{G}} \right)^{-5} \left(\frac{n_0}{10^9\,\mathrm{cm}^{-3}} \right)^{3/2} \left(\frac{T_{\mathrm{peak}}}{10^7\,\mathrm{K}} \right)^{17/2}, \qquad (1.2)$$

where EM_v is the volume EM, B_{corona} is the coronal magnetic field strength, n_0 is the preflare electron number density, and T_{peak} is the temperature in the flare peak time. See Section 2.4.2 for more details on the assumptions of this scaling law. Figure 1.22a compares equation (1.2) and the solar/stellar flares. From Figure 1.22a, we can see that the solar/stellar flares are consistent with the scaling law for a coronal magnetic field strength of about 50 G. This result suggests that a common physical mechanism can explain solar/stellar flares. This study can be called a pioneering attempt to understand solar/stellar flares in a unified way.

Further evidence for a unified understanding of solar and stellar flares had to wait until

the discovery of many stellar flares by the *Kepler*. Maehara et al. (2012) and Shibayama et al. (2013) found that the flare frequency in Sun-like stars is roughly an extension of the frequency of solar flares. Shibata et al. (2013) compared flare energies and spot area and found that stellar flares are located at the extension of the upper limit of solar flare energies. These data were later analyzed again based on the Gaia Data Release 2 catalog (Berger et al., 2018), and those studies reached similar conclusions (Notsu et al., 2019; Okamoto et al., 2021) (Figure 1.22b and c).

Maehara et al. (2015) found the relationship $\tau \propto E^{0.39}$ by comparing flare energy E and duration τ. This power-law index is similar to solar flares (Veronig et al., 2002). Maehara et al. (2015) also theoretically derived the relationship $\tau \propto E^{1/3}$, assuming that the flare duration is roughly equal to the reconnection time. Namekata et al. (2017b) statistically analyzed the white-light flares in the Sun to make a more direct comparison with the physical quantities of stellar flares observed by the *Kepler*. As a result, they found a relationship $\tau \propto E^{0.38}$. This power-law index is almost the same as reported by Maehara et al. (2015). In addition, Namekata et al. (2017b) developed the scaling law obtained by Maehara et al. (2015) by including magnetic field strength B and spatial scale L as follows:

$$\tau \propto E^{1/3} B^{-5/3}, \tag{1.3}$$

$$\tau \propto E^{-1/2} L^{5/2}. \tag{1.4}$$

Based on a comparison of these equations with observations, the magnetic field strength of stellar flares is estimated to be 2-4 times stronger than those of solar flares (Namekata et al., 2017b; Maehara et al., 2021) (Figure 1.22d).

The above scaling laws show that the physical quantities of stellar flares result in extensions of solar flares. These results suggest that solar/stellar flares result from a common physical mechanism of "magnetic reconnection." However, note that these scaling laws do not discuss the ejections associated with stellar flares. I discuss a scaling law of ejecta associated with stellar flares in detail in the next topic and Chapter 3.

- Stellar filament eruption -

Many attempts have been made worldwide to detect CMEs associated with stellar flares in recent years. The existence of stellar CMEs not only provides evidence for a common physical mechanism with solar flares/CMEs but can also be important in discussions of stellar evolution and the habitability of exoplanets. Hence, the detection of stellar CMEs is an important astronomical problem. However, it is challenging to directly observe eruptions associated with stellar flares that cannot be spatially resolved. For this reason, many studies have tried to capture indirect evidence of ejecta associated with stellar flares using various methods. Typical approaches are to capture X-ray and EUV dimming associated with ejecta (Veronig et al., 2021), a blue shift in X-rays (Argiroffi et al., 2019), and a blue

shift in the chromospheric lines (stellar filament eruption) (e.g., Maehara et al., 2021). In this section, I introduce an attempt to capture the blue shift in chromospheric lines, which can be compared to filament eruptions in the Sun.

Stellar flares in M-/K-dwarfs are often accompanied by blue-shifted emissions in the chromospheric lines (e.g., Houdebine et al., 1990; Vida et al., 2016, 2019; Honda et al., 2018; Maehara et al., 2021). They are called "blue asymmetry." The most likely interpretation of blue asymmetry is a stellar filament eruption associated with a stellar flare. The relationship between flare energy and mass for blue asymmetry is an extension of the solar CMEs relationship. On the other hand, the relationship between flare energy and kinetic energy is on the lower side of the extension of the solar CMEs relation (Maehara et al., 2021). Unlike solar filament eruptions, the reason for the blue shift always observed in emission in blue asymmetry is being discussed. Regarding this problem, Leitzinger et al. (2022) recently performed 1D non-LTE modeling and cloud model analysis. They showed that filaments could be observed as emissions in M-type stars even when they are on the stellar disk. Future studies using such radiation transfer simulations are expected to advance our understanding of blue asymmetry.

While blue asymmetry is often observed in M-/K- type stars, blue shifts in the chromospheric lines associated with stellar flares had not been observed for a long time in G-type stars. This was because it is challenging to detect stellar flares in G-type stars in the first place, and no spectroscopic observations of stellar flares in G-type stars had been performed. However, there was a breakthrough recently. Namekata et al. (2022b) performed spectroscopic observations of young G-type stars with the 3.8 m Seimi telescope at the Okayama Observatory of Kyoto University (Kurita et al., 2020) and found that blue-shifted absorption in the Hα line appears with stellar flares (Figures 1.23a and b). They compared the spectra with those of solar filament eruptions and confirmed that the blue-shifted absorption appearing in the G-type star was similar to that of the solar filament eruptions. They also estimated the mass and velocity of the blue shift to be 10^{18} g and $-510\,\mathrm{km\,s^{-1}}$. By comparing these physical quantities with solar CMEs and a few examples of solar filament eruptions, they found that the stellar ones are an approximate extension of the solar events (Figures 1.23c and d). These results suggest that stellar filament eruptions have been detected for the first time in G-type stars and that a similar physical mechanism works as solar filament eruptions. In the future, it is expected to increase the number of observed examples to investigate the statistical properties and to understand the physical causes of more complex spectral variations through sun-as-a-star studies (Namekata et al., 2022a; Otsu et al., 2022).
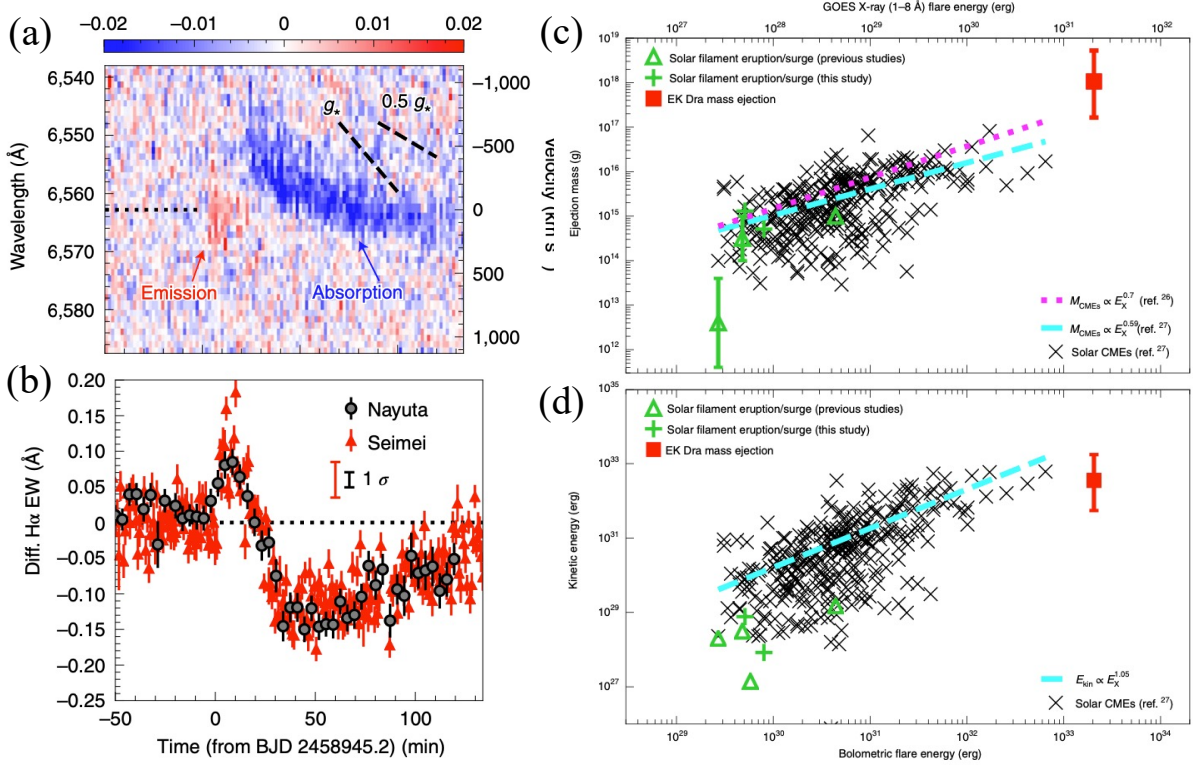
Figure 1.23: Observational evidence of stellar filament eruptions associated with stellar flares and their comparison with solar CMEs/filament eruptions (from Namekata et al., 2022b). (a) Time evolution of the Hα spectra. (b) Light curves of the Hα equivalent width. (c) and (d) Comparison of stellar filament eruptions and solar CMEs/filament eruptions with respect to mass and kinetic energy.

1.4 Aim of this thesis

The purpose of this thesis is to gain a better understanding of the physical mechanisms of small-scale flares and their associated dynamics on the Sun. As mentioned earlier, some evidence of magnetic reconnection has been found even in small flares on the Sun (Sections 1.3.1 and 1.3.2). Such small-scale magnetic reconnection may be the origin of the heating and dynamics of the solar atmosphere. Moreover, similar depictions could occur in other stellar atmospheres and astrophysical plasma. Therefore, understanding the physical mechanisms of small-scale magnetic reconnection is important in astrophysics. However, it is not fully understood how the thermal properties of the surrounding atmosphere change and what dynamics occur due to small magnetic reconnections in the solar atmosphere. In this thesis, I aim to deepen our understanding of those variations associated with small-scale reconnection through theoretical and observational studies.

A key concept throughout this thesis is the comparison of small flare observations and simulations with theoretical models and correlations for large solar flares. This concept

is based on the idea that certain aspects of MHD phenomena, as described by the scale universality of ideal MHD, are connected regardless of their scale. This approach has been used with great success in stellar flare studies, which are larger than typical solar flares (Section 1.3.3). Hence, this approach is expected to be effective even for smaller flares than typical solar flares. Through a comparison of correlations and theoretical models for large flares, I aim to understand the similarities and differences between small flares and large flares in the Sun in this thesis.

In Chapters 2 and 3, I focus on small flares accompanied by chromospheric temperature ejection in the quiet Sun of the solar corona. Although the qualitative properties of these small flares have been well investigated, it is not fully understood whether the theoretical models and correlations of large solar flares are really hold even for these small flares. Chapter 2 is based on Kotani et al. (2022, submitted) and describes the thermal properties of small flares in the quiet Sun of the solar corona. I mainly discuss the effect of magnetic reconnection in the corona on the chromosphere and the resulting time evolution of the thermodynamic quantities in the corona (cf. Figure 1.7). Chapter 3 is based on Kotani et al. (2022) and describes the correlation between the energy of small flares in the Sun and the physical quantities of the ejecta associated with the flare. By examining small flares in the Sun, this chapter aims to establish a correlation for ejecta at the chromospheric temperature associated with flares over a wide range of energies, from small solar flares to giant stellar flares.

Chapter 4 describes the results of numerical simulations of magnetic reconnection and the resulting jet-like structure in the solar photosphere, based on Kotani & Shibata (2020). The motivation for this chapter is a unified understanding of the dynamics caused by magnetic reconnection in the solar corona, chromosphere, and photosphere (Figure 1.19). To this end, I investigated the mechanism of jet formation resulting from magnetic reconnection in the photosphere, which had not been observed nor numerically simulated. In addition, I discuss the waves resulting from reconnection in the photosphere and their possible impact on the upper atmosphere.

Thermodynamic Properties of Small Flares in the Quiet Sun Observed by Hα and EUV: Plasma Motion of the Chromosphere and Time Evolution of Temperature / Emission Measure

2.1 Introduction

[†] Small flares are frequently observed throughout the solar atmosphere. In this chapter, we focus on small flares in the quiet Sun (QS) corona with energies of $10^{24} - 10^{27}\,\mathrm{erg}$ (hereafter "small flares").

Various instruments have observed brightenings associated with small flares for more than 20 years (Krucker et al., 1997; Krucker & Benz, 1998; Berghmans et al., 1998; Aschwanden et al., 2000; Parnell & Jupp, 2000; Benz & Krucker, 2002; Joulin et al., 2016; Chitta et al., 2021a; Purkhart & Veronig, 2022). Numerous studies have investigated whether small flares have the required energies to heat the solar corona (Parker, 1988). It is believed that the nanoflares observed with the current telescope resolution do not have enough energy to heat the steady corona (Chitta et al., 2021a). In contrast, we have not yet reached a consensus on whether nanoflares that are too small to be captured by the current resolution can be responsible for coronal heating. For nanoflares to have a significant con-

---

[†]This chapter is based on Kotani et al. (2022, submitted)

tribution to coronal heating, the power-law index between the flare frequency dN/dE and the flare energy E must be smaller than -2 ($dN/dE \propto E^{\alpha}$, $\alpha < -2$) (Hudson, 1991). In recent observations using the *Atmospheric Imaging Assembly* onboard the *Solar Dynamics Observatory* (SDO/AIA) (Pesnell et al., 2012; Lemen et al., 2012), Purkhart & Veronig (2022) reported a power-law index smaller than -2 ($\alpha = -2.28 \pm 0.03$), whilst Joulin et al. (2016) reported a power-law index larger than -2 ($\alpha = -1.73$ in the QS). Further understanding of the mechanism of small flares in the QS is crucially important for resolving this open question.

Small flares in the QS at coronal temperatures often accompany small eruptions at chromospheric temperatures (called "minifilament"). Minifilament eruptions were first reported in the 1970s (Moore et al., 1977; Labonte, 1979). Multi-wavelength observations using chromospheric and Extreme Ultraviolet (EUV) lines in the 2000s showed that they typically accompany coronal small flares (Sakajiri et al., 2004; Ren et al., 2008). These studies also reported that minifilament eruptions were associated with magnetic flux cancellation in the photosphere. Minifilament eruptions are often reported to be associated with jets (e.g., Sterling et al., 2015). Madjarska et al. (2020) reported simultaneous brightening in the Hα line and EUV accompanied by a minfilament eruption. Galsgaard et al. (2019) reproduced the coronal magnetic field at the location of a microflare and minifilament eruption in a coronal bright point (CBP, Madjarska, 2019) using the non-linear force-free field (NLFFF) method. They found that twisted magnetic field lines (flux ropes) form at the minifilament eruption location. This is similar to the magnetic morphology of solar flares (e.g., Jiang et al., 2013; Inoue et al., 2014; Yamasaki et al., 2022). Kontogiannis et al. (2020) and Panesar et al. (2022b) performed spectroscopic observations of chromospheric lines (Hα and Mg II, respectively) and reported that brightenings and downflow in the chromosphere are observed in response to EUV brightenings. Jin et al. (2021) observed microflares with minifilament eruptions using the AIA. They found that the AIA 304 Å light curve's peak precedes the coronal emission's peak by 2 or 3 minutes. This trend suggests a Neupert effect in large flares (Neupert, 1968); that is, the hard X-ray light curve corresponds to the time derivative of the soft X-ray light curve. All these properties support the interpretation that small flares in the QS with minifilament eruptions are miniature versions of typical solar flares associated with filament eruptions.

Recent observations by the Extreme Ultraviolet Imager (EUI, Rochus et al., 2020) onboard Solar Orbiter (SO, Müller et al., 2020) revealed small brightenings in the QS that were named "campfires" (Berghmans et al., 2021). The average temperature of these brightenings was estimated at $\log T = 6.1$, which is consistent with other brightenings observed in the QS in the past. Berghmans et al. (2021) and Zhukov et al. (2021) compared their length and height using triangulation with SO/EUI and SDO/AIA. These studies found that the height was larger than the length, which suggests that the brightenings

occur only near the apex of the loops. Panesar et al. (2021) found that campfires are often associated with magnetic flux cancellation and dark eruptions seen in EUV emission that may correspond to minifilament. With recent improvements in numerical simulation techniques, realistic simulations have been performed to reproduce the EUI brightenings (e.g., Tiwari et al., 2022; Panesar et al., 2022a). Chen et al. (2021) performed the 3D radiation magnetohydrodynamics simulation with a QS parameter and reproduced brightenings with similar properties to the observed features. They found that these brightenings are caused by heating the cool and dense plasma to 1 MK. This heating is due to magnetic reconnection that occurs below the transition region. This mechanism differs from the brightening mechanism involving chromospheric evaporation when reconnection occurs in the corona.

Although small flares in the QS have been studied intensively, the similarities and differences with the physical mechanisms of typical solar flares are not fully understood. In particular, we do not fully understand how small-scale reconnection events affect the chromosphere. Several minifilament eruption studies have reported brightening in the chromosphere with EUV brightening (e.g., Sakajiri et al., 2004; Madjarska et al., 2020). However, only Kontogiannis et al. (2020), Madjarska et al. (2022), and Panesar et al. (2022b) performed spectroscopic observations, and all studies analysed only one event. Investigating whether small flares in the QS also show red asymmetry in chromospheric lines observed during large flares (Ichimoto & Kurokawa, 1984; Canfield et al., 1990) may help us understand the heating mechanism at work (Ashfield & Longcope, 2021). To the best of our knowledge, there exist no studies clearly showing chromospheric evaporation at work during small flares in the QS. A comparison with scaling law studies of flares in active regions is also expected to help investigate the physical mechanism of small flares in the QS (e.g., Shibata & Yokoyama, 1999, 2002; Namekata et al., 2017b; Aschwanden, 2020). If the observations are consistent with the scaling law, we can expect the same physical mechanisms at work in small flares in the QS as in large flares.

In this study, we performed Hα line imaging and spectroscopic analysis together with coronal EUV imaging analysis of more than 20 small flares in the QS. We aimed to improve our understanding of the thermal evolution of small flares in the QS and their impact on the chromosphere. This chapter uses the term "small flare" while referring to brightening phenomena in EUV emission at coronal temperature.

2.2 Observations and data processing

We observed the chromosphere using the *Solar Dynamics Doppler Imager* (SDDI: Ichimoto et al., 2017) on the *Solar Magnetic Activity Research Telescope* (SMART: UeNo et al., 2004) at the Hida Observatory of Kyoto University. SDDI performs Hα imaging spectroscopy observations of the full solar disk with a time resolution of 12 s and a pixel size of

1.23 arcsec. In this study, we took Hα images at 25 wavelengths from H$\alpha - 3.0$ Å to H$\alpha + 3.0$ Å with a constant wavelength step of 0.25 Å. The data were processed with dark and flat field corrections. We used a position angle for the Sun to rotate the SDDI data and make the upward direction of the image orientate towards the solar north pole. We confirmed that the rotated SDDI data and AIA level 1.5 data generated by sunpy's aiapy.calibrate (Barnes et al., 2020) were aligned with an accuracy of less than $1.0\,\mathrm{arcsec}$.

We analysed small flares with plasma eruptions at chromospheric temperatures captured by SDDI and AIA from 21:56:17 UT on September 6, 2019, to 8:32:40 UT on September 7, 2019. All of these events occurred in the QS. We excluded near-limb events and analysed 25 small flares. These events are the same as our previous study investigating the relationship between chromospheric ejections and small flare energies in the QS (Kotani et al., 2022).

We used SDO/AIA data to study the properties of small flares. We checked images of the 304 Å and 6 coronal channels (94 Å, 131 Å, 171 Å, 193 Å, 211 Å, and 335 Å). The method used to determine the physical quantities (flare spatial scale, temperature, emission measure, and electron number density) of small flares was the same as in our previous study (Kotani et al., 2022) using differential emission measure (DEM) analysis (Hannah & Kontar, 2012). We defined the flare duration as the time between the brightening becoming visible and returning to its original intensity in the AIA 193 Å images. Thus, even if multiple brightening peaks are included, they are assumed to be the duration of a single event.

We used the *Helioseismic and Magnetic Imager* (HMI: Scherrer et al., 2012) onboard SDO to study the photospheric magnetic field of the small flares. We used magnetograms with a 45 seconds cadence because of the short duration of the events.

2.3 Results

2.3.1 Overview

In Fig. 2.1, we show a typical example of an event analysed in this study. We can see a brightening appearing in the AIA images from Fig. 2.1. The dark ejecta can be seen in the AIA 193 Å and 304 Å images (Fig. 2.1e, f, i, j, m, and n). The brightening in AIA 94 Å is weaker than in 193 Å (Fig. 2.1k and o). We can see from the HMI images that magnetic field polarities converge and cancel (Fig. 2.1d, h, l, and p). We also confirmed from the broader field of view images that this event occurred at the network boundary. All these properties are consistent with previous studies (e.g., Sakajiri et al., 2004; Panesar et al., 2021).
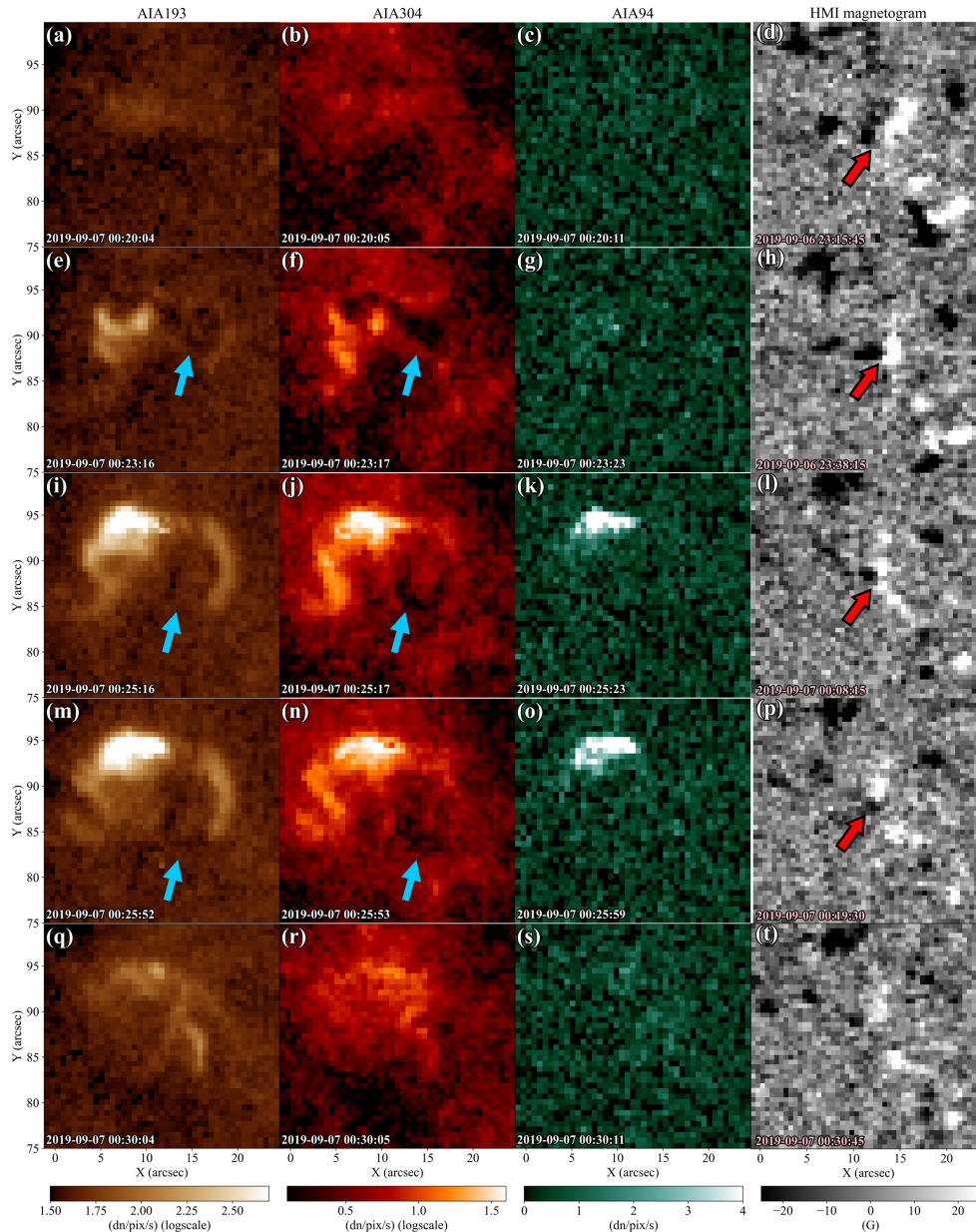
Figure 2.1: The time evolution of a typical event (event 4 in Table 2.1) in AIA and HMI images. The three left columns show the time evolution in AIA 193 Å, 304 Å, and 94 Å, respectively. Light blue arrows indicate dark ejecta. The right column shows the time variation of HMI magnetograms. Red arrows indicate dipole magnetic fields that indicate cancellation. HMI images are corrected for the effect of the solar rotation to track the field of view of the panel (t). Note that the AIA and HMI images on the same row are at different times.

Table 2.1: Parameters of small flares analysed in this study.

event	peak time (UT)	X (arcsec)	Y (arcsec)	L (km)[a]	t_{dur} (s)[b]	$\log(T_{\mathrm{DEM}}/[\mathrm{K}])$[c]	n (10^9 cm^{-3})[d]	v_{red} (km s^{-1})[e]	FC[f]	comments
1	0906T22:02:16	-350	230	1100	360	6.12	2.12		Y	MB[g]
2	0906T23:35:16	-260	-360	1500	360	6.14	2.54	2.82	Y	jet?
3	0907T00:09:16	-70	-450	2400	636	6.19	3.19	4.83	Y	CBP, jet
4	0907T00:25:52	10	90	3800	516	6.17	1.71	2.03	Y	
5	0907T01:32:16	320	470	1000	408	6.09	2.31	0.97	Y	jet, MB
6	0907T02:11:52	40	-450	2800	1008	6.17	2.94	4.48	Y	CBP
7	0907T02:18:16	620	-180	2200	540	6.12	1.74		Y	
8	0907T02:25:16	-420	480	3600	912	6.14	1.93		Y	MB
9	0907T02:32:28	-540	-40	1200	84	6.12	1.67	2.47	Y	
10	0907T03:17:04	610	510	2700	180	6.20	1.78		Y	CBP, jet, MB
11	0907T03:20:28	-100	-50	3200	900	6.13	1.79		Y	jet, MB
12	0907T03:47:28	-70	260	4300	1044	6.17	1.55		Y	CBP, jet, MB
13	0907T05:28:52	200	-290	2700	312	6.21	1.79	4.40	A	CBP
14	0907T05:38:52	-220	290	2200	360	6.15	1.91	1.50	Y	CBP?, jet, MB
15	0907T05:47:28	710	160	6200	1188	6.15	2.96	4.22	Y	CBP, jet, MB
16	0907T06:03:16	340	-480	1300	252	6.13	2.53	5.08	Y	CBP, jet?
17	0907T06:48:28	-320	-540	1600	360	6.11	2.11		Y	
18	0907T06:50:40	-420	430	1100	600	6.11	1.93		Y	MB
19	0907T06:49:28	-30	-510	2800	264	6.07	1.39	4.56	Y	jet, MB
20	0907T06:56:52	140	-790	2400	156	6.13	1.53		Y	CBP
21	0907T07:06:52	650	-100	3500	548	6.13	1.46		Y	jet
22	0907T07:13:52	-270	-660	1200	408	6.11	2.80	3.50	A	MB
23	0907T07:27:40	490	-30	1300	216	6.16	2.44	3.95	Y	MB
24	0907T07:35:16	190	350	4600	1368	6.20	1.97	4.35	Y	
25	0907T07:55:52	-660	320	1500	228	6.11	2.24		Y	jet

(a) flare spatial scale (square root of the area of brightening pixels)

(b) flare duration

(c) temperature in the flare peak time

(d) electron number density in the flare peak time

(e) maximum velocity for the redshift associated with Hα line centre brightening

(f) FC = flux cancellation. "Y" indicates that the cancellation has been confirmed. "A" indicates ambiguous events.

(g) MB = multiple brightening.

We show the physical quantities and their histograms for the events analysed in this study in Table 2.1 and Fig. 2.2. We can see from Fig. 2.2 that the events have spatial scales L (square root of the area of brightening pixels) between $1000\,\mathrm{km}$ and $6000\,\mathrm{km}$ and durations t_{dur} between $100\,\mathrm{s}$ and $1000\,\mathrm{s}$. The events have temperatures T_{DEM} between $10^{6.05}\,\mathrm{K}$ and $10^{6.2}\,\mathrm{K}$ and emission measure (EM) between $10^{26.5}\,\mathrm{cm}^{-5}$ and $10^{27.5}\,\mathrm{cm}^{-5}$. From these values, we can estimate the thermal energies between $10^{24}\,\mathrm{erg}$ and $10^{26.5}\,\mathrm{erg}$ and electron densities n between $1.5 \times 10^9\,\mathrm{cm}^{-3}$ and $3.0 \times 10^9\,\mathrm{cm}^{-3}$.

Based on these spatial scales and durations, we expect that the events analysed in this study correspond to the smaller events analysed in Aschwanden et al. (2000). Whilst the temperature is consistent with the results of Aschwanden et al. (2000), the density is a factor of three to ten times larger in our analysis. This difference in density is expected due to the different methods used to obtain the DEM. Aschwanden et al. (2000) estimated EM from the 195 Å filter of TRACE. By contrast, we used AIA 6 channels to estimate DEM distributions for a wider range of temperatures and the sum of these was used as
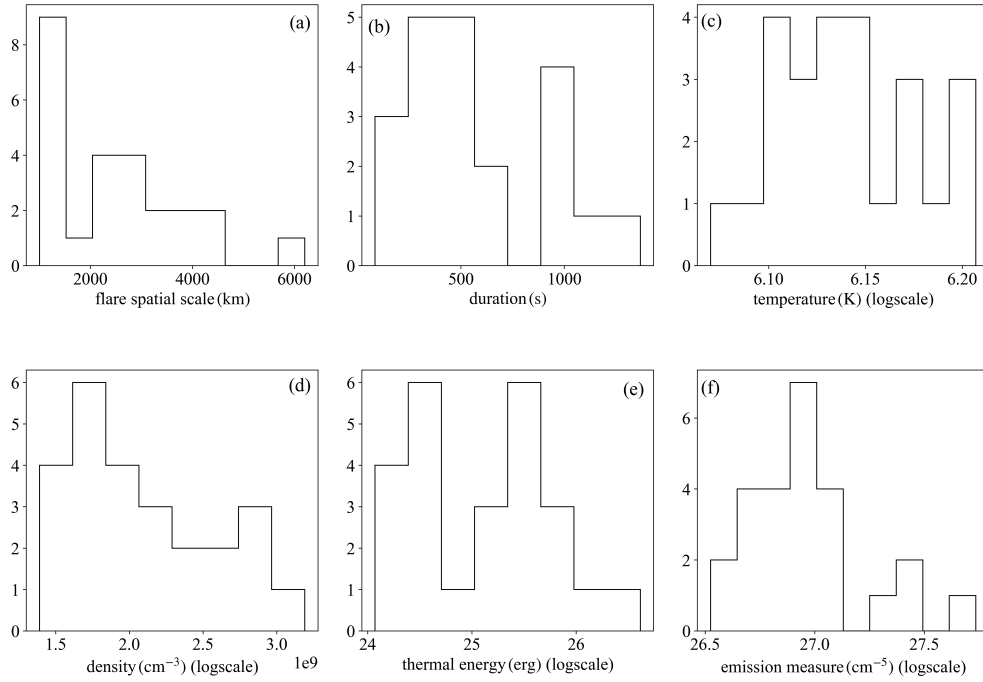
Figure 2.2: Histogram of the physical quantities of the events analyzed in this study. The panels (a), (c), and (f) are the same as in fig. 5 of Kotani et al. (2022).

EM. Thus, the EM values estimated in Aschwanden et al. (2000) are typically ten times smaller than those in our analysis. The thermal energy values appear to be consistent with Aschwanden et al. (2000); however, given the different density values, Aschwanden et al. (2000) may have underestimated the thermal energy by a factor of three to ten.

By comparing the recent SO/EUI campfire observations with the current analysis, we can see that our event corresponds to a large campfire (Berghmans et al., 2021). Spatial scale, lifetime, and EM have larger values in our analysis, whilst temperature values were almost the same. All of our events occurred at the network boundary, and we could clearly see flux cancellation in 92 % of the events. These features are consistent with campfires (Berghmans et al., 2021; Panesar et al., 2021).

Some of the events analysed in this study had some distinctive qualitative characteristics. Nine of the analysed events occurred at CBPs. It is known that small flares with eruptions of cold plasma also occur in CBPs (Madjarska, 2019). We should note that the events at CBP tended to have larger temperatures and electron densities but not as large as the microflares in the active region (Hannah et al., 2008). Coronal jets were also observed in several of our events. Considering that a jet with chromospheric temperature accompanying a coronal jet is formed by magnetic forces (Yokoyama & Shibata, 1996), it is a natural result that coronal jets were observed in some of our events, which had chromospheric plasma eruptions. Some recent campfire observations have also reported the
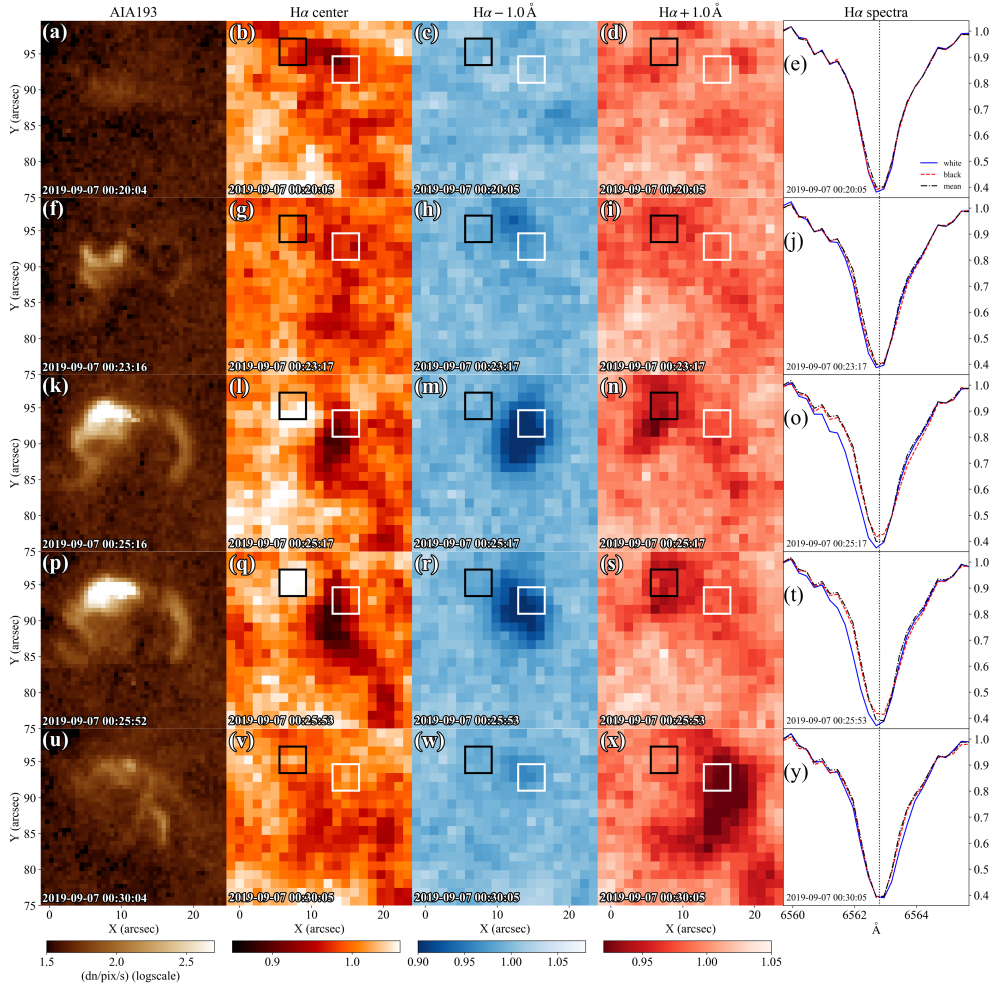
Figure 2.3: The time evolution of a typical event in the SDDI images and spectra. The event is the same as in Fig. 2.1. The left column shows the AIA 193 Å images shown for comparison. The middle columns show the time evolution in the Hα line at line centre, −1.0 Å, and +1.0 Å, respectively, from left to right. Each image is normalised by the average intensity of the surrounding area. Black squares indicate pixels of brightening at line centre with redshift. White squares indicate pixels of dark ejecta. The right column shows the time evolution of the Hα spectra. The solid blue and dashed red lines indicate spectra averaged by white and black squares, respectively. The dash-dotted black line indicates the average spectra of the surrounding area. Each spectrum is normalised to the Hα − 3.0 Å intensity of the average spectrum.

appearance of jets with coronal brightenings (Chitta et al., 2021b).

2.3.2 Hα spectrum

In Fig. 2.3 we show a typical example of a small flare recorded in the AIA and Hα line images. We can see a brightening in the corresponding pixels in the Hα line centre at
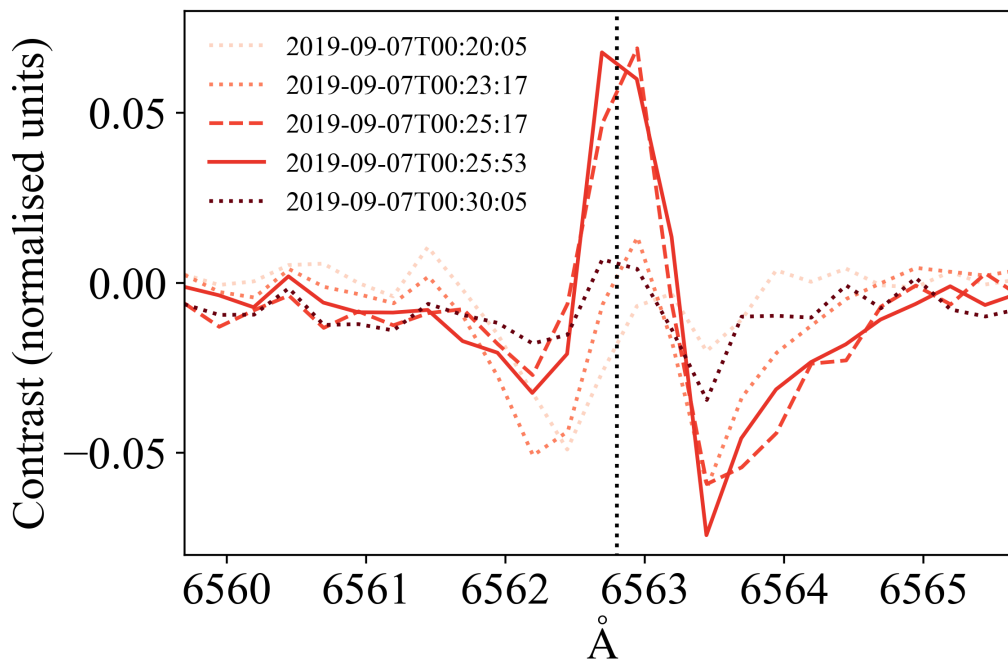
Figure 2.4: Time evolution of contrast for the redshift associated with the line centre brightening. Contrast is obtained as $(I_{\mathrm{red}} - I_0)/I_0$, where I_{red} is the redshifted spectrum shown as the red line in Fig. 2.3 and I_0 is the average spectrum shown as the black line. Each line shows the contrast at each time of Fig.2.3.

the time when the brightness in AIA 193 Å reaches its peak (Figs. 2.3l and q). This enhancement is insignificant as the intensity increases by only about 5 % over the ambient intensity. This brightening is seen in the Hα images taken at +1.0 Å as a dark structure; that is, it is associated with Hα redshift (Fig. 2.3n, o, s, and t). We show its characteristics more explicitly by calculating the contrast of the redshifted spectra (Fig. 2.4). In addition, the dark ejecta identified in the AIA images is also visible as absorption in the Hα line centre (Fig. 2.3l and q). This ejecta is also seen in the Hα−1.0 Å;thus, it shows blueshifted absorption(Fig. 2.3m, o, r, and t). These results confirm that the dark ejecta identified in the AIA images contain plasma at chromospheric temperatures. After the brightening and blueshift disappear, another redshifted absorption appears near the pixel where the ejecta was originally in the Hα + 1.0 Å (Fig. 2.3x and y). Based on the spatial and temporal consistency with the ejecta observed in the blueshift, this redshift would be the ejecta falling due to gravity.

We found a redshift associated with line centre brightening in the Hα line corresponding to AIA brightening in 14 cases. Previous studies often reported the enhancement at the line centre associated with minifilament eruption (Hermans & Martin, 1986; Sakajiri et al., 2004; Madjarska et al., 2020). However, the redshift with the line centre brightening
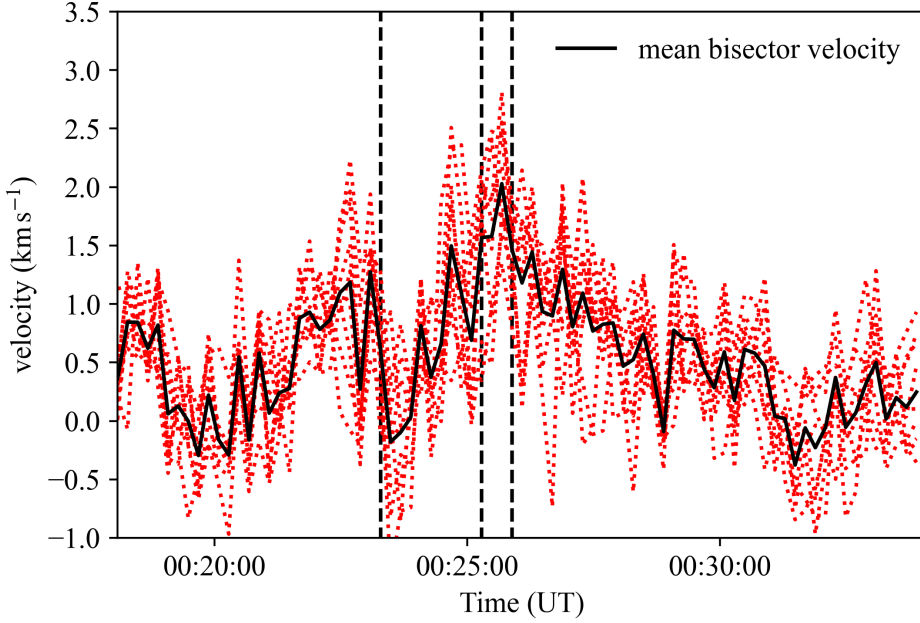
Figure 2.5: Typical example of redshift velocity with brightening in Hα line centre. The event is the same as in Fig. 2.1. The dashed black vertical lines indicate the times in Figs. 2.1e, i, and m, respectively. The dotted red lines indicate the time evolution at each of the pixels surrounded by the white squares in Fig. 2.3. The solid black line shows the average of the dotted red lines.

has rarely been observed in chromospheric spectra (Kontogiannis et al., 2020; Madjarska et al., 2022; Panesar et al., 2022b), and this is the first time it has been investigated in many events. This result indicates that even small flares in the QS can affect the chromosphere. The reason that the brightening and redshift were observed in only half of the events could be attributed to the insufficient spatial resolution of the SDDI. Another reason could be that the energy flux injected into the chromosphere is not extremely large compared to the radiation flux in the chromosphere. We can estimate the thermal conduction flux F_{cond} (in units of $\mathrm{erg\,cm^{-2}\,s^{-1}}$) using the typical physical quantities of the events analysed in this study as follows:

$$F_{\mathrm{cond}} \sim \kappa_0 \frac{T_{\mathrm{DEM}}^{7/2}}{L^2} \simeq 9.0 \times 10^6 \left(\frac{T_{\mathrm{DEM}}}{10^{6.1}\,\mathrm{K}}\right)^{7/2} \left(\frac{L}{2.5 \times 10^8\,\mathrm{cm}}\right)^{-1}, \qquad (2.1)$$

where $\kappa_0 \simeq 10^{-6}$ cgs is the Spitzer thermal conductivity. This value is larger than the energy flux in the chromosphere (upper chromosphere: $3 \times 10^5\,\mathrm{erg\,cm^{-2}\,s^{-1}}$, middle chromosphere: $2 \times 10^6\,\mathrm{erg\,cm^{-2}\,s^{-1}}$, Withbroe & Noyes, 1977) but much smaller than the energy flux of a typical solar flare ($> 10^9\,\mathrm{erg\,cm^{-2}\,s^{-1}}$).

We determined the bisector velocity to characterise the redshift associated with the

brightening of the Hα line centre (Kulander & Jefferies, 1966). We obtained the intensity I_{bis} for determining the bisector velocity as follows:

$$I_{\text{bis}} = I_{\text{H}\alpha}(0\,\text{Å}) + 0.35 \left(\frac{I_{\text{H}\alpha}(+3.0\,\text{Å}) + I_{\text{H}\alpha}(-3.0\,\text{Å})}{2} - I_{\text{H}\alpha}(0\,\text{Å}) \right), \qquad (2.2)$$

where $I_{\text{H}\alpha}(\lambda\,\text{Å})$ is the Hα intensity at wavelengths shifted by $\lambda\,\text{Å}$ from the line centre. With the two wavelengths corresponding to the intensity I_{bis} as λ_+ and λ_-, we determined the bisector velocity v_{red} as follows:

$$v_{\text{red}} = \frac{0.5(\lambda_+ + \lambda_-) - \lambda_0}{\lambda_0} c, \qquad (2.3)$$

where $\lambda_0 = 6562.8\,\text{Å}$ is the Hα line centre wavelength and $c = 3.0 \times 10^5\,\text{km s}^{-1}$ is the light speed. The bisector velocity corresponding to the intensity I_{bis} was determined for each of the 9 pixels where brightening occurred, as shown in Fig. 2.3. We then took the average of these 9 pixels. We show the typical behaviour of the bisector velocity obtained at each time in Fig. 2.5. We can see from Fig. 2.5 that the bisector velocity increases with the brightening. We focused on the average bisector velocity of 9 pixels, and the maximum value of its time evolution was taken as the bisector velocity of the event.

We summarise the bisector velocity for each event in Table 2.1. The events have bisector velocities between $1.0\,\text{km s}^{-1}$ and $5.0\,\text{km s}^{-1}$. These values are slightly larger than the redshift velocity in the steady chromosphere (Chae et al., 1998).

2.3.3 Light Curve

In Fig. 2.6a we show a typical example of a light curve for the analysed events in this study. We obtain the AIA light curves as the sum of the pixels showing brightenings. The light curves are normalised to the maximum value. For the Hα light curve, we use the sum of the intensities of the nine pixels shown in Fig. 2.3. The Hα light curve is also normalised by its maximum value. We can see from Fig. 2.6a that Hα and AIA 304 Å show an earlier intensity increase than AIA 193 Å. This property is consistent with previous studies (Benz & Krucker, 1999; Jin et al., 2021; Madjarska et al., 2022) and is reminiscent of the Neupert effect (Neupert, 1968). Fig. 2.6a also shows that the brightening in the Hα line varies only about 10 % over time.

Fig. 2.6b shows the time evolution of the redshifted velocity associated with line centre brightening and the velocity of the chromospheric ejecta compared to the AIA 193 Å light curve. We used the cloud model (Beckers, 1964; Mein & Mein, 1988) and obtained the line-of-sight velocities of the chromospheric ejecta. We averaged the line-of-sight velocity over the nine pixels shown in Fig. 2.3 and examined its temporal evolution. Fig. 2.6b shows that both the ejecta and the redshifted velocity peaked before the 193 Å light curve
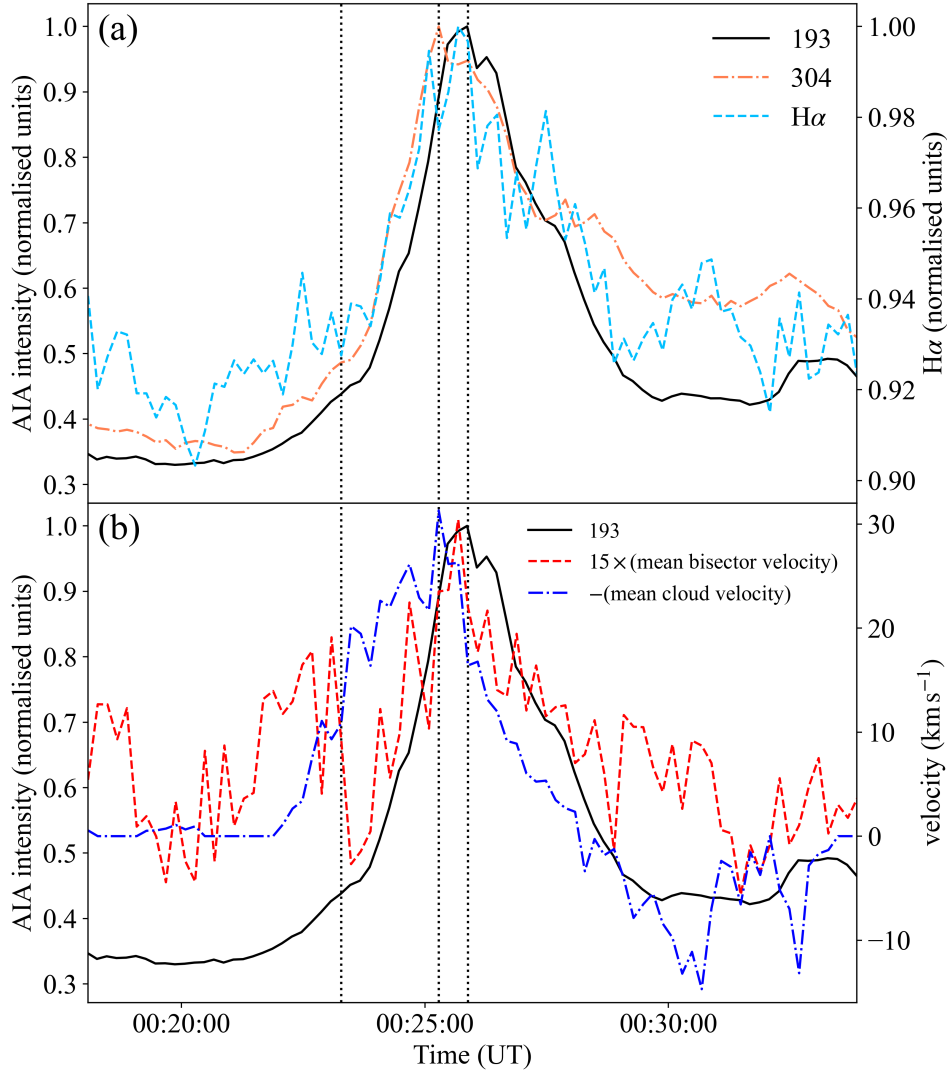
Figure 2.6: Typical examples of the light curves. The event is the same as in Fig. 2.1. The dotted black vertical lines indicate the times in Figs. 2.1e, i, and m, respectively. (a): AIA 193 Å and 304 Å, and Hα line centre light curves. The solid black, dashed light blue, and dash-dotted orange lines indicate the light curves of 193 Å, 304 Å, and Hα line centre, respectively. (b): Comparison of AIA 193 Å light curves with redshift velocities with brightening in Hα centre, and velocities of the dark ejecta. The dashed red and dash-dotted blue lines indicate the velocity of the redshift and the dark ejecta, respectively. The redshift velocity is shown multiplied by a factor of 15. The velocity of the dark ejecta is shown with the sign reversed. Note that the direction toward the observer is defined as a negative velocity.

peak. The ejecta accelerates before the small flare reaches its peak, reaching a maximum value at the same time as the 304 Å light curve. This property is consistent with the standard flare model in which mass ejection triggers magnetic reconnection (Ohyama & Shibata, 1998; Shibata et al., 1995). The redshift velocity is highly variable, and we cannot clearly identify an acceleration phase. However, its peak is synchronised with the Hα line light curve. This fact provides stronger support that the redshift is accompanied by the line centre brightening.

2.4 Discussion

2.4.1 Comparison of Hα redshifted spectra and chromospheric condensation theory

Section 2.3.2 confirmed that Hα line spectra show the line-centre brightening and redshift synchronised with the coronal brightening. Here we discuss the possibility that this redshift corresponds to chromospheric condensation in the small flares in the QS.

The line centre brightening and redshift of the Hα line found in our study are reminiscent of the red asymmetry observed in large-scale flares (Ichimoto & Kurokawa, 1984). In large flare cases, released flare energy is injected into the chromosphere from the corona, resulting in chromospheric condensation (Fisher et al., 1985). The propagation of the condensation shock downward is observed as red asymmetry. The spectra found in this study are not emission lines; however, they are similar to the red asymmetry of large flares in that they show a redshift associated with line centre brightening. This difference is probably because the source function of the Hα line increases due to energy injection from the corona even for small flares in the QS, but the resulting brightening is not large enough for the Hα line to be observed in emission.

Some synthesised Hα profiles corresponding to chromospheric condensation originating from a nanoflare have been reported to have a similar profile to the present observation. Bakke et al. (2022) performed numerical simulations for nanoflares in active regions and produced synthesised profiles of the Hα line. As a result, they reproduced the Hα line spectra, which remain absorption lines but show an increase in the line centre intensity and a redshift (see Bakke et al., 2022, fig. 7). However, their synthesised Hα spectra also show a redshift at the line centre. This is different from our observations, which show almost no shift in the line centres and a redshift only around +1.0 Å. Their calculations also report a phase in which the Hα line becomes an emission line before becoming an absorption line, but we found no Hα emission line in our observation. One reason for these differences is that the spatial and temporal resolution of SDDI (pixel size: 1.23 arcsec/temporal resolution: 12 s) is not as good as the numerical simulations. In other words,
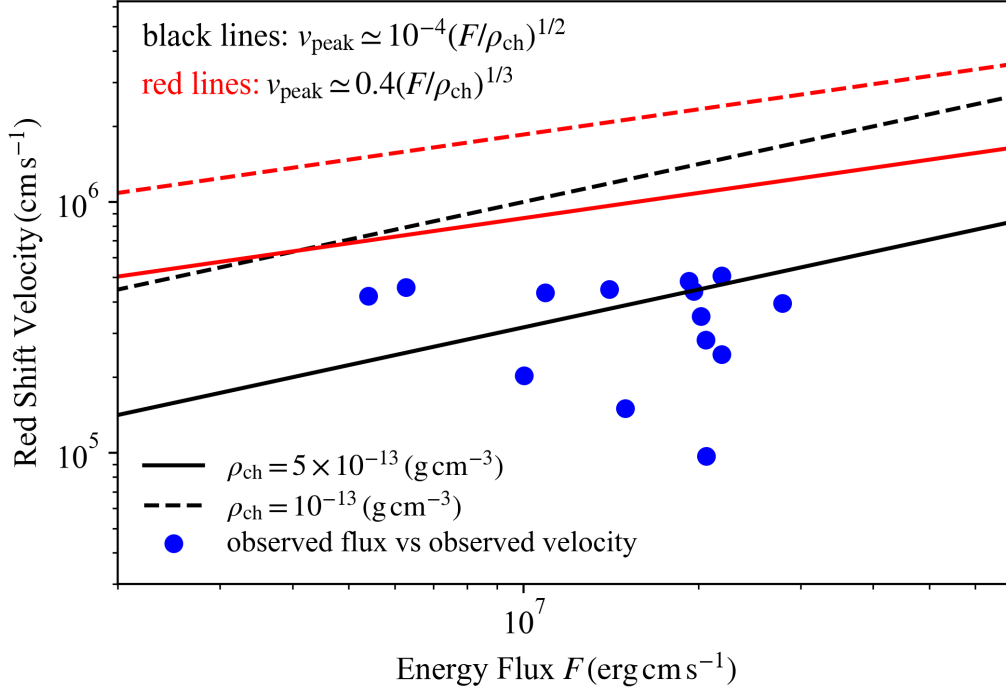
Figure 2.7: Comparison of the observed redshift velocity associated with brightening in the Hα centre with the formula for chromospheric condensation (Fisher, 1989; Longcope, 2014). The black and red lines indicate the Longcope (2014) formula (equation 2.5) and the Fisher (1989) formula (equation 2.4), respectively. The solid and dashed lines show the equations (2.4) and (2.5) assuming different mass densities of the chromosphere, respectively.

we should observe a superposition of spectra from multiple loops, resulting in a difference from the synthetic observation calculated for a single loop. Another reason may be that Bakke et al. (2022) calculated using different parameters than the small loops in the QS.

We compared the observational result with the theoretical formula to verify that the observed spectra are chromospheric condensation. Following two relationships have been proposed between the maximum velocity of chromospheric condensation and the energy flux (Fisher, 1989; Longcope, 2014, in order):

$$v_{\mathrm{peak}} \simeq 0.4 \left(\frac{F}{\rho_{\mathrm{ch}}} \right)^{1/3}, \tag{2.4}$$

$$v_{\mathrm{peak}} \simeq 10^{-4} \left(\frac{F}{\rho_{\mathrm{ch}}} \right)^{1/2}, \tag{2.5}$$

where v_{peak} is the condensation peak velocity (in units of $\mathrm{cm\,s^{-1}}$), F is the injected energy flux into the chromosphere (in units of $\mathrm{erg\,cm^{-2}\,s^{-1}}$), and ρ_{ch} is the mass density in the chromosphere (in units of $\mathrm{g\,cm^{-3}}$). Hence, we compared equations (2.4) and (2.5) with the observations.

Fig. 2.7 compares equations (2.4) and (2.5) and our observations. Here, we assume the thermal conduction fluxes (equation 2.1) for the energy flux F. We can see from Fig. 2.7 that equation (2.5) agrees with the upper bound of the observed velocities. Considering that equation (2.5) corresponds to the maximum condensation velocity, this result supports the interpretation that the spectral variations are due to the chromospheric condensation. In addition, the better agreement of the Longcope (2014) formula than the Fisher (1989) formula is consistent with the case of small-energy flares in the numerical simulation of Ashfield & Longcope (2021).

Another candidate for heated downflow is reconnection outflow, that is, plasma flow accelerated in a current sheet. However, it is unlikely that the observed spectral variations are due to reconnection outflows for the following two reasons. First, the observed redshift velocity is small compared to the Alfvén velocity in the chromosphere. Assuming typical parameters for the upper chromosphere, we can estimate the Alfvén velocity (v_A, in units of $\mathrm{cm\,s^{-1}}$) as follows:

$$v_A = \frac{B_{\mathrm{ch}}}{\sqrt{4\pi\rho_{\mathrm{ch}}}} = 4.0 \times 10^6 \left(\frac{B_{\mathrm{ch}}}{10\,\mathrm{G}}\right)\left(\frac{\rho_{\mathrm{ch}}}{5\times10^{-13}\,\mathrm{g\,cm^{-3}}}\right), \qquad (2.6)$$

where B_{ch} is the magnetic field strength in the upper chromosphere (in units of G). This value is more than ten times larger than our observation. Second, condensation downflow should be easier to observe than reconnection outflow because of its larger spatial scale. Reconnection outflow is collimated thin and stops when it collides with the lower loop. In contrast, the condensation downflow propagates along the top of the lower loop. Hence, it should have a larger spatial scale than the reconnection outflow in a typical magnetic field morphology. Based on the above discussion, although reconnection outflow may be mixed, it is likely that condensation downflow mainly contributed to the Hα spectral variability.

2.4.2 Emission measure vs temperature scaling Law

To understand the physical mechanism of small flares in the QS, we compared the present DEM analysis results with Shibata & Yokoyama (1999, 2002) scaling law. Shibata & Yokoyama (1999, 2002) derived the following scaling law between the volume emission measure EM_v ($\mathrm{cm^{-3}}$) and temperature in the flare peak times:

$$EM_v \simeq 10^{48} \left(\frac{B_{\mathrm{corona}}}{50\,\mathrm{G}}\right)^{-5}\left(\frac{n_0}{10^9\,\mathrm{cm^{-3}}}\right)^{3/2}\left(\frac{T_{\mathrm{peak}}}{10^7\,\mathrm{K}}\right)^{17/2}, \qquad (2.7)$$

where B_{corona} is the coronal magnetic field strength, n_0 is the preflare electron number density, and T_{peak} is the temperature in the flare peak time. This scaling law is consistent with a wide range of energies, from microflares in active regions to giant stellar flares.
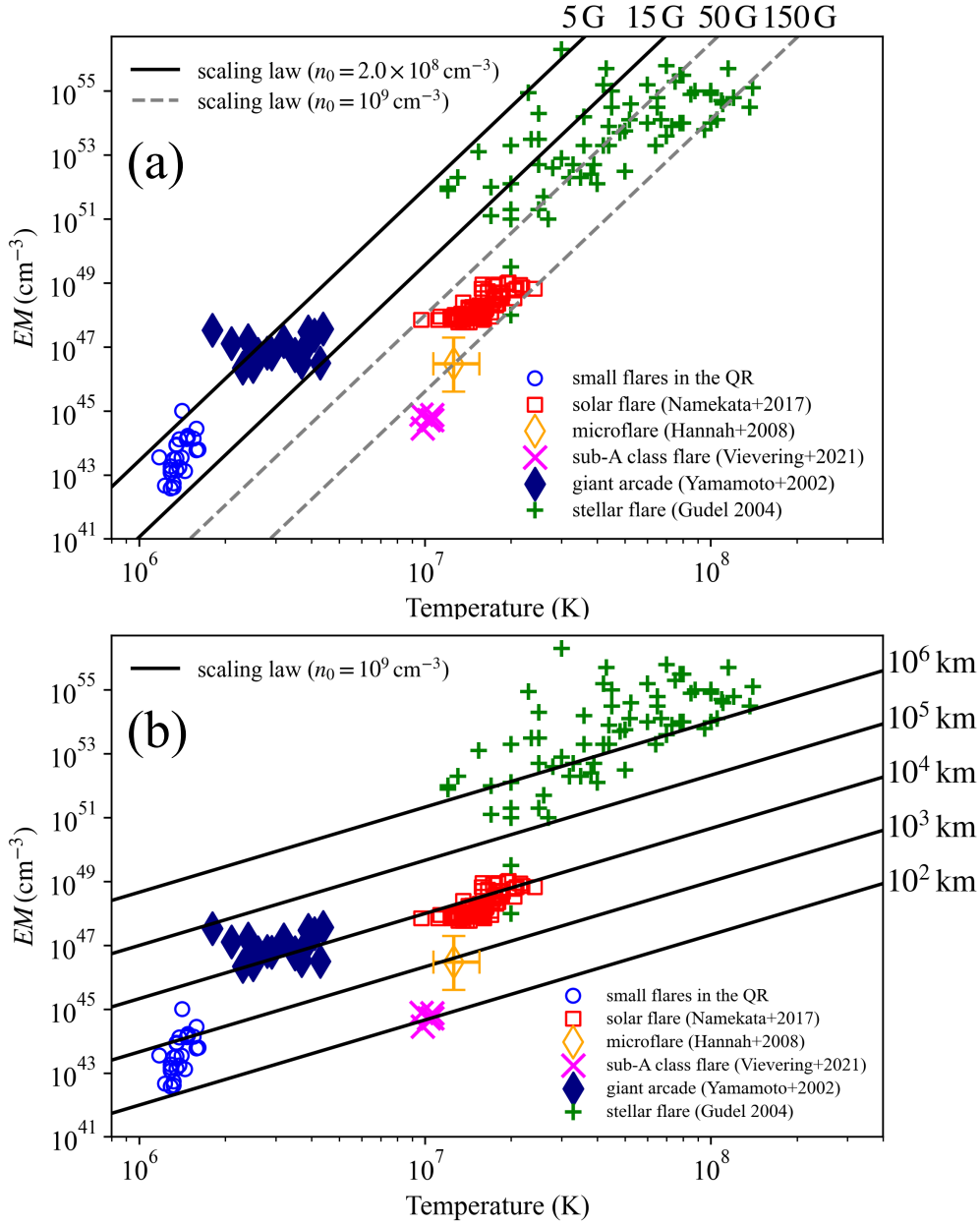
Figure 2.8: Comparison with EM vs temperature scaling law at time of flare peak (Shibata & Yokoyama, 1999, 2002). The blue circles indicate the analysed results of the small flares in the QS in this study. Red squares indicate typical solar flares (Namekata et al., 2017a). The orange diamonds and the pink x-marks indicate microflares (Hannah et al., 2008) and sub-A class flares (Vievering et al., 2021) in active regions, respectively. The dark blue diamonds indicate large flares in the QS (giant arcades, Yamamoto et al., 2002). Green plus signs indicate stellar flares (Güdel, 2004). (a): Comparison with the scaling law (equation 2.7) with the coronal magnetic field strength as a parameter. The solid black and dashed gray lines assume $n_0 = 2 \times 10^8$ cm^{-3} and $n_0 = 10^9$ cm^{-3} for the pre-flare electron density in the corona n_0, respectively. (b): Comparison with the scaling law (equation 2.9) with the spatial scale as a parameter. Since in equation (2.9) n_0 only affects the EM by a power-law index of $2/3$, we assume $n_0 = 10^9$ cm^{-3} for all lines in this figure.

Fig. 2.8 shows the comparison of our analysis result with the scaling law of Shibata & Yokoyama (1999, 2002). Here, the volume emission measure EM_v is calculated from the observations as follows:

$$EM_v = EM \times L^2 \qquad (2.8)$$

We can see from Fig. 2.8a that the present observation agrees with the case where $B_{\mathrm{corona}} = 5 - 15\,\mathrm{G}$ and $n_0 = 2 \times 10^8\,\mathrm{cm}^{-3}$ in equation (2.7). We also include in Fig. 2.8 observations of giant arcades (Yamamoto et al., 2002) for further understanding. The giant arcades are also located away from the group of active region flares and agree with equation (2.7) for $B_{\mathrm{corona}} = 5 - 15\,\mathrm{G}$ and $n_0 = 2 \times 10^8\,\mathrm{cm}^{-3}$. These results indicate that Shibata & Yokoyama (1999, 2002) scaling law can explain small flares in the QS and giant arcades by considering appropriate values of the magnetic field strength and coronal electron density in the QS.

Shibata & Yokoyama (1999, 2002) also derived the scaling law using the spatial scale L rather than the magnetic field B_{corona} as a parameter.

$$EM_v \simeq 10^{48} \left(\frac{L}{10^9\,\mathrm{cm}} \right)^{5/3} \left(\frac{n_0}{10^9\,\mathrm{cm}^{-3}} \right)^{2/3} \left(\frac{T_{\mathrm{peak}}}{10^7\,\mathrm{K}} \right)^{8/3}. \qquad (2.9)$$

We show in Fig. 2.8b our analysis results and equation (2.9). We can see a good agreement with the case where $L \simeq 10^3\,\mathrm{km}$. We can also see that some of the small flares in the QS are consistent with equation (2.9) for the case smaller than $1000\,\mathrm{km}$. These spatial scales are less than the thickness of the chromosphere, which may seem to be a contradictory result. However, we suggest that these spatial scales reflect that only a portion of the loops brightens at coronal temperatures. This hypothesis is consistent with recent "campfire" studies (Berghmans et al., 2021; Zhukov et al., 2021).

Aschwanden et al. (2008) also compared the EM_v and temperature of small flares in the QS with active region flares. They obtained the following relationship by a linear regression fit for various scale solar flares:

$$EM_v \simeq 10^{48.4} \left(\frac{T_{\mathrm{peak}}}{10^7\,\mathrm{K}} \right)^{4.7 \pm 0.1}. \qquad (2.10)$$

The power-law index in this equation differs from those in equations (2.7) and (2.9). The following two reasons can explain this difference. First, Aschwanden et al. (2008) performed the fit without including sub-A class flares in active regions and giant arcades. Equation (2.10) is clearly inconsistent with these events shown in Fig. 2.8. The second reason is that the fitting in Aschwanden et al. (2008) did not consider differences in the physical quantities associated with flares. Aschwanden et al. (2008) performed the fitting simultaneously for flares in quiet and active regions where the magnetic field strength differs. The difference in the magnetic field strength affects the Poynting flux that heats the atmosphere associated with the flare, causing differences in the temperature for same

EM. Hence, the power index should be smaller than the value in equation (2.7) (= $17/2$). From the above discussion, we can say that equation (2.10) is the result of fitting by focusing on only some of the many flares that occur in the solar atmosphere without considering the differences in their parameters. Therefore, it would not be easy to obtain a unified view of flares based on this formula.

We can expect from Fig. 2.8 that the following assumptions of Shibata & Yokoyama's scaling law hold even for small flares in the QS.

(I) Cooling by thermal conduction and heating by magnetic reconnection are balanced.

$$\kappa_0 \frac{T_{\max}^{7/2}}{2L^2} \simeq \frac{B_{\text{corona}}^2}{4\pi} \frac{v_A}{L}, \tag{2.11}$$

where $\kappa_0 \simeq 10^{-6}$ cgs is the Spitzer thermal conductivity, $T_{\max}$ is the maximum temperature in the flare, and v_A is the Alfvén velocity.

(II) The maximum flare temperature $T_{\max}$ is three times higher than the temperature observed at the flare peak time T_{peak}.

(III) The high-temperature, high-density plasma originating from the chromosphere is the origin of the brightening in the corona.

$$EM_v \simeq n^2 L^3, \tag{2.12}$$

where n is the increased flare-loop density.

(IV) The magnetic pressure of the loop confines the high-temperature, high-density plasma originating from the chromosphere.

$$2nk_B T_{\text{peak}} \simeq \frac{B_{\text{corona}}^2}{8\pi}, \tag{2.13}$$

where k_B is the Boltzmann constant.

The fact that small flares in the QS also show these properties is essential for understanding the physical mechanism of nanoflares.

2.4.3 Time evolution of flare temperature and density

We investigated the time evolutions of temperature and density to understand how heating from small reconnection in the QS affects the atmosphere. The time evolution of flare temperature and density has been well studied in large solar flares by numerical simulations and observations (e.g., Nagai, 1980; Serio et al., 1991; Jakimiec et al., 1992; Sylwester et al., 1993; Shibata & Yokoyama, 2002). Reale (2007, 2014) summarised the time evolution of flare temperatures and densities in the following four phases (see Reale, 2007, fig.1. and 2.).
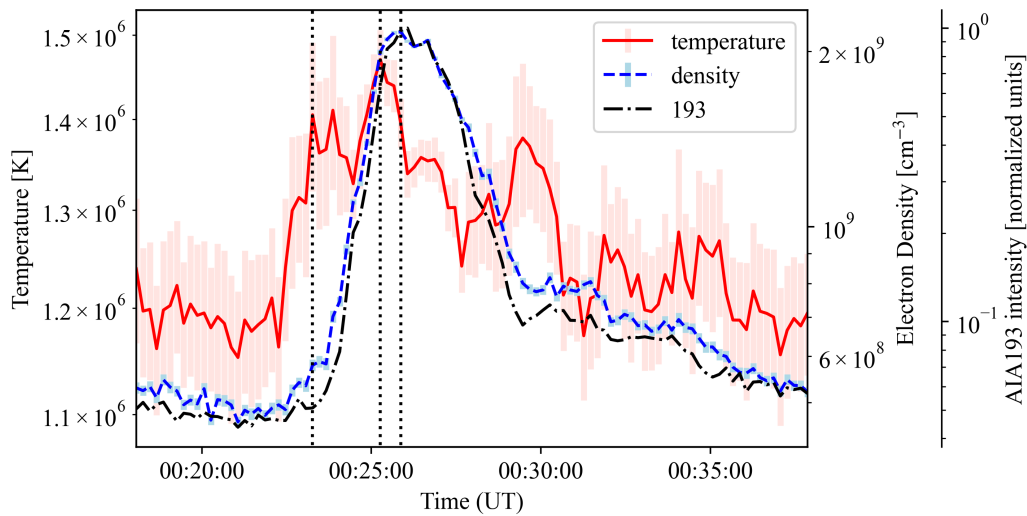
Figure 2.9: Typical example of the time evolution of density and temperature of a small flare. The event is the same as in Fig. 2.1. The dotted black vertical lines indicate the times in Figs. 2.1e, i, and m, respectively. The solid red, dashed blue, and dash-dotted black lines show the time evolution of the temperature, density, and 193 Å intensity, respectively. Error bars of the temperature and density calculations are from the errors in estimating the DEM.

Phase I: From the start of the heat pulse to the temperature peak (*heating*).

Phase II: From the temperature peak to the end of the heat pulse (*evaporation*).

Phase III: From the end of the heat pulse to the density peak (*conductive cooling*).

Phase IV: From the density peak afterwards (*radiative cooling*).

We averaged the temperature and density at 3×3 pixels to investigate the time evolution. To select pixels for the time evolution of temperature and density, we referred to the time when the AIA 193 Å light curve was at its maximum. At that time, we defined the 3×3 pixels, centred on the pixel with the largest AIA 193 Å intensity. We have fixed and limited the analysed pixels to facilitate comparison with the time evolution of the single-loop model (e.g., Jakimiec et al., 1992).

Fig. 2.9 shows a typical example of the time evolution of the density and temperature. We can see from Fig. 2.9 that the temperature increase precedes the density increase. The density and AIA 193 Å light curves reach their peaks almost simultaneously after the temperature peaks. After the density peak, it decays a little more slowly than the AIA 193 Å light curve. The qualitative characteristics of these time evolutions are the same as those of large-scale flares (Reale, 2007, 2014). The result that the temperature increase precedes
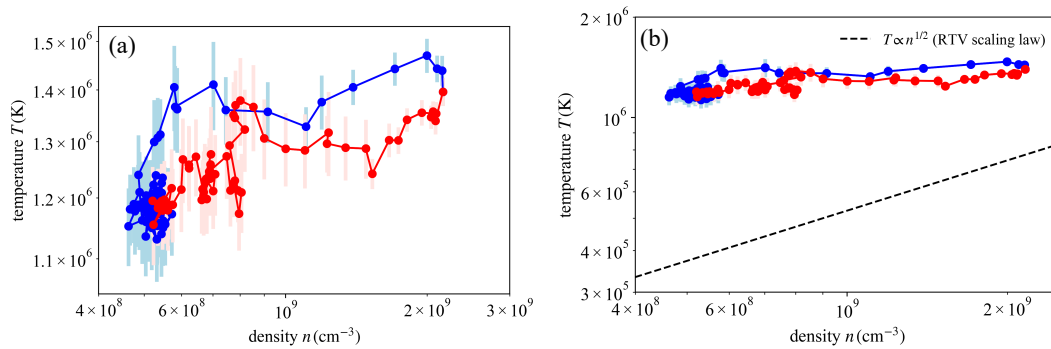
Figure 2.10: Typical example of the temperature-density (T-N) diagram. The event is the same as in Fig. 2.1. (a): T-N diagram shown in large size. (b): Comparison with RTV scaling law (equation 2.14, Rosner et al., 1978). The dashed black line is the RTV scaling law calculated at the spatial scale of event 4 in Table 2.1.

the density increase suggests that chromospheric evaporation occurs even in small flares in the QS. We found 15 events in which the temperature peak preceded the density peak.

We note that the density increase simultaneously with coronal intensity increase was also found by Kamio et al. (2011), who described it as supporting chromospheric evaporation models. However, only the fact that the density increase is synchronised with the coronal brightening is not enough to indicate the presence of chromospheric evaporation. This is because optically thin coronal plasmas are sensitive to density fluctuations. Moreover, numerical simulations suggest that the shocks also cause fluctuations in physical quantities comparable to those of nanoflares (Moriyasu et al., 2004; Antolin et al., 2008). The preceding temperature than the density increase more strongly supports the scenario of energy release that occurs in the corona and propagates to the chromosphere, resulting in evaporation.

Fig. 2.10 shows a typical temperature-density (T-N) diagram for small flares in the QS. From Fig. 2.10a, we can see that the temperature and density increase process is qualitatively the same as for large flares. In contrast, Fig. 2.10b shows that the temperature is about three times higher than that determined by the RTV scaling law (Rosner et al., 1978) in the pre and post-flare phases. The power-law index of the decay phase is gradual and almost constant.

There are multiple reasons for the higher temperatures than expected from the RTV scaling law, even without the occurrence of small flares. The first is the possibility that small loops in the QS are not in a steady state. The second possibility is that the spatial scale determined from the brightening pixels underestimates the actual loop length since brightening is seen only in part of the loop. These underestimations will appear as a
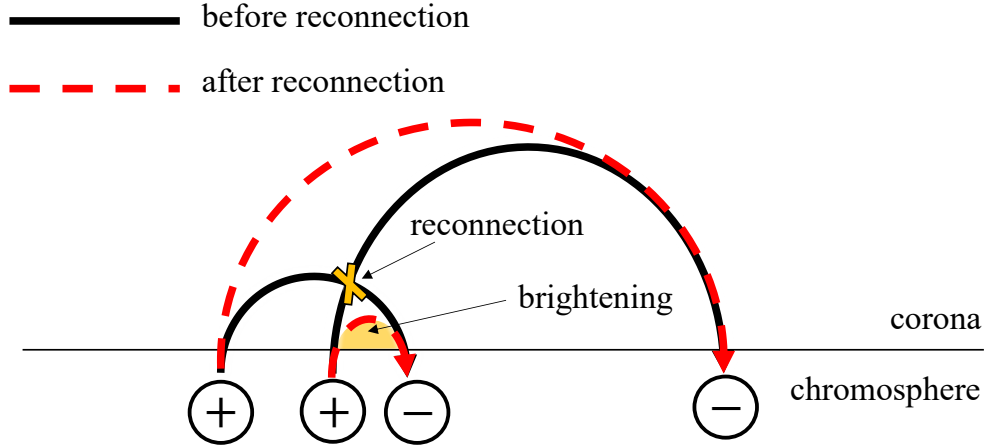
Figure 2.11: Schematic diagram showing an example of a magnetic field morphology that can underestimate the spatial scale.

brightening only near the top of the loop (Berghmans et al., 2021; Zhukov et al., 2021). Also, if the brightening of a small loop formed by reconnection is observed primarily, as in Fig. 2.11, the spatial scale will be underestimated. Then the question to ask is: how much underestimation of the actual loop length would make the temperature consistent with the RTV scaling law when the flare is not occurring? The RTV scaling law for the relationship between temperature and density is as follows:

$$T = 4.3 \times 10^5 \left(\frac{n}{10^9 \, \text{cm}^{-3}} \right)^{1/2} \left(\frac{L}{2.5 \times 10^8 \, \text{cm}} \right)^{1/2} . \qquad (2.14)$$

Therefore, the spatial scale must be underestimated by approximately one order of magnitude.

A third possibility is that the DEM analysis using AIA itself was problematic. The temperature response functions of the six AIA channels used in the DEM analysis have no peak around $10^{5.5} \sim 3.2 \times 10^5$ K (Landi et al., 2013). The smallest temperature peak is about $10^{5.8} \sim 6.3 \times 10^5$ K in AIA 131 Å, which is higher than the temperature of $4.3 \times 10^5 \sim 10^{5.63}$ K expected from the RTV. Therefore, the AIA DEM analysis may not be able to diagnose plasmas that is at a temperature as low as $10^{5.5}$ K. We believe that the AIA DEM analysis may be the most influential in the above three possibilities since the temperature in the absence of flares is about 10^6 K for all events. Hence, the temperatures when flares are not occurring and during the decay phase will need to be investigated differently.

We present two examples of temperature and density temporal evolution showing peculiar behaviour. The first example is events in which the density peak precedes the temperat-
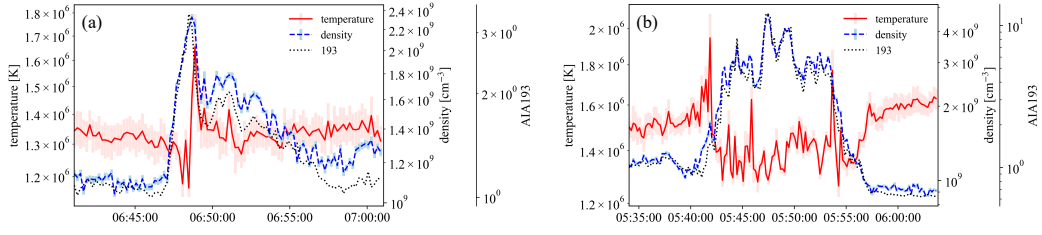
Figure 2.12: Examples of the temperature and density evolution that differ from typical events.

ure peak (Fig. 2.12a). We identified five such examples. One of the causes of these events is the failure to fully resolve the single loop. In other words, the temperature increase corresponding to the density peak may not have been captured by the selected pixels. In such cases, we may capture the temperature increase corresponding to the small brightenings that repeatedly occur after the density peak. Another possibility is that reconnection below the transition region heated the dense plasma to coronal temperatures (Chen et al., 2021). Since the AIA DEM analysis basically describes plasma at coronal temperatures, the observed EM value should increase when plasma at chromospheric/transition region temperatures is heated to coronal temperatures. In such cases, the plasma in the chromosphere/transition region should be heated to coronal temperatures with decreasing density due to expansion. Thus, the observed temperature should peak at or slightly after the density peak.

The second example is that the temperature decreases at the density peak with respect to the pre-flare one (Fig. 2.12b). We identified four such examples. These events occurred at CBPs and had relatively high temperatures ($T \sim 1.5 \times 10^6$ K) before the flares occurred. Therefore, the low temperature ($T \sim 1.2 \times 10^6$ K) plasma is considered to have increased due to chromospheric evaporation, resulting in a decrease in temperature at the density peak. We need to test this hypothesis in the future, including the perspective of what determines the temperature of chromospheric evaporation.

2.5 Summary and future work

This chapter presents our analysis of many small flares in the QS using SDO/AIA and SMART/SDDI observational data, with particular attention to their thermal properties. Our analysis confirmed that the events had physical quantities that were quantitatively consistent with previous studies. We also confirmed common qualitative properties, such as that they occurred at network boundaries and that most of them were accompanied by flux cancellation. The main results of this chapter are as follows:

(i) Redshift with brightening of the Hα line centre was observed in more than half of the events. These redshifts corresponded well to brightenings in the corona both temporally and spatially and were also consistent with the chromospheric condensation formula (Longcope, 2014). Therefore, they are considered to correspond to chromospheric condensation for small flares in the QS (Sections 2.3.2, 2.3.3, and 2.4.1).

(ii) The observed relationship between EM and temperature is consistent with the scaling law (Shibata & Yokoyama, 1999, 2002) for coronal magnetic field strengths of 5–15 G. This consistency suggests that the primary cooling mechanism at the flare peak time is thermal conduction and that the plasma originated from the chromosphere through evaporation significantly affects the brightening. In other words, it suggests that small flares in the QS also have qualitatively the same thermal properties in their peak time, only with reduced magnetic field and spatial scale (Section 2.4.2).

(iii) In more than half of the events, the temperature reached a maximum before the density. This result supports the idea that chromospheric evaporation occurs even in some small flares in the QS (Section 2.4.3).

(iv) Our temperature-density diagram shows that the thermal evolution of small flares always proceeds at higher temperatures than the RTV scaling law (Rosner et al., 1978). One of the reasons for this evolution at high temperatures is the possibility that we overestimate the temperatures in the steady state and decay phase due to the limitation of the observed temperature range by AIA (Section 2.4.3).

These results suggest that the interaction with the chromosphere may play an essential role in the thermal evolution of some small flares in the QS. This property may be the new commonality between small flares in the QS and typical active region flares. However, due to the lack of sample size and spatial resolution, our observations do not accurately answer the question of how many small flares in the QS interact with the chromosphere. Our observations also may not have captured the entire thermal evolution of the small flare in the QS. To solve these problems, simultaneous higher spatial resolution spectroscopic observations of the chromosphere (e.g., with SST/CRISP or DKIST/VTF) and observations capable of diagnosing temperatures from 10^4 to 10^6 K with equally high spatial and temporal resolution (e.g., IRIS or Solar-C/EUVST) will be necessary.

We propose some suggestions based on our results in determining the relationship between the frequency and energy of small flares in the QS. To determine the power-law index of the relationship, we need a proper detection method and method for determining flare energy over a wide energy range. Regarding the flare detection method, our study suggests that using coronal intensity or EM variations may not be able to detect events

that only produce heating without a brightening. This is because the density and coronal intensity showed almost the same time evolution in our analysis, whilst the temperature showed a behaviour independent of them. In other words, because coronal intensity and temperature can be determined independently, we cannot rule out the existence of reconnection, in which the density hardly increases relative to the temperature. This hypothesis would correspond to a QS version of the heating events without X-ray brightening observed in active regions (Ishikawa et al., 2017). The first candidates for such reconnection are small ones in braided field lines (Parker, 1988; Antolin et al., 2021) or weak magnetic fields outside the network boundary. Another candidate, if reconnection occurs in a loop that is already reconnected and highly dense, with radiation cooling as the primary cooling mechanism, would also not cause significant intensity fluctuations. If these events were to occur, how to detect heating (reconnection) events would need to be carefully verified, including numerical verification.

To determine the flare energy, we propose estimating the radiation energy in the chromosphere of a small flare in the QS. The energy partition of flares, including large flares, is an open question. In particular, Warmuth & Mann (2020) has proposed that thermal-nonthermal energy partition changes with flare energy. Hence, using thermal energy as the flare energy may be an inappropriate definition for comparing flares with a wide range of energies. On the other hand, the bolometric radiated energy is considered a good proxy for the dissipated magnetic energy of the flare. The bolometric energy is estimated from variations in the total solar irradiance (TSI) (Kretzschmar, 2011; Emslie et al., 2012), with the main contribution coming from visible and UV wavelengths. It would be impossible to estimate the bolometric energy from TSI variations for small flares in the QS; however, it is possible to estimate the radiative energy of the chromosphere from non-LTE inversion (Yadav et al., 2022). By estimating the radiative energy of the chromosphere for small flares, the flare energy can be defined more accurately, which may help solve the coronal heating problem.

Unified Relationship between Cold Plasma Ejections and Flare Energies Ranging from Solar Microflares to Giant Stellar Flares

3.1 Introduction

[†] Filament eruptions are phenomena in which low-temperature plasma ($\sim 10^4\,\mathrm{K}$) in the solar corona erupts into the interplanetary space, and they are often accompanied by flares and coronal mass ejections (CMEs) (Parenti, 2014). In the standard flare model, filament eruptions are considered to be the trigger of flares (Shibata et al., 1995). Filaments can be broadly classified into active region filaments, quiescent filaments, and intermediate filaments (Mackay et al., 2010), all of which can be erupted. After the filament eruption, post-flare loops are formed in the case of active region filament eruptions, and giant arcades are formed in the case of quiescent filament eruptions. Post-flare loops and giant arcades have different X-ray intensities and spatial scales, but their morphologies are similar. Therefore, both of these phenomena are considered to be explained by the standard flare model (Shibata & Magara, 2011).

The typical length of an ejected filament ranges from 10^4 to $10^5\,\mathrm{km}$, but signatures of smaller/larger spatial scale ejections of cold plasma with flares have also been observed. Small plasma ejections with chromospheric temperatures over 10^3 to $10^4\,\mathrm{km}$ (called mini-filaments) occur in the Sun and are considered miniature versions of filament eruptions. These small phenomena were first discovered in the quiet region in the 1970s (Moore

---

[†]This chapter is based on Kotani et al. (2022)

et al., 1977; Labonte, 1979). Hermans & Martin (1986) performed the first comprehensive study by Hα observation. Subsequent observations showed that they were accompanied by extreme ultraviolet (EUV) small flares (Sakajiri et al., 2004; Ren et al., 2008). These early studies also revealed that minifilament eruptions are associated with magnetic flux cancellation. In addition, minifilament eruptions are often accompanied by coronal waves and mini-CMEs (Innes et al., 2009; Podladchikova et al., 2010; Schrijver, 2010). Several studies reported that minifilament eruption contributes to the EUV jet formation with flux cancellation (e.g., Sterling et al., 2015). These previous studies suggest that minifilament eruptions have common properties with filament eruptions and flares, and recent observations with high spatial resolution have supported the same conclusion (Kontogiannis et al., 2020; Chen et al., 2020; Jin et al., 2021). Cold plasma ejections have also been found with campfires, which are smaller EUV brightenings recently discovered by the Solar Orbiter/Extreme Ultraviolet Imager (Panesar et al., 2021; Berghmans et al., 2021). Considering the scale-free self-similar characteristics of magnetohydrodynamics, we can expect similar phenomena at smaller scales (Kotani & Shibata, 2020). Even in the case of stellar flares occurring on M-type stars, which are sometimes much stronger than solar flares, blue asymmetry has been found in spectral profiles of the chromospheric lines (Houdebine et al., 1990; Vida et al., 2016, 2019; Honda et al., 2018; Moschou et al., 2019; Maehara et al., 2021). A plausible interpretation is that the blue asymmetry represents cold plasma ejections associated with stellar flares. Also, a blue shift in the Hα absorption line has been found with a superflare in G-type stars(Namekata et al., 2022b). Because of its similarity to filament eruptions on the Sun, it is reasonable to interpret this as large cold plasma ejections associated with a stellar flare.

Cold plasma ejections occur over a wide range of flare energy spanning more than ten orders of magnitude ($10^{25} - 10^{35}$ erg). In contrast, the relationships between their physical parameters (such as ejection mass, kinetic energy, and velocity) and flare energy have not been studied quantitatively as a common framework. The ejection mass and flare energy have been estimated by spectral observation of the stellar chromosphere in the stellar flare studies (Moschou et al., 2019; Maehara et al., 2021; Namekata et al., 2022b). These stellar studies report that the stellar flare energy and the mass of associated ejecta could be interpreted as an extension of the solar CMEs. However, there should be a significant gap in the temperature and observable height of the target between the solar CMEs observation using coronagraphs and the observation of cold plasma ejections using chromospheric lines. Therefore, the cold plasma ejections associated with stellar flares are strictly speaking in a different framework than the solar CMEs. The stellar cold plasma ejections should be compared to the solar cold plasma ejections. Namekata et al. (2022b) has compared solar filament eruptions with stellar cases, but the number of samples is only five (Jain & Sorathia, 1987; Ohyama & Shibata, 1999; Christian et al., 2015; Namekata et al., 2022b). In addition, to our knowledge, the flare energy and the ejection mass of events smaller than

10^{27} erg have never been quantitatively studied. To investigate the correlation between the physical quantities of the cold ejecta and the flare energy over a wide energy range, a larger sample of flares, including those below 10^{27} erg, needs to be examined.

In this study, we performed a statistical spectral analysis of small mass ejections associated with small flares in the quiet region of the Sun (energy $10^{25} - 10^{27}$ erg) and filament eruptions associated with solar flares (energy $10^{27} - 10^{29}$ erg) using the *Solar Dynamics Doppler Imager* (SDDI: Ichimoto et al., 2017) on the *Solar Magnetic Activity Research Telescope* (SMART: UeNo et al., 2004). By adding small events to the sample of large events, including the stellar flares, this study aims to investigate the correlation between the flare energy and the physical parameters of cold plasma ejecta over the energy range of $10^{25} - 10^{35}$ erg. We analyzed small-scale ($10^{25} - 10^{27}$ erg) phenomena that have common properties with minifilament eruption, such as line-of-sight velocity, lifetime, and appearance with small flares (=EUV brightening) (Figures 3.1 and 3.2). Because shapes of the small ejecta are ambiguous due to the insufficient spatial resolution of Hα observation, we refer to the small phenomenon to be analyzed in this article as "small mass ejections associated with small flares in the quiet region" rather than "mini filament eruption."

We also constructed a theoretical scaling law between the total flare energy[*] and the mass of ejected filament and compared it with our observation results. Using this scaling law, we attempt to understand cold plasma ejections associated with flares of various scales in a unified way.

3.2 Observation and data analysis

We used SMART/SDDI to detect cold plasma ejections. SDDI at Hida Observatory of Kyoto University takes the solar full-disk images at 73 wavelengths from H$\alpha - 9.0$ Å to H$\alpha + 9.0$ Å with a constant wavelength step of 0.25 Å. The temporal resolution and the pixel size are 12 s and 1.23 arcsec, respectively. The data were processed for dark and flat field correction.

3.2.1 Small mass ejections associated with small flares in the quiet region

We used the SDDI data taken from 21:56:17 UT on September 6, 2019 to 8:32:40 UT on September 7, 2019 to detect the small mass ejections in the quiet region. In this case,

---

[*]This chapter use the term "total flare energy" as an alternative to dissipated magnetic energy in magnetic reconnection. Dissipated magnetic energy may be best suited to define the flare energy over a wide range of energies; however, it is difficult to estimate directly from observations. On the other hand, the kinetic energy and the energies related to the flare radiation (bolometric, non-thermal and thermal) can be estimated from observations. In addition, the dissipated magnetic energy is mainly accounted for by kinetic and radiation-related energies (Emslie et al., 2012). Therefore, we define the "total flare energy" as the sum of the kinetic energy of the cold plasma and the energy related to the flare radiation (see Section 3.2).
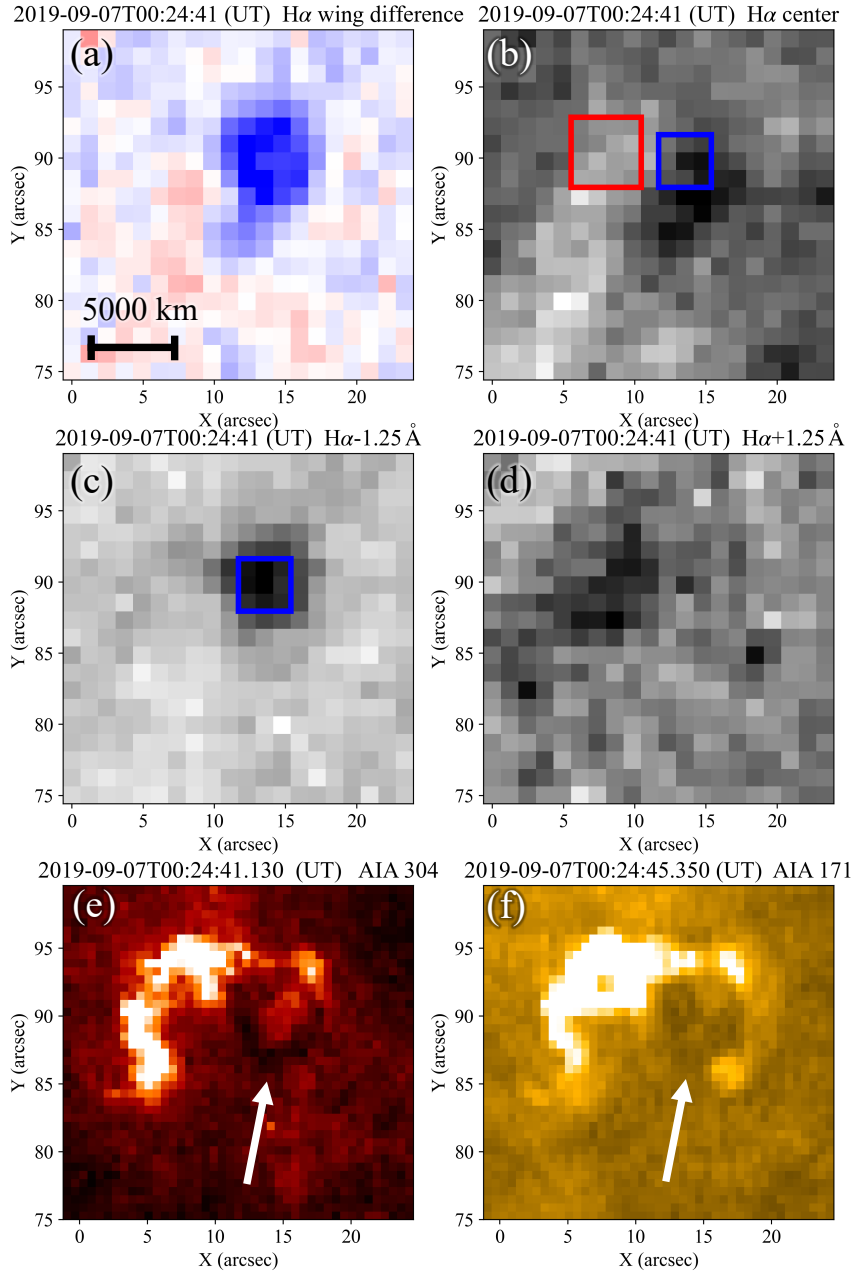
Figure 3.1: A typical example of a small mass ejection in the quiet region with a small flare. (a) Hα wing difference image. This image is created by subtracting the counts from H$\alpha + 1.25$ Å to $+2.0$ Å from the counts from H$\alpha - 1.25$ Å to -2.0 Å. For the colors in this figure, blue and red represent dark and bright features corresponding to the blue and red shifts. (b) Hα line center intensity. The red and blue squares represent the area where the Hα's light curve was calculated and the temporal variation of the line-of-sight velocity were calculated in Figure 3.2, respectively. (c), (d) Intensities at H$\alpha \pm 1.25$ Å. The blue square is the same with that in panel (b). (e), (f) AIA 304 Å and 171 Å intensities. The white arrows indicate mass ejections.
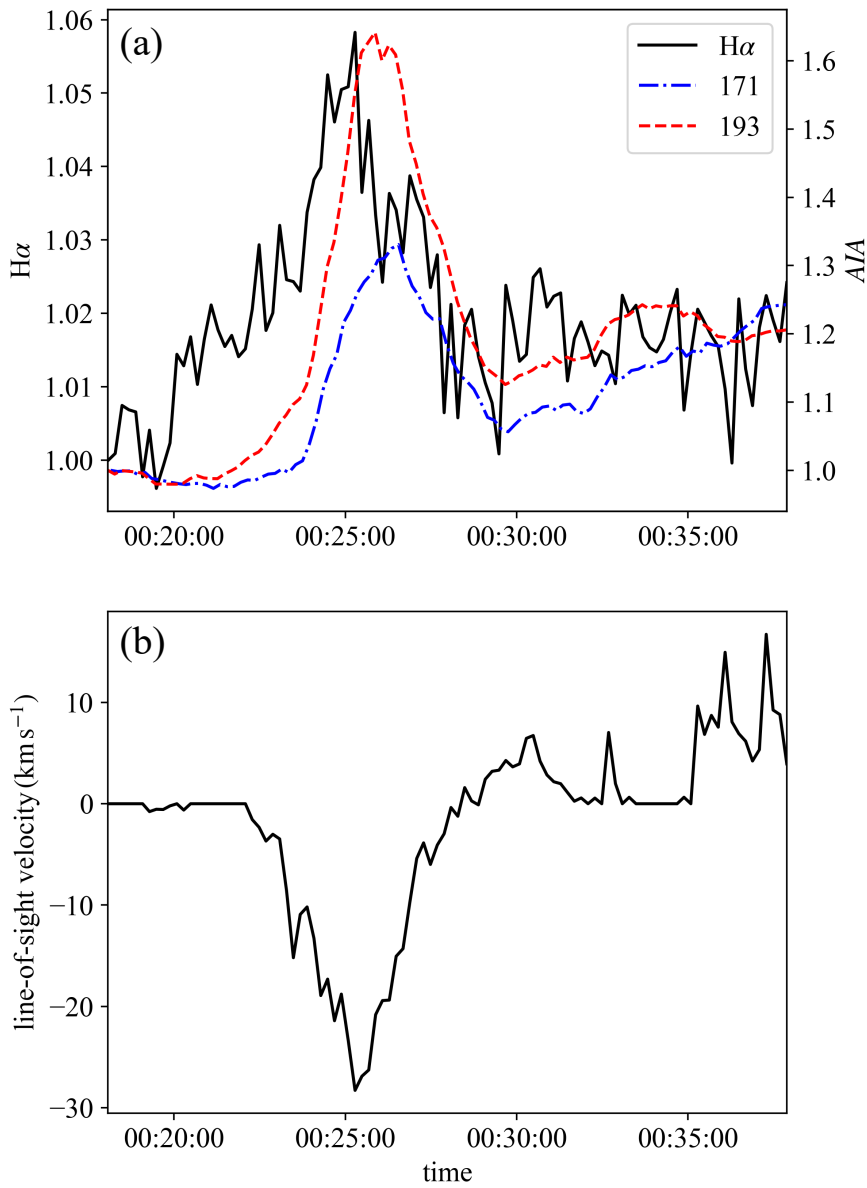
Figure 3.2: (a) Light curves of Hα center (solid black), AIA 171 Å (dash-dotted blue), and 193 Å (dashed red). Hα brightness is calculated as the average over the red square region in Figure 3.1b, and 171 Å AIA 193 Å are calculated as the average over the entire field of view in Figure 3.1f. Each light curve is normalized by its initial brightness at 00:18 (UT). (b) Temporal variation of the line-of-sight velocity of the small mass ejection. The line-of-sight velocity is calculated by averaging those obtained by the cloud model fitting in the blue squares in Figure 3.1b. A negative value represents a blue shift, and a positive value represents a red shift.
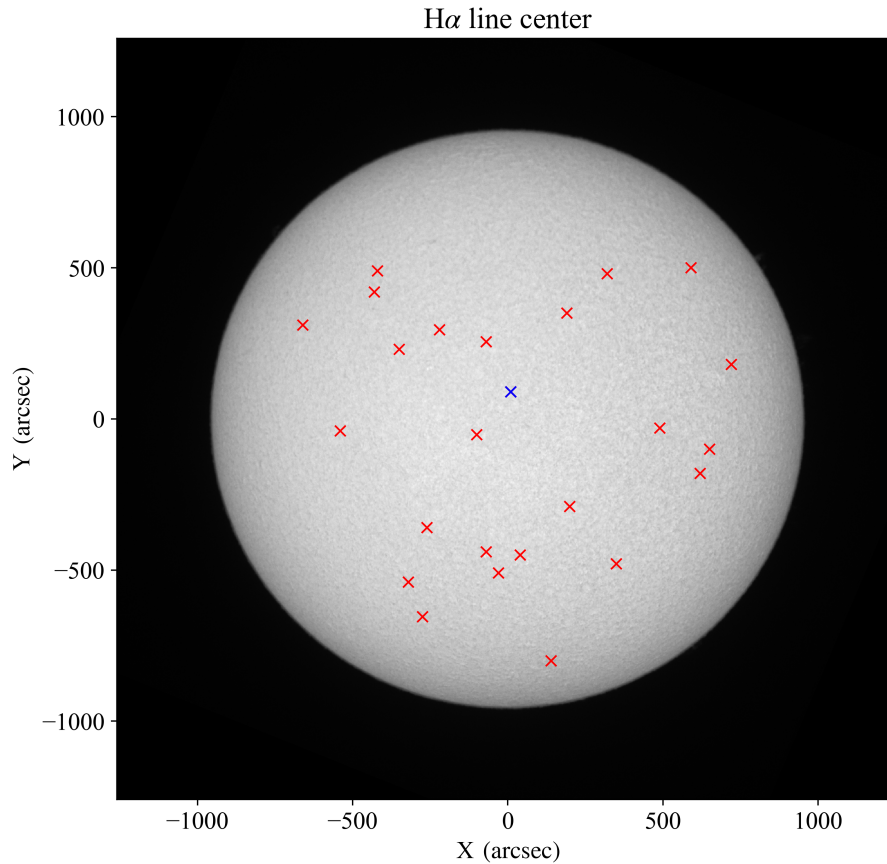
Figure 3.3: Solar full-disk image observed by SMART/SDDI at the Hα line center on September 7, 2019. The red crosses indicate the locations of the small mass ejections used in the analysis. The blue cross indicates the event shown in Figures 3.1 and 3.2.

we used 25 wavelengths covering from $H\alpha - 3.0$ Å to $H\alpha + 3.0$ Å because this range is sufficient to capture our targets. On this day, neither sunspots, large plage regions, nor large filaments were present on the solar disk (Figure 3.3). Although the Sun was tranquil, tiny spatial dimming was frequently observed in the Hα blue wing.

We analyzed 25 events that satisfied the following conditions.

- They showed clear dark features in "Hα wing difference images", which corresponded to the blue shift due to the fast mass ejections. We made these wing difference images by subtracting "the average of the counts from $H\alpha + 1.25$ Å to $+2.0$ Å" from "the average of the counts from $H\alpha - 1.25$ Å to -2.0 Å" at each time. These dark structures include pixels where the difference counts are larger than 4σ ($\sigma =$ the standard deviation calculated from the surrounding pixels).

- They were located within approximately $60°$ from the disk center.

Figure 3.4: Diagrams showing how the length L, width, and line-of-sight length d of cold ejecta are defined. (a) Typical example for the approximation of cold ejecta as a quadrangle. The color bar indicates the line-of-sight velocity $(\mathrm{km\,s^{-1}})$. The red and black lines indicate the opposite sides corresponding to width and length L, respectively. (b) Schematic diagram of the eruption assumed in this study. d is the line-of-sight length.
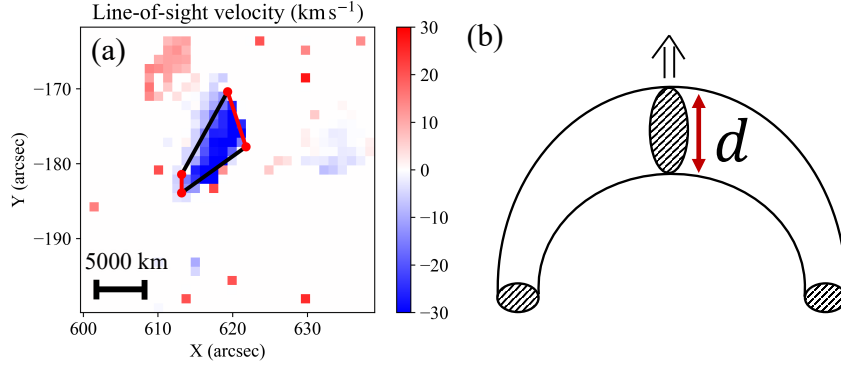
- They were associated with EUV brightening in images taken by the *Atmospheric Imaging Assembly* (AIA) onboard *Solar Dynamics Observatory* (SDO) (Pesnell et al., 2012; Lemen et al., 2012). As described in detail later, we checked for the presence of areas at least three times brighter than the surroundings as a criterion for brightness.

Locations of the selected 25 events are shown in Figure 3.3. Figures 3.1 and 3.2 show a typical example of the event and its time development.

To estimate the kinetic energy and mass of the ejecting plasma, we performed cloud model fitting (Beckers, 1964; Mein & Mein, 1988) to determine the line-of-sight velocity v_l (in units of $\mathrm{cm\,s^{-1}}$), optical thickness of the ejecting plasma τ_0, source function S, and Doppler width $\Delta\lambda_D$ (in units of Å). Using the fitting results, we counted the number of pixels A_{ejecta} where the blue shift was greater than $10\,\mathrm{km\,s^{-1}}$ and defined it as the area of the ejections.

We estimated the physical quantities of each event when the sum of v_l^2 in region A_{ejecta} reached the maximum. The sum of v_l^2 can be regarded as a measure of the kinetic energy of the ejection if the mass column density is uniform over the ejection. To estimate the hydrogen density n_H (in units of $\mathrm{cm^{-3}}$), the second level hydrogen density $n_2{}^*$ (in units of $\mathrm{cm^{-3}}$) was obtained from the results of the cloud model fitting as follows (Tsiropoula & Schmieder, 1997):

$$n_2 = 7.26 \times 10^{12} \frac{\tau_0 \Delta\lambda_D}{d}\,\mathrm{cm^{-3}}, \tag{3.1}$$

$^*n_2$ includes the effect of the filling factor. This is because τ_0 and $\Delta\lambda_D$ are determined from the spectrum whose signal is weakened by the filling factor.

where d is the line-of-sight length of the ejecta (in units of cm). We approximated A_{ejecta} as a quadrilateral by selecting the four endpoints, as shown in Figure 3.4a. We calculated the average of the opposite side lengths of the quadrangle, respectively, and defined the shorter and longer sides as the width and length L of the ejecta. Assuming that the cold plasma erupts in a cylinder-like structure (Figure 3.4b), we defined the line-of-sight length d as equal to the width. We estimated n_H, column density M_{col} (g cm^{-2}), and mass density ρ (g cm^{-3}) from the n_2 values in each pixel as follows (Tsiropoula & Schmieder, 1997):

$$n_H \quad = 5.01 \times 10^8 \sqrt{n_2}, \tag{3.2}$$

$$M_{\mathrm{col}} \quad = (n_H m_H + 0.0851 n_H \times 3.97 m_H)d, \tag{3.3}$$

$$\rho \quad = \frac{M_{col}}{d}, \tag{3.4}$$

where $m_H = 1.67 \times 10^{-24}$ g is the mass of the hydrogen atom. Using equation (3.3), we obtained the mass M (g) and kinetic energy E_k (erg) of the ejecting plasma by summing over the pixels in region A_{filament};

$$M \quad = \sum_A M_{\mathrm{col}} \times (\text{SDDI pixel size})^2, \tag{3.5}$$

$$E_k \quad = \sum_A \frac{1}{2}\rho v_l^2 \times (\text{SDDI pixel size})^2 \times d, \tag{3.6}$$

where SDDI pixel size $= 1.23\,\mathrm{arcsec} = 8.99 \times 10^7$ cm.

To determine the total flare energy, we estimated the thermal energy of the small flare by the differential emission measure (DEM) from the AIA 6 channels. The analysis was performed for the dataset at the peak time of AIA 193 Å light curve. We extracted the areas where the intensity of AIA 171 Å and 193 Å was more than five times brighter than the surrounding area and where AIA 131 Å and 211 Å were more than seven times brighter than the surrounding area. These areas were combined to determine the region for DEM analysis. In three events, the intensity of the surrounding area was high, or the brightening was low, and we could not extract the area for DEM analysis by the above method. In these cases, we determined the area for DEM analysis with the threshold of AIA 171Å and 193 Å intensity as three times, and AIA 131 Å and 211 Å intensity as five times. We defined the spatial scale of the flare L_{flare} (in units of cm) by taking the square root of the area where the DEM analysis was performed.

We performed the DEM analysis using the method of Hannah & Kontar (2012). We used AIA level 1.5 data generated by sunpy's aiapy.calibrate as input values for the DEM analysis. We determined the DEM in the range $5.5 \leq \log T \leq 6.7$ with a step of $d \log T = 0.05$. After obtaining the DEM, we calculated the emission measure $EM\,(\mathrm{cm}^{-5})$, DEM-weighted temperature T_{DEM} (K), and electron density n_e (cm^{-3}) at each pixel using the

following relations:

$$EM = \int DEM(T)dT \tag{3.7}$$

$$T_{DEM} = \frac{\int DEM(T) \times T dT}{\int DEM(T)dT} \tag{3.8}$$

$$n_e = \sqrt{\frac{EM}{L_{\text{flare}}}}. \tag{3.9}$$

We used these values to obtain the thermal energy of the small flare E_{th} (in units of erg) by summing over all pixels for which the DEM analysis was performed.

$$E_{th} = \sum 3n_e k_B T_{DEM}, \tag{3.10}$$

where k_B is Boltzmann constant.

We determined the total flare energy E_{tot} (erg) as the sum of the kinetic energy of the cold ejection and the thermal energy for small flares cases. Previous studies for the energy partition of flares have suggested that bolometric energy is a good alternative for energies related to flare radiation (Emslie et al., 2012). However, we could not estimate the bolometric energy because all the small flares analyzed in this study are sub-A class flares. On the other hand, Warmuth & Mann (2020) have proposed that the contribution of non-thermal energy decreases as the flare energy decreases. We, therefore, followed the hypothesis of Warmuth & Mann (2020) and used thermal energy as a bolometric energy substitute, neglecting the non-thermal energy contribution.

Distributions of the physical quantities thus obtained are shown in Figure 3.5a-3.5d. The result of the line-of-sight velocities in this study (Figure 3.5a) is larger than those by Kontogiannis et al. (2020), which reported about $10\,\text{km}\,\text{s}^{-1}$, also based on the cloud model. This is probably because we used Hα wing difference images from ± 1.25 Å to ± 2.0 Å in our event selection, which is sensitive to faster velocity movements. Spatial scale, temperature, and EM for small-scale flares (Figures 3.5b, 3.5c, and 3.5d, respectively) are comparable to or slightly greater than those studied for the larger "campfires" (Berghmans et al., 2021). Note that we have obtained the temperature and EM for each event by averaging the physical quantities for pixels where the DEM analysis was performed. We can confirm from Figure 3.5 that we are indeed analyzing a small flare associated with a cold plasma ejection.

3.2.2 Filament eruptions with solar flares

To perform the similar study for large filament eruptions, we used the SMART/SDDI filament disappearance catalog* (Seki et al., 2019) as the data source. From this catalog, we

---

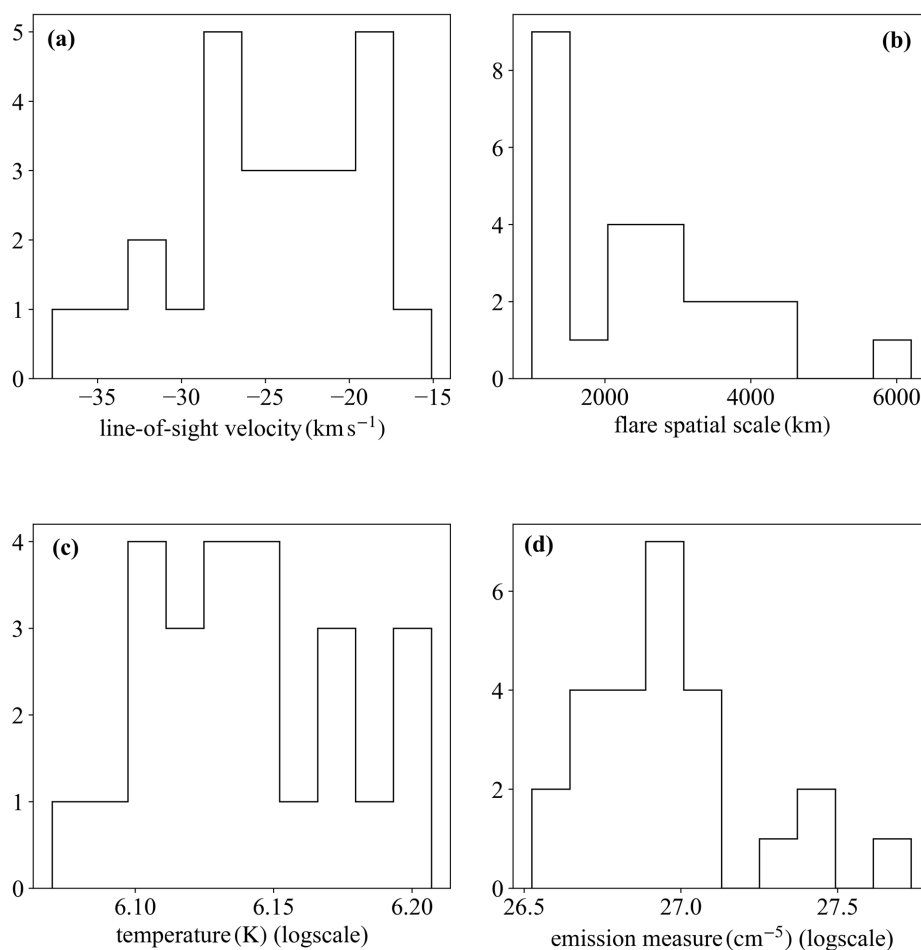*https://www.kwasan.kyoto-u.ac.jp/observation/event/sddi-catalogue/

Figure 3.5: Histograms of the physical parameters of 25 events analyzed in this study. (a) Line-of-sight velocity of the cold plasma ejection obtained by the cloud model. (b)-(d) Spatial scale, temperature, and EM for small-scale flares.

selected events near the disk center that were accompanied by flares. Under this criterion, we selected six active region filaments and four intermediate filaments; in total, ten cases were analyzed in this study.

We estimated the kinetic energy of the filament eruption using the cloud model fitting in the same way as the small mass ejections. The analysis was performed for the period when the radial velocities of the eruption got maximum. We estimated the bolometric energy by assuming that the GOES flare index is proportional to the bolometric energy and that the bolometric energy of the M1.0-class flare corresponds to 10^{30} erg (Shibata et al., 2013; Namekata et al., 2022b). As a result, we obtained the total flare energy as the sum of the kinetic energy of the filament eruption and the bolometric flare energy.

3.3 Results

Figure 3.6a shows the relationship between total flare energy and ejected mass for the events analyzed in this study. The correlation coefficients between the ejected mass and total flare energy for the small mass ejections in the quiet region r_{small} and filament eruptions r_{large} are 0.60 and 0.49, respectively. The 95% confidence intervals for the respective correlation coefficients are $0.27 < r_{small} < 0.80$ and $-0.21 < r_{large} < 0.85$. These values confirm a positive correlation between total flare energy and ejection mass at least in small event cases. In the large filament eruption cases, we cannot claim a positive correlation from only these values, but this may be due to the small sample number of 10. The correlation coefficient of all events analyzed in this study r_{all} is $r_{all} = 0.85$ and its 95% confidence intervals is $0.73 < r_{all} < 0.92$, suggesting a strong correlation over a wide range of energies as expected. Linear fitting of the logarithms of the ejected mass and flare energy results in $M \propto E_{tot}^{0.61\pm0.25}$ for small mass ejections in the quiet region and $M \propto E_{tot}^{0.59\pm0.22}$ for filament eruptions, where the uncertainties are given by assuming the error in mass by a factor of three. For all events analyzed in this study, $M \propto E_{tot}^{0.46\pm0.06}$ was obtained. It is noticed that the power-law index was reduced compared to the individual cases.

In Figure 3.6b, we include other examples of solar filament eruption (Jain & Sorathia, 1987; Ohyama & Shibata, 1999; Christian et al., 2015; Namekata et al., 2022b) and the blue shifts accompanied by the stellar flares interpreted as stellar filament eruptions (Moschou et al., 2019; Maehara et al., 2021; Namekata et al., 2022b) with the present analysis. We assumed $E_{tot} = 100E_X + E_{kin}$ in the M-type star cases (Moschou et al., 2019; Maehara et al., 2021) and $E_{tot} = E_{bol} + E_{kin}$ in the G-type star case (Namekata et al., 2022b), where E_X is the X-ray energy in the GOES $1-8$ Å band of the stellar flares estimated from their Hα energy, E_{kin} is the kinetic energy of the ejecta, and E_{bol} is the bolometric energy of white-light flare. We can see a strong correlation between total flare energy and ejection mass over a wide range of energies in Figure 3.6b. The correlation coefficient $r_{all\_previous}$, which includes both previous studies and stellar cases, increased to $r_{all\_previous} = 0.90$ and its 95% confidence intervals is $0.83 < r_{all\_previous} < 0.95$.

In Figure 3.6b, we include the mass-total flare energy relation for the solar CMEs (Aschwanden, 2016). The total flare energy associated with CMEs is estimated in the same way as in the case of solar filament eruptions. As a result, CMEs and cold plasma ejections show similar trends. This trend is consistent with the scaling law for CMEs $M_{CME} \propto E_{tot}^{2/3}$ derived by Takahashi et al. (2016). Observational studies of solar CMEs using X-ray flux and fluence as the flare energy also report power-law indexes close to 2/3 (0.70: Aarnio et al. 2011, 0.59: Drake et al. 2013).

Figure 3.7 shows the relationship between total flare energy and kinetic energy of ejec-
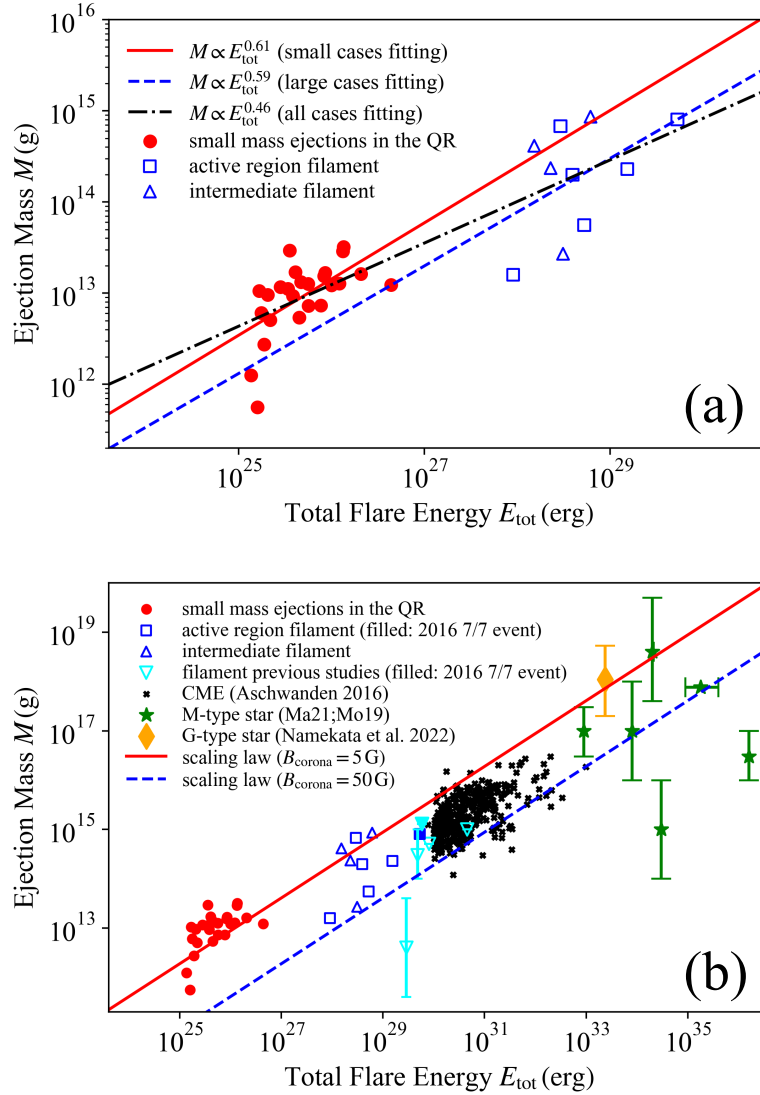
Figure 3.6: (a) Relationship between total flare energy and ejected mass for events analyzed in this study. The red circles, blue squares, and blue triangles represent small mass ejections in the quiet region, the active region filament, and the intermediate filament eruptions, respectively. The solid red and dashed blue lines show the results of fitting for red symbols and blue symbols, respectively. The dash-dotted black line shows the fitting of all events in this figure. (b) Comparison of the present study with previous studies. The light blue triangles represent filament eruptions in previous studies (Jain & Sorathia, 1987; Ohyama & Shibata, 1999; Christian et al., 2015; Namekata et al., 2022b). The filled blue square and light blue triangle represent the same event, the July 7, 2016 filament eruption analyzed in Namekata et al. (2022b). The black crosses represent CMEs (Aschwanden, 2016). The green stars and orange diamond represent signs of cold plasma ejections with stellar flares on M-type (Moschou et al., 2019; Maehara et al., 2021, shown Mo19 and Ma21 in the figure) and G-type stars (Namekata et al., 2022b), respectively. The solid red line and the dashed blue line show the cases of $B_{\mathrm{corona}} = 5\,\mathrm{G}$ and $B_{\mathrm{corona}} = 50\,\mathrm{G}$ in the scaling law (3.12), respectively. We assume the energy conversion rate $f = 0.1$ in equation (3.12) in both lines.
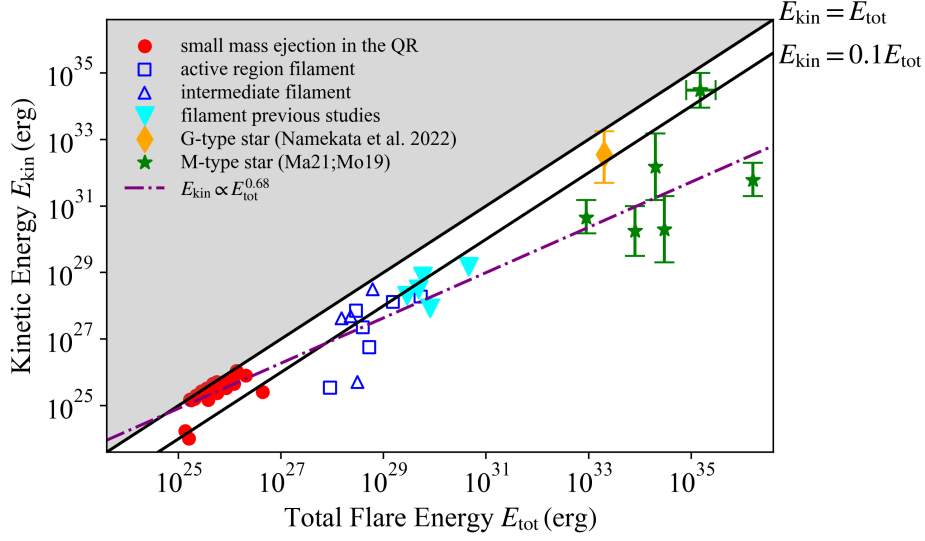
Figure 3.7: Same as Figure 3.6 but for the kinetic energy. The solid black lines shows $E_{\mathrm{kin}} = E_{\mathrm{tot}}$ and $E_{\mathrm{kin}} = 0.1E_{\mathrm{tot}}$, respectively. The dash-dotted purple line shows the fitting of all events in Figure 3.6a. The gray region shows $E_{\mathrm{kin}} > E_{\mathrm{tot}}$.

Figure 3.8: Same as Figure 3.6 but for the line-of-sight velocity. The dash-dotted purple line shows the fitting of all events in Figure 3.6a. The solid black line show $v \propto E_{\mathrm{tot}}^{1/6}$ relation.

tion for events analyzed in this study. From this figure, we can see that the kinetic energy accounts for a larger percentage of the total energy for small ejections in the quiet region, while it becomes sm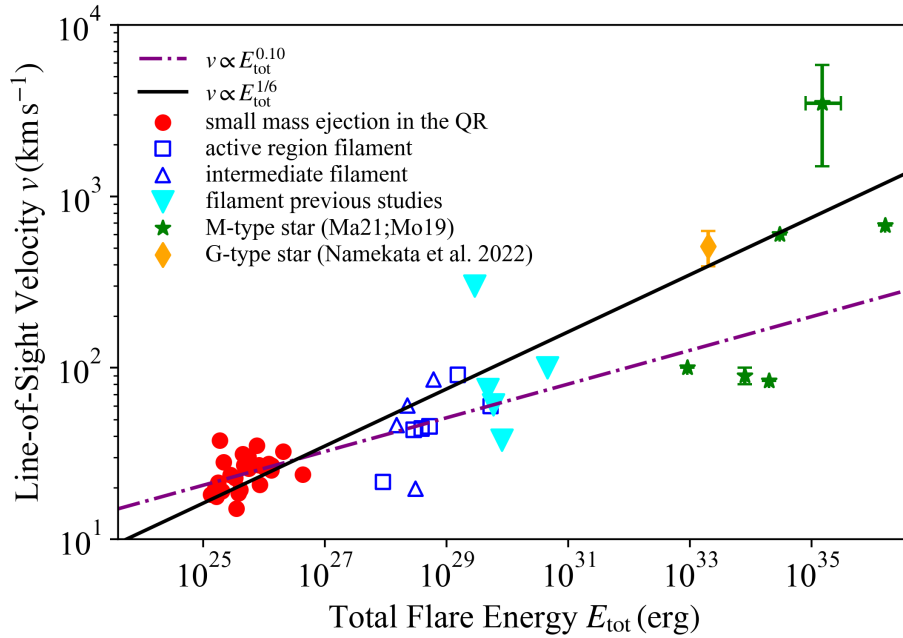aller to about 10% for large filament eruptions. The correlation coefficient of all events analyzed in this study is $r = 0.87$ and its 95% confidence intervals is $0.76 < r < 0.94$. The linear fitting between the logarithm of E_{kin} and E_{tot} results $E_{\mathrm{kin}} \propto E_{\mathrm{tot}}^{0.68 \pm 0.12}$. Here, the uncertainty of the power index is estimated by assuming an error of an order of magnitude in the kinetic energy. This power-law index is smaller than the power ($= 1.05$) between the flare X-ray fluence and the CME kinetic energy reported by Drake et al. (2013). Figure 3.7 also includes the previous result of the filament eruption and stellar events. We can see from this figure that the results of the M-type stars roughly coincide to the extension of the fitting results of the events analyzed in this study. The correlation coefficient r_{previous} increases to $r_{\mathrm{previous}} = 0.96$ and its 95% confidence intervals is $0.92 < r_{\mathrm{previous}} < 0.98$.

Figure 3.8 shows the relationship between total flare energy and line-of-sight velocity analyzed in this study. The correlation coefficient of all events analyzed in this study is $r = 0.73$ and its 95% confidence intervals is $0.52 < r < 0.85$. Linear fitting of logarithms of these quantities results in $v \propto E_{\mathrm{tot}}^{0.10 \pm 0.04}$, where the uncertainty is given for an error of factor two in the velocity. Takahashi et al. (2016) derived $v \propto E_{\mathrm{tot}}^{1/6}$ for CMEs by assuming $E_{\mathrm{kin}} \propto E_{\mathrm{tot}}$ and $M \propto E_{\mathrm{tot}}^{2/3}$. Since the filament eruptions in Figure 3.7 are roughly consistent with the $E_{\mathrm{kin}} = 0.1 E_{\mathrm{tot}}$ relation, we also show the $v \propto E_{\mathrm{tot}}^{1/6}$ relation in the figure. Figure 3.8 also includes the comparison with previous results. The correlation coefficient r_{previous} increases to $r_{\mathrm{previous}} = 0.86$ and its 95% confidence intervals is $0.76 < r_{\mathrm{previous}} < 0.92$. Although the dependence on flare energy is small, we can confirm a positive correlation between velocity and total flare energy from this figure. We can also confirm that the $v \propto E_{\mathrm{tot}}^{1/6}$ relationship roughly corresponds to the upper limit of the velocity.

3.4 Discussion and conclusion

3.4.1 Mass-total flare energy relation

To explain the relationship between the mass of the cold plasma ejections and the total flare energy, we attempt to derive a scaling law using a simple model. We assume that the filament is approximated by a cuboid supported by a stable helical magnetic field shown in Figures 3.9a and 3.9b. In this situation, the characteristic spatial scale of the filament width l is proportional to the scale height due to gravitational stratification along the concave magnetic field. On the other hand, filament length L and height R are considered to vary similarly with the spatial scale. Hence, we can infer $M = \alpha L^2$ ($\alpha = $ const in
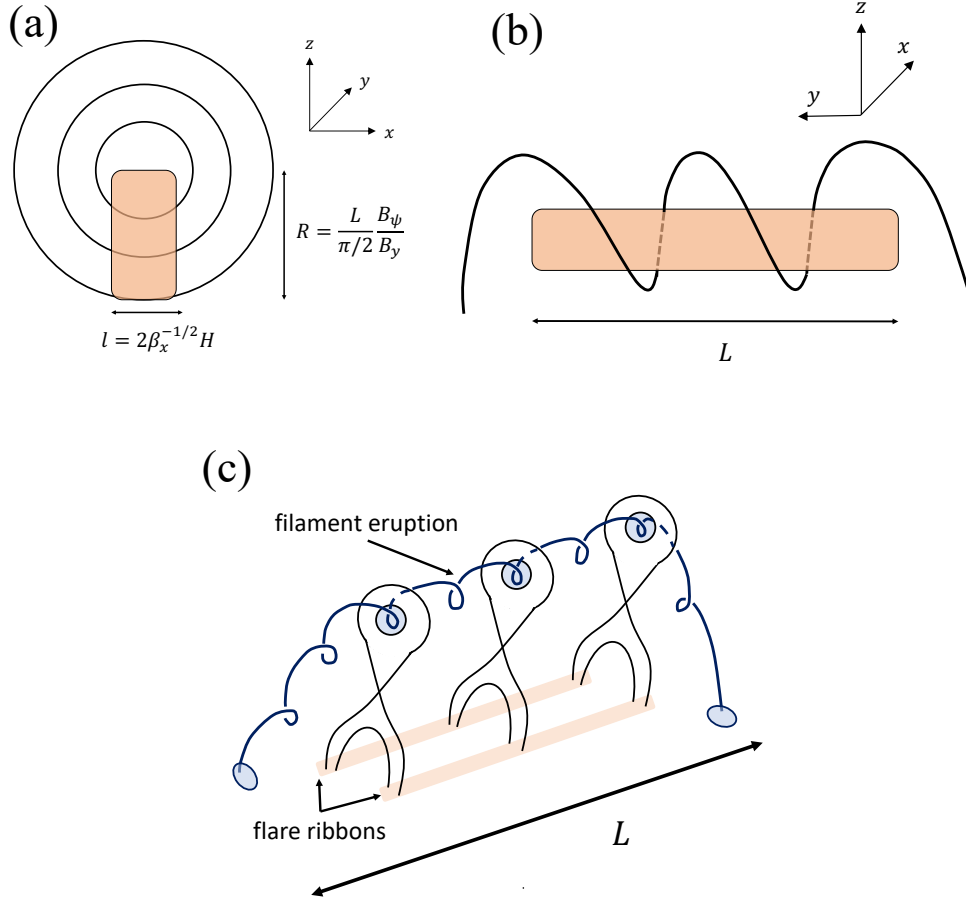
Figure 3.9: (a), (b) Geometric configuration of stably existing filaments. For the filament height R, we show equation (A.2) assuming $a = 4$. (c) Relationship between the erupting filament and the flare.

units of $\mathrm{g\,cm^{-2}}$). Since we determined both mass and length of the cold ejecta from our observation (Figures 3.4 and 3.6), we can determine the coefficient α by fitting of the data analyzed in this study. We show the relation between filament length and mass in Figure 3.10, and the fitting result is $\alpha = 10^{-5.12 \pm 0.079}$. Note that if the fitting is performed without assuming the $M \propto L^2$ relation, we obtain $M \propto L^{1.59 \pm 0.18}$. We also assume that a stable filament erupts with a flare, as shown in Figure 3.9c. In this case, the total flare energy can be estimated by the total amount of magnetic energy contained in a cube of length L. Hence, using the conversion rate f from the magnetic energy, the total flare energy can be roughly expressed as follows:

$$E_{\mathrm{tot}} = f \frac{B_{\mathrm{corona}}^2}{8\pi} L^3, \tag{3.11}$$
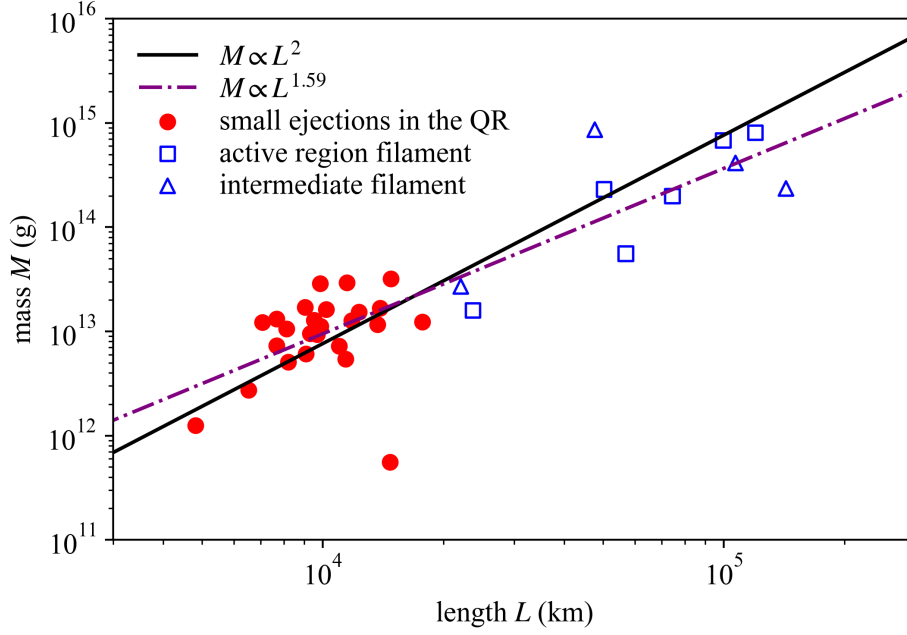
Figure 3.10: The relation between filament length and mass. The red circles, blue squares, and blue triangles represent small mass ejections in the quiet region, the active region filament, and the intermediate filament eruptions, respectively. The solid black line show the fitting result assuming $M \propto L^2$. The dash-dotted purple line shows the fitting of all events in Figure 3.10 without fixing the power-law index .

where B_{corona} is the strength of the coronal magnetic field surrounding the filament. Using $M = 10^{-5.12}L^2$, we can derive the scaling law as follows;

$$M = 8.8 \times 10^{12} \left(\frac{f}{0.1} \right)^{-2/3} \left(\frac{B_{\mathrm{corona}}}{50\,\mathrm{G}} \right)^{-4/3} \left(\frac{E_{\mathrm{tot}}}{10^{28}\,\mathrm{erg}} \right)^{2/3}. \tag{3.12}$$

We show the scaling law (3.12) for the cases $B_{\mathrm{corona}} = 5\,\mathrm{G}$ and $B_{\mathrm{corona}} = 50\,\mathrm{G}$ in Figure 3.6b. We confirm from Figure 3.6b that the scaling law explains well the present observation and also stellar events. This result implies that cold plasma ejections with flares occur by a common mechanism regardless of their scale, and supports the interpretation of blue shifts associated with stellar flares as stellar filament eruptions (Namekata et al., 2022b). We can also understand from the scaling law that the power on the total energy becomes smaller if we include large flares, as shown in Figure 3.6a; the reason could be the difference of the coronal magnetic field strength in quiet and active regions.

We point out the similarity between the scaling law of cold plasma ejection and that of CMEs. Takahashi et al. (2016) assume a cube of spatial scale L_{corona} corresponding to the characteristic length of the active region in the gravitationally stratified corona, and its mass is supposed to be the CME mass (M_{CME}). Therefore, the CME mass can

be estimated as $M_{\mathrm{CME}} \sim \rho_{\mathrm{corona}} L_{\mathrm{corona}}^2 H_{\mathrm{corona}} \propto L_{\mathrm{corona}}^2$, where ρ_{corona} is the mass density at the bottom of the corona and H_{corona} is the scale height in the corona. As a result, the mass is proportional to the 2/3 power of the total flare energy, similar to that in the cold plasma ejection case. Although the shape of the ejected plasma is different in these theories, the scaling laws of cold plasma ejections and CMEs both follow 2/3 power. This is because we can assume that, even for the hot plasma, the density scale height is smaller than the typical length of coronal magnetic field lines.

Next, we attempt to derive a scaling law by estimating the filament width and height to understand what physical quantity affects the coefficient α of the relation $M \propto L^2$. Based on the calculations in appendix A.1, we derive the following scaling law.

$$
\begin{aligned}
M = \quad & 9.0 \times 10^{12} \left(\frac{f}{0.1}\right)^{-2/3} \left(\frac{B_\psi/B_y}{0.3}\right) \left(\frac{\beta_x(x=0)}{10^{-3}}\right)^{-1/2} \\
& \left(\frac{H}{250\,\mathrm{km}}\right) \left(\frac{\rho}{3 \times 10^{-14}\,\mathrm{g\,cm^{-3}}}\right) \left(\frac{B_{\mathrm{corona}}}{50\,\mathrm{G}}\right)^{-4/3} \left(\frac{E_{\mathrm{tot}}}{10^{28}\,\mathrm{erg}}\right)^{2/3}, \quad (3.13)
\end{aligned}
$$

where B_ψ is an azimuthal component of the helical magnetic field and $\beta_x(x = 0)$ is the plasma β (the ratio of gas pressure to magnetic pressure) calculated from only the horizontal magnetic field B_x in the filament center. H and ρ are the filament's scale height and mass density. In deriving the above scaling law, we can express the coefficient α as in equation (A.9). Substituting the same values as in equation (3.13) into equation (A.9), the coefficient α can be expressed as follows.

$$
\alpha = 9.1 \times 10^{-6} \left(\frac{B_\psi/B_y}{0.3}\right) \left(\frac{\beta_x(x=0)}{10^{-3}}\right)^{-1/2} \left(\frac{H}{250\,\mathrm{km}}\right) \left(\frac{\rho}{3 \times 10^{-14}\,\mathrm{g\,cm^{-3}}}\right) \quad (3.14)
$$

The value of α determined by the parameter given in equation (3.14) is consistent with the value determined by fitting from the observed data ($= 10^{-5.12}$).

For M-type stars, some parameter values of the scaling law, such as B_{corona}, H, and ρ, should be different from those of denominators in equation (3.13) because the dipolar magnetic field is expected to be 10–1000 times stronger than that of Sun-like stars (See et al., 2017) and the gravitational acceleration g and surface temperature are also different on these stars. These differences may affect roughly one order of magnitude on the scaling law and may explain the much smaller ejected mass in some events. Regarding the magnetic field strength, we need the coronal magnetic field strength, not the photospheric magnetic field strength, to use our scaling law. Thus, the value of the magnetic field in M-type stars used in our scaling law should be several times smaller than the dipole field values (typically 200 G, up to 2000 G) summarized in See et al. (2017). Assuming that the coronal magnetic field is three times smaller than the photospheric field, we obtain about 60-600 G as the coronal magnetic field of an M-type star. These coronal field values can explain why the ejected mass of some events appear as extensions of the solar case while

some are about an order of magnitude smaller in Figure 3.6b. This estimate is also roughly consistent with the M-type star's coronal magnetic field strength estimated by the scaling law between flare duration and flare energy (Namekata et al., 2017b; Maehara et al., 2021) and the scaling law between flare temperature and flare emission measure (Shibata & Yokoyama, 1999, 2002; Raassen et al., 2007). Meanwhile, according to Sakaue & Shibata (2021), $\rho H = p/g$ in the transition region changes only a factor of three approximately between the Sun and M-type stars. The calculation of Sakaue & Shibata (2021) was for an open flux tube with a different geometry from a closed loop. However, assuming the same trend in the closed loop and that the gas pressure in the filament and the transition region is comparable, the difference in ρH on the scaling law is expected to be a factor of three approximately. From these discussions, we expect that equation (3.13) (and equation (3.12)) are also applicable to M-type stars by accounting for differences in the coronal magnetic field strength.

3.4.2 Kinetic energy, velocity, and total flare energy relation

Here, we discuss the theoretical relationship among kinetic energy, velocity, and total flare energy spanning more than ten orders of magnitude, as shown in Figures 3.7 and 3.8. For this purpose, we consider the relations for solar CMEs ($E_{\mathrm{kin}} \propto E_{\mathrm{tot}}$ and $v \propto E_{\mathrm{tot}}^{1/6}$), which Takahashi et al. (2016) reported being established for solar CMEs, and compare these relations with the present analysis for cold plasma ejections.

The relationship $v \propto E_{\mathrm{tot}}^{1/6}$ is roughly consistent with the upper limits of the velocity for each energy in Figure 3.8. Note that we used the "line-of-sight" velocity in this observation, which provides a lower bound of the velocity due to the projection effect. Hence, the theoretical $v \propto E_{\mathrm{tot}}^{1/6}$ relationship can appear only for the upper limits for each total flare energy in Figure 3.8. The relationship $v \propto E_{\mathrm{tot}}^{1/6}$ may correspond to a larger Alfvén velocity as the spatial scale increases. In other words, it would indicate that as the spatial scale increases, the height of the ejecta increases, and the plasma density decreases.

Figure 3.7 shows that $E_{\mathrm{kin}} = 0.1 E_{\mathrm{tot}}$ is a good approximation for the relation between the total flare energies and the kinetic energy of the cold plasma ejections in a range of $E_{\mathrm{tot}} \sim 10^{27} - 10^{29}\,\mathrm{erg}$. However, the power obtained by our observation ($E_{\mathrm{kin}} \propto E_{\mathrm{tot}}^{0.68}$ in Figure 3.7) is less than one for a wider range of energies. For small events in the quiet region, the ratio of kinetic energy to total energy is greater than 10%, and for some stellar cold plasma ejections, the ratio is significantly smaller than 10%. Therefore, it is inconsistent with our observation for a wide energy range, although the $E_{\mathrm{kin}} = 0.1 E_{\mathrm{tot}}$ relationship is consistent with the relationships $M \propto E_{\mathrm{tot}}^{2/3}$ and $v \propto E_{\mathrm{tot}}^{1/6}$.

Are there any problems with our analysis method that prevented $E_{\mathrm{kin}} = 0.1 E_{\mathrm{tot}}$ from being valid for a wide range of energies? For small events in the quiet region, neglecting

non-thermal energy may cause the underestimation of the total flare energy. In addition, recent studies have suggested that only a portion of the loops are brightened in EUV seen in coronal temperature in small flares in the quiet region (Berghmans et al., 2021; Chen et al., 2021). In other words, even if magnetic reconnection occurs, the major part of the loop may remain at the chromospheric temperature. Since the thermal energy is obtained from the EUV in our observation, we cannot measure the thermal energy of the plasma at chromospheric temperature, which may lead to an underestimation of the total flare energy.

The smaller kinetic energies obtained for some stellar events than that expected from the $E_{\mathrm{kin}} = 0.1 E_{\mathrm{tot}}$ relation may reflect the unique nature of stellar ejections. Some numerical studies for stellar CMEs have reported the possibility of the stellar CMEs suppression by a large-scale stellar coronal magnetic field (Alvarado-Gómez et al., 2018; Sun et al., 2022). In addition, the spatial scale of the stellar ejection is comparable to the stellar radius, and its spectra may be more sensitive to the projection effect than in solar cases. Consequently, the line-of-sight velocity and the kinetic energy are more likely to be underestimated in the stellar cases than in the solar cases. To understand the significance of this effect, we need further sun-as-a-star analyses for the spectra of the cold plasma ejection (Namekata et al., 2022b; Otsu et al., 2022).

3.4.3 Error sources and validity of event selection methods

We note that our estimation of the physical quantities has errors of approximately one order of magnitude. When estimating ejection mass, there are uncertainties in the line-of-sight thickness of ejecta and the validity of selecting the time and pixels at which the mass was estimated. We have analyzed the same event as Namekata et al. (2022b) and have confirmed that our mass estimation is about factor 2 smaller than their result due to the selection of the time and pixels (Figure 3.6b). Uncertainties also arise from the model used to estimate the mass (Tsiropoula & Schmieder, 1997). Thus, the ejection mass is expected to have an error of approximately one order of magnitude. In estimating the energy of small flares in the quiet region, we used their thermal energy based on Warmuth & Mann (2020). Flare energies accompanied by filament eruption were estimated by assuming that the bolometric energy is proportional to the GOES flare class. However, the flare energy partition has not been concretely established, and some studies have suggested that the power between bolometric energy and GOES flare class has different values (see Cliver et al., 2022, Fig. 22). In addition, the estimated kinetic energy is supposed to be a lower bound. This underestimation is due to our measurement of only line-of-sight velocity and neglecting the kinetic energy of the hot coronal plasma. For determining the flare energy in the M-type stars, the bolometric energy was estimated from the X-ray energy, which was estimated from the Hα line energy. Therefore, the energy uncertainty is considered more significant than the solar cases.

We note that transverse motions of plasma during the wavelength scan will not affect the results of our analysis. SDDI can take 73 images from H$\alpha - 9.0$ Å to H$\alpha + 9.0$ Å in ten seconds (Ichimoto et al., 2017). Hence, the time difference in observing from H$\alpha - 2.0$ Å to H$\alpha + 2.0$ Å is approximately 2 s. Since the typical line-of-sight velocity of the plasma analyzed in this study is $30\,\mathrm{km\,s^{-1}}$ (Figure 3.8), the plasma moves horizontally by approximately $(2\,\mathrm{s} \times 30\,\mathrm{km\,s^{-1}})/(1.23\,\mathrm{arcsec} = 8.99 \times 10^2\,\mathrm{km}) = 1/15$ of the SDDI pixel size during a single scan in the wavelength direction. Moreover, we performed spatial averaging in deriving the physical quantities in this study. Based on the above discussions, the effect of observing different plasmas with the same pixel would be minor in this study.

Our analysis results are expected to contain errors of approximately one order of magnitude; however, the relationships between physical quantities over a wide range of total flare energies do not vary significantly. In the fitting results by the linear regression method in this study, the errors in power index were estimated to be about 0.1 in all cases ($M \propto E_{\mathrm{tot}}^{0.46\pm0.06}$, $E_{\mathrm{kin}} \propto E_{\mathrm{tot}}^{0.68\pm0.12}$, and $v \propto E_{\mathrm{tot}}^{0.10\pm0.04}$). Consequently, the physical quantity predicted from our fitting results are approximately one order of uncertainty for ten orders of magnitude variation in total flare energy. On the other hand, our linear regression method did not account for errors in the values of the x-axis, that is, the total flare energy. We also estimated the power indexes and their errors by the orthogonal distance regression (ODR) method to consider the error in both and x- and y-axes. As a result of the fitting with an error of one order of magnitude in the total flare energy, we obtained $M \propto E_{\mathrm{tot}}^{0.54\pm0.05}$, $E_{\mathrm{kin}} \propto E_{\mathrm{tot}}^{0.75\pm0.07}$, and $v \propto E_{\mathrm{tot}}^{0.11\pm0.02}$. These results were almost similar to those obtained using linear regression methods. We also fitted using the ODR method for the relationship between the cold plasma's length and mass, assuming a factor two error in the length. We obtained $M = 10^{-5.12\pm0.07}L^2$ and $M \propto L^{1.9\pm0.18}$, and these results were similar to those by linear regression methods. Note that we assumed symmetric errors for the fittings in this study. However, some of our physical quantities estimation errors only act in one direction: asymmetric errors (such as underestimation of kinetic energy and neglection of non-thermal energy for small flares in the quiet region). Therefore, while our analysis leaves open the issue of handling asymmetric errors, it is believed to reflect the correct trend as long as the errors are symmetric.

Our analysis excluded events that have only cold plasma ejections or only flare brightening. Because of this, we can perform comparisons with the stellar cases. If we include events in which only cold plasma ejections occur, it is formally possible to add them in Figures 3.6 through 3.8 by setting the flare thermal energy or bolometric energy to the detection limit in our method. Because kinetic energy accounts for a large proportion of the total flare energy in small events in the quiet region, those events will be similar to our analysis results. In contrast, for large filament eruptions, the flare energy would shift toward an order of magnitude or two smaller. Events with only flares cannot be added

to Figures 3.6 through 3.8 because the physical quantities of the cold plasma ejecta are not present. Some flares are accompanied by hot plasma eruptions at coronal temperature (plasmoid ejections) seen in soft X-ray or EUV without cold plasma ejections (e.g., Ohyama & Shibata, 1998; Takasao et al., 2012). In this sense, the correlations and scaling laws for mass and kinetic energy of cold ejecta investigated in this study would correspond to an upper limit on the low-temperature component in eruptive events. Ohyama & Shibata (1998) reported the mass of the hot plasmoid and its kinetic energy (mass: $(2.3 \pm 0.2) \times 10^{13}$ g, kinetic energy: $8 \times 10^{27} - 2 \times 10^{28}$ erg) close to those obtained in this study for an M2.0 class flare. Those hot ejections are desired to be included to establish a complete scenario on the relationship between flares and plasma ejections.

In this study, we estimated physical parameters of various scale solar cold plasma ejection accompanied by flares. We showed their positive correlations and constructed a theoretical scaling law between the total flare energy and the ejected mass. Our scaling law suggests a common physical mechanism across a wide range of energies and can also be used to estimate parameters such as magnetic fields indirectly. In particular, we expect to make more progress in parameter estimation for stellar flare observations when combined with other scaling laws (Shibata & Yokoyama, 1999, 2002; Namekata et al., 2017b). We expect that our results will serve as a quantitative benchmark for studies of stellar flares (Namekata et al., 2022b) and "campfires" associated with cold plasma ejection (Panesar et al., 2021).

Numerical Simulation of Solar Photospheric Jet-like Phenomena Caused by Magnetic Reconnection

4.1 Introduction

[†] In the solar atmosphere, different kinds of jet phenomena, that is, the ejection of collimated plasma, can be observed at different wavelengths. In particular, numerous jets with a bright loop at their footpoint can be observed. These jets are called inverted-Y, Eiffel tower-shaped, or anemone jets because of their appearance (e.g., Shibata et al., 1994, 2007; Nisticò et al., 2009). Herein, we use the term "anemone jets" to refer to these jets in this chapter.

Anemone jets were first discovered in the corona by the Yohkoh satellite (Shibata et al., 1992; Shimojo et al., 1996). Shibata (1999) proposed that these jets are formed as a consequence of magnetic reconnection similar to large-scale flares followed by coronal mass ejections. Today, numerous simulations have been performed in two-dimensional (2D) (Yokoyama & Shibata, 1996) and three-dimensional (3D) scenarios (Moreno-Insertis et al., 2008; Moreno-Insertis & Galsgaard, 2013; Török et al., 2009; Pariat et al., 2009, 2015, 2016; Archontis & Hood, 2013; Fang et al., 2014; Lee et al., 2015; Wyper et al., 2018) and their results support this theory.

Approximately ten years after the Yohkoh satellite discovery, small anemone jets were found in the chromosphere by observation with the Hinode satellite (Shibata et al., 2007; Nishizuka et al., 2008; Singh et al., 2011). Although the spatial scale and velocity of the

---

[†]This chapter is based on Kotani & Shibata (2020)

anemone jets differ significantly between the corona and chromosphere (see table 4.1), their observational features and numerical simulations (Nishizuka et al., 2008; Takasao et al., 2013) support the fact that chromospheric anemone jets are also explained by magnetic reconnection. In both coronal and chromospheric cases, the jets speed is approximately the Alfvén speed, and the lifetime normalized by the Alfvén time is approximately $10 - 100$. These properties are consistent with reconnection theory and suggest that anemone jets are induced by reconnection regardless of their spatial scale. This fact reflects the scale universality of magnetohydrodynamics (MHD).

From the MHD scale universality, it can be expected that anemone jets having physical values as indicted in table 4.1 occur in the solar photosphere. However, considering that the solar photosphere is not magnetically dominant (plasma beta $\beta \sim 1 - 10$), it is not apparent that jets can be created as a result of magnetic reconnection, as in the chromosphere and corona of $\beta \ll 1$. Pariat et al. (2016) performed 3D MHD simulation in an environment of $\beta \simeq 1$; however, this calculation did not include gravity, and hence it could possibly not apply to the dynamics in the photosphere. Moreover, owing to the lack of spatial resolution, observing jets with a size of approximately $100\,\mathrm{km}$ remains a challenge. Several cases of brightening with inverted-Y-shaped loops in the upper photosphere and the lower chromosphere have been reported (Yurchyshyn et al., 2011; Bharti et al., 2017; Chitta et al., 2017; Tian et al., 2018; Nelson et al., 2019); however, their length is approximately $1000\,\mathrm{km}$. The jet phenomenon of approximately $100\,\mathrm{km}$ has not yet been observed.

The presence of photospheric anemone jets could be valuable as a source of waves in the lower solar atmosphere. When a photospheric anemone jet is generated, the surrounding pressure and magnetic field fluctuate and MHD waves are generated. Because the solar atmosphere is stratified by gravity, these MHD waves propagate to the upper layer with growing amplitude and form shock waves, which could drive spicules and surges. Such a growth process of MHD waves is the same mechanism that drives spicules by p-mode leakage and slow mode MHD waves generated from nonlinear Alfvén waves (Suematsu et al., 1982; De Pontieu et al., 2004; Hollweg et al., 1982; Kudoh & Shibata, 1999; Wang & Yokoyama, 2020) or surges from Ellerman bombs (e.g., Yang et al., 2014). As a model to explain the spicule formation with the same mechanism as coronal jets, Sterling & Moore (2016) proposed that spicules are formed by the ejection of microfilament. However, if the microfilament ejected at Alfvén speed is not re-accelerated, the height that can be achieved is $\sim H/\beta$ (H: scale height$\sim 150\,\mathrm{km}$ in the solar photosphere). Therefore, it is difficult for the microfilament itself to achieve the height of the spicule even if the microfilament erupts from the photosphere or lower chromosphere with $\beta \sim 1$. Hence, even when considering microfilament ejection, it is necessary to consider the MHD waves generated by the ejection or the re-acceleration mechanism of the microfilament. Moreover, magnetic re-

Table 4.1: Typical physical quantities of anemone jets in each layer of the solar atmosphere.

Region	Length (km)	Velocity (km s^{-1})	Lifetime (s)	Alfvén velocity (km s^{-1})	t/t_A
Corona	$10^4 - 10^5$	$100 - 10^3$	$10^3 - 10^4$	$100 - 10^3$	$10 - 100$
Chromosphere	$10^3 - 10^4$	$10 - 100$	$100 - 10^3$	$10 - 100$	$10 - 50$
Photosphere?	$10 - 100$	$1 - 10$	$10 - 100$	$1 - 10$	$10?$
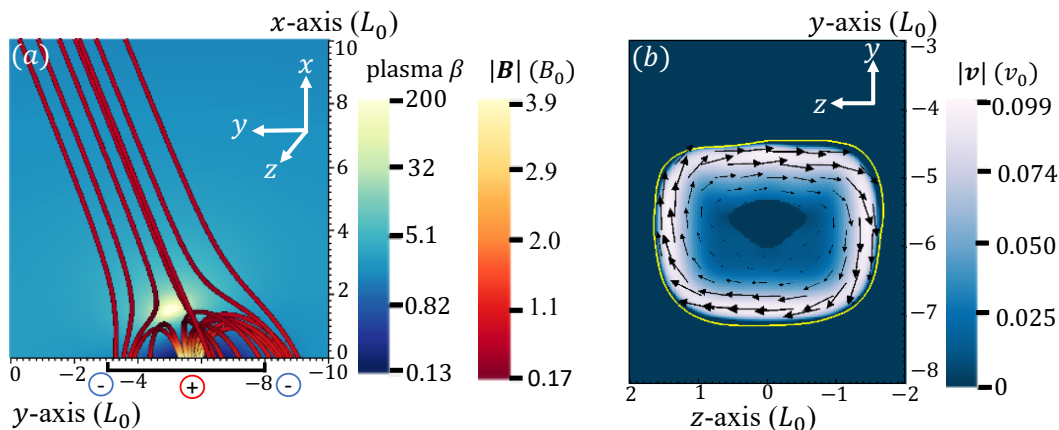
Figure 4.1: (a): Initial potential field and distribution of plasma β. The symbols in the bottom boundary mean the polarity of the magnetic field. The region indicated by the black line along the y-axis represents the range of the (b). (b): Velocity distribution in the bottom boundary at $t = 60t_0$. Yellow contour means polarity inversion line.

connection has been proposed as the origin of the waves necessary to cause chromospheric and coronal heating (e.g., Parker, 1991). If reconnection events in the lower atmosphere provide waves to heat, photospheric jets could be a candidate. For these reasons, we must study photospheric anemone jets to determine spicule models and clarify the heating mechanism of the solar atmosphere.

In this study, we perform a 3D MHD simulation of magnetic reconnection with solar photospheric parameters to investigate the properties of photospheric anemone jets. Then, we discuss the degree to which MHD waves are generated from the jets and how they influence the upper atmosphere.

4.2 Method

Although in the solar photosphere the temperature is $\sim 6000\,\text{K}$, ionization degree is low, and majority of components of the fluid are neutral, numerous collisions do occur between the neutral and plasma owing to the high density in the photosphere. The collision time between the ion and neutral τ represents $\nu_{in}^{-1} \simeq n_n \sqrt{(8k_B T/\pi m_{in})} \Sigma_{in}$, where ν_{in}, n_n,

$m_{in} = (m_i + m_n)/m_i m_n$, and $\Sigma_{in} \simeq 5 \times 10^{-15}\,\mathrm{cm}^2$ are the collisional frequency of ions with the neutrals, number density of the neutrals, reduced mass of the ion and neutral, and ion-neutral collision cross-sections (Leake & Arber, 2006). We assume that all the elements are hydrogen and $n_n = 10^{17}\,\mathrm{cm}^{-3}$ in the photosphere; then, m_{in} is the proton mass m_p and $\tau \simeq 10^{-9}\,\mathrm{s}$. This time is considerably shorter than the time resolution of our simulation $dt \sim 0.1 \times 0.1\,\mathrm{km}/(c_s = 8.15\,\mathrm{km\,s^{-1}}) \sim 10^{-3}\,\mathrm{s}$. Thus, we can neglect the effect of the partially ionized plasma in our simulation, and we adopt the one fluid (MHD) approximation.

For our numerical simulation, we use Athena++ code with the van Leer predictor-corrector scheme and Piecewise Linear Method (Stone et al., 2020). We solve the ideal MHD equations including uniform gravity and simple form radiative cooling (Newton cooling). The basic equations are as follows.

$$\frac{\partial \rho}{\partial t} + \boldsymbol{\nabla} \cdot (\rho \boldsymbol{v}) = 0 \tag{4.1}$$

$$\frac{\partial \rho \boldsymbol{v}}{\partial t} + \boldsymbol{\nabla} \cdot (\rho \boldsymbol{v} \boldsymbol{v}) = -\boldsymbol{\nabla} p + \frac{1}{4\pi}(\boldsymbol{\nabla} \times \boldsymbol{B}) \times \boldsymbol{B} + \rho \boldsymbol{g} \tag{4.2}$$

$$\frac{\partial (e + \frac{1}{2}\rho v^2 + \frac{B^2}{8\pi})}{\partial t} + \boldsymbol{\nabla} \cdot [(h + \frac{1}{2}\rho v^2 + \frac{B^2}{4\pi})\boldsymbol{v} - \frac{1}{4\pi}(\boldsymbol{B} \cdot \boldsymbol{v})\boldsymbol{B})]$$
$$= \rho \boldsymbol{g} \cdot \boldsymbol{v} - \frac{\rho R}{\mu(\gamma - 1)}\frac{T - T_0}{\tau_{\mathrm{cooling}}} \tag{4.3}$$

$$\frac{\partial \boldsymbol{B}}{\partial t} = \boldsymbol{\nabla} \times (\boldsymbol{v} \times \boldsymbol{B}) \tag{4.4}$$

$$p = \frac{\rho R T}{\mu} \tag{4.5}$$

, where e is the internal energy of the fluid, $h = p + e$ is the enthalpy, $T_0 = 6000\,\mathrm{K}$ is uniform initial temperature, $\tau_{\mathrm{cooling}} = 1\,\mathrm{s}$ is mean cooling time and $\mu = 1.25$ is mean molecular weight in the solar photosphere. Note that $\tau_{\mathrm{cooling}} = 1\,\mathrm{s}$ agrees with the cooling time deduced for the photosphere with temperature $T = 6000\,\mathrm{K}$ (Athay, 1976, p. 474 table X-4) and that it decreases with height in the actual sun. In our simulation, because magnetic reconnection occurs at a height of approximately $20\,\mathrm{km}$ and the majority of the temperature change occurs in this vicinity, we set the cooling time uniform within the simulation box for simplicity. $\boldsymbol{g}$ is the gravitational acceleration of the solar atmosphere ($|\boldsymbol{g}| = 2.7 \times 10^4\,\mathrm{cm\,s^{-2}}$) and we set $\boldsymbol{g} = (g_x, g_y, g_z) = (-g, 0, 0)$. We assume a specific heat ratio of $\gamma = 5/3$.

For the normalization of the simulation, we use the typical length $L_0 = 10\,\mathrm{km}$, initial temperature $T_0 = 6000\,\mathrm{K}$, and density in the bottom boundary $\rho_0 = 1.0 \times 10^{-7}\,\mathrm{g\,cm^{-3}}$. Then, we use the unit of velocity, pressure, magnetic field, and time as $v_0 = \sqrt{(RT_0/\mu)} = 6.32 \times 10^5\,\mathrm{cm\,s^{-1}}$, $p_0 = \rho_0 v_0^2 = 3.97 \times 10^4\,\mathrm{erg\,cm^{-3}}$, $B_0 = \sqrt{(4\pi p_0)} = 706\,\mathrm{G}$, and $t_0 = L_0/v_0 = 1.57\,\mathrm{s}$ (see table 4.2). Note that v_0 is different from the sound speed in the solar photosphere $c_{s0} = \sqrt{(\gamma R T_0/\mu)} = 8.15 \times 10^5\,\mathrm{cm\,s^{-1}}$.

Table 4.2: Units used in numerical simulation.

Length	Density	Temperature	Velocity	Gas pressure	Magnetic field	Time
L_0	ρ_0	T_0	v_0	p_0	B_0	t_0
$10\,\mathrm{km}$	$10^{-7}\,\mathrm{g\,cm^{-3}}$	$6000\,\mathrm{K}$	$6.32 \times 10^5\,\mathrm{cm\,s^{-1}}$	$3.97 \times 10^4\,\mathrm{erg\,cm^{-3}}$	$706\,\mathrm{G}$	$1.57\,\mathrm{s}$

Table 4.3: Parameters of magnetic field.

i	b_i	x_i	y_i	z_i
1	-1.35	-1.0	-0.5	-1.0
2	-1.35	-1.0	-0.5	-0.5
3	-1.35	-1.0	-0.5	0
4	-1.35	-1.0	-0.5	0.5
5	-1.35	-1.0	-0.5	1.0
6	-1.35	-1.0	0	-1.0
7	-1.35	-1.0	0	0
8	-1.35	-1.0	0	1.0
9	-1.17	-1.0	-1.5	-1.0
10	-1.17	-1.0	-1.5	-0.5
11	-1.17	-1.0	-1.5	0
12	-1.17	-1.0	-1.5	0.5
13	-1.17	-1.0	-1.5	1.0
14	-1.17	-1.0	-1.0	-1.0
15	-1.17	-1.0	-1.0	0
16	-1.17	-1.0	-1.0	1.0

As an initial condition, we assume hydrostatic equilibrium with uniform temperature T_0. Moreover, we present a potential field as follows (Wyper et al., 2018).

$$\boldsymbol{B} = (c_1 \cos \theta, c_1 \sin \theta, 0) + \sum_{i=1,16} \boldsymbol{\nabla} \times \boldsymbol{A}_i \tag{4.6}$$

$$\boldsymbol{A}_i = \frac{b_i x_i^3}{2[x_i'^2 + (y_i' - y_c)^2 + z_i'^2]^{3/2}} \times [-z_i' \boldsymbol{e}_y + (y_i' - y_c)\boldsymbol{e}_z] \tag{4.7}$$

$c_1 = -0.8$ and $\theta = -22^o$ are the parameters of the background field strength and angle, respectively. $x_i' = x - x_i, y_i' = y - y_i, z_i' = z - z_i$. We present the values of b_i, x_i, y_i, z_i in table 4.3. Figure 1 (a) displays this initial field.

We set the velocity field in the bottom boundary as follows (Pariat et al., 2009; Wyper

et al., 2018):

$$v_x = 0 \tag{4.8}$$

$$\boldsymbol{v}_\perp = f(t)\nu_0 g(B_x)\boldsymbol{e}_x \times \boldsymbol{\nabla}B_x \tag{4.9}$$

$$g(B_x) = k\frac{B_r - B_l}{B_x}\tanh\left(k\frac{B_x - B_l}{B_r - B_l}\right) \quad B_l \le B_x \le B_r \tag{4.10}$$

$$= 0 \quad \texttt{otherwise}. \tag{4.11}$$

We set $k = 4.0$, $\nu = 0.002$, $B_l = 0.15$, and $B_r = 3.6$. $f(t)$ is the time development of the bottom boundary photospheric motion, and we assume the following:

$$f(t) = t/t_1 \quad (t < t_1) \tag{4.12}$$

$$= 1 \quad (t_1 \le t < t_2) \tag{4.13}$$

$$= 1 - \frac{t - t_2}{t_1} \quad (t \le t_2) \tag{4.14}$$

, where $t_1 = 60t_0$ and $t_2 = 75t_0$. Note that although the adopted function is the same, the values of these parameters are different from those of the previous study, resulting in different values of the velocity field from those of the previous study. These values are based on the assumption that granulation satisfies the Kolmogorov law $\epsilon \sim v_\lambda^3/\lambda$. Specifically, the typical size of the granulation is $1000\,\mathrm{km}$ and the speed is $1\,\mathrm{km\,s^{-1}}$; then, the speed of the smaller vortex of approximately $10\,\mathrm{km}$ is determined from the Kolgomogorov law as follows:

$$v_{\lambda=10\,\mathrm{km}} \sim v_{\lambda=1000\,\mathrm{km}}\left(\frac{\lambda = 10\,\mathrm{km}}{\lambda = 1000\,\mathrm{km}}\right)^{1/3} \sim 0.25\,\mathrm{km\,s^{-1}}. \tag{4.15}$$

Moreover, the time scale of the $10\,\mathrm{km}$ scale small vortex is

$$t_{\lambda=10\,\mathrm{km}} \sim \frac{\lambda = 10\,\mathrm{km}}{v_{\lambda=10\,\mathrm{km}}} \sim 40\,\mathrm{s}. \tag{4.16}$$

These values are consistent with the velocity and lifetime used in our simulation within a factor three. Figure 1 (b) displays this boundary motion. For gas pressure and density, the initial values are maintained, and for the magnetic field, the gradient is set to zero. In the other boundary, we use an open boundary and set the gradient of the physical value as zero.

We set our simulation box as $[x_\mathrm{min}, x_\mathrm{max}] \times [y_\mathrm{min}, y_\mathrm{max}] \times [z_\mathrm{min}, z_\mathrm{max}] = [0, 50L_0] \times [-12.5L_0, 7.5L_0] \times [-5L_0, 5L_0]$. We set the grid size as $dx = dy = dz = 0.05$. Moreover, the lattice spacing is halved at $[0, 10L_0] \times [-12.5L_0, -2.5L_0] \times [-2.5L_0, 2.5L_0]$ to sufficiently resolve the anemone-type magnetic field.

4.3 Results

Figure 4.2 displays the time evolution of the density distribution on the $z = 0$ plane and magnetic field lines integrated in the plane. First, the initial magnetic fields are twisted to
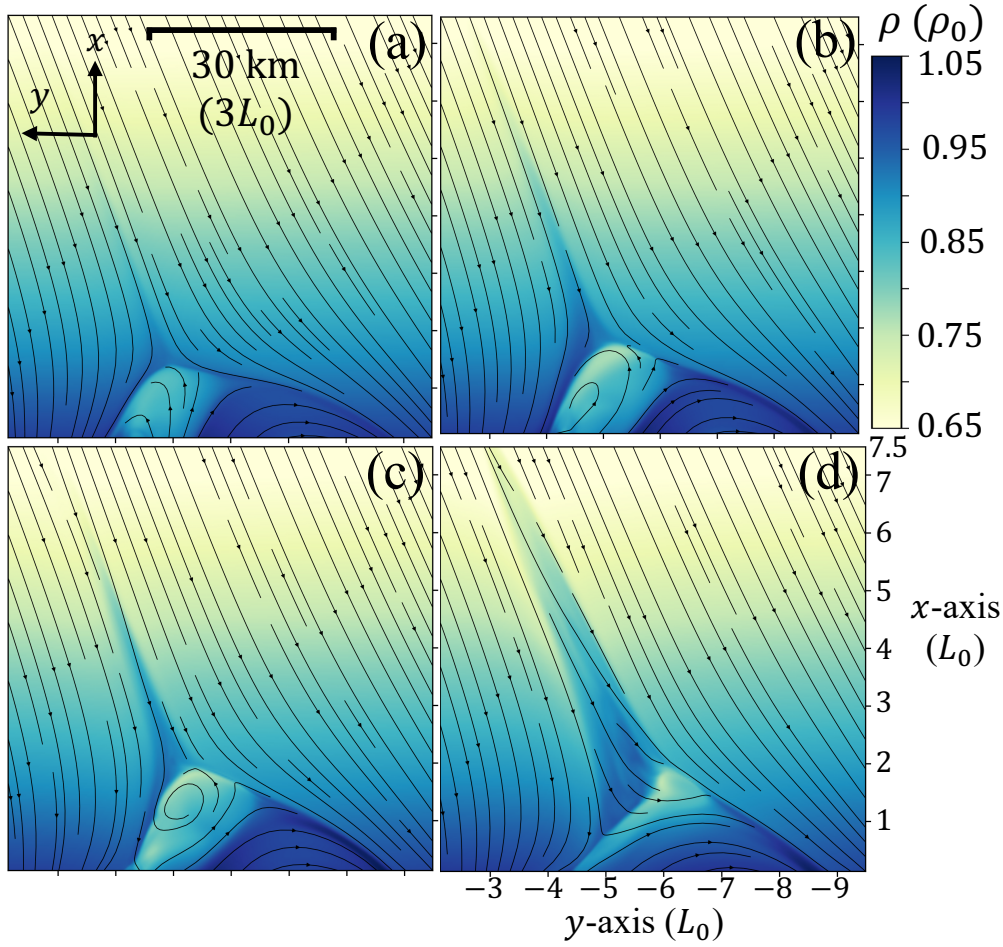
Figure 4.2: Time development of density distribution in $z = 0$ plane. (a): $t = 60t_0$, (b): $t = 70t_0$, (c): $t = 80t_0$, (d): $t = 100t_0$. Black lines display magnetic field lines integrated by x, y components in the plane. The upper boundary is the $x = 7.5L_0$ plane, where we measure the MHD wave energy fluxes in figures 4.14 and 4.17. (An animation of this figure is available.)

form a sheared loop because of the photospheric motion based on the boundary condition (figure 4.2a). As the magnetic pressure increases owing to the magnetic energy injected by the photospheric motion, the sheared loop rises (figure 4.2b). At this time, magnetic reconnection occurs at the top of the sheared loop, and a jet-like structure, which is an elongated density increase along the magnetic field lines and appears as a jet in imaging observations, is generated. This reconnection removes the magnetic field that holds the sheared loop from above and thus further promotes the rising of the sheared loop. When the twisted sheared loop emerges sufficiently, the twisted sheared loop and the background field cause magnetic reconnection, resulting in an untwisting jet-like structure, which releases numerous Alfvén waves (figures 4.2c and 4.2d). This mechanism is similar to coronal jet simulation (e.g., Pariat et al., 2009; Archontis & Hood, 2013; Wyper et al., 2018), which

assumes a corona of $\beta \ll 1$.

The length, apparent speed, and lifetime of this jet-like structure are approximately $100 \, \text{km}$, $5 \, \text{km} \, \text{s}^{-1}$, and $80 \, \text{s}$. This apparent speed approximately corresponds to Alfvén speed at this point. The length of the twisted sheared loop is approximately $30 \, \text{km}$, and hence the Alfvén time t_A is $t_A \sim 30 \, \text{km} / 5 \, \text{km} \, \text{s}^{-1} \sim 6 \, \text{s}$. Thus, the lifetime t divided by the Alfvén time t_A is $t/t_A \sim 80 \, \text{s} / 6 \, \text{s} \sim 13.3$. All of these values are consistent with those in table 4.1.

Figure 4.3 indicates how much the density and temperature increase in the jet-like structure. Figures 4.3a and 4.3b indicate that the jet-like structure has a density of approximately 1.1 times greater than its surroundings. Furthermore, figures 4.3c and 4.3d indicate that the temperature increases approximately 200 K in the jet-like structure, and that the temperature increase has an inverted-Y shape.

Figure 4.4 displays the 3D appearance at $t = 81t_0$. From figure 4.4b, we can observe that magnetic reconnection occurs between the twisted sheared loop and background fields, and plasma frozen in the reconnected field lines is accelerated approximately in the z-direction; that is, in the direction normal to the ambient field. Moreover, the twisted loop, background field, and current sheet are aligned in the z-direction. Therefore, the reconnection process can be investigated in more detail with an appropriate "$y = \text{const}$" cross section, though it is actually a complex 3D phenomenon.

Figures 4.5 and 4.6 display the physical values of the jet-like structure in the $y = -4.95L_0$ plane, where we can interpret the process of magnetic reconnection in a broadly 2D view. Closed fields at the bottom indicate the twisted sheared loop. From figure 4.5a, we can observe reconnection inflow and outflow. The outflow's velocity is $\sim 0.7v_0$, which corresponds to Alfvén velocity in the sheared loop (figure 4.5b). The inflow's velocity is $\sim 0.1v_0$. Then, we can estimate the reconnection rate $v_{\text{in}}/v_{\text{out}} \sim 0.1$. From figure 4.5c, we can observe that the maximum temperature in the current sheet is $\sim 6600\text{K}$ and the outflow temperature is $\sim 6300\text{K}$. From figure 4.5d, we can observe the area of $\text{div} v < 0$ between the inflow and outflow, which corresponds to the compression occurring. Moreover, the gas pressure becomes stronger and the magnetic field becomes weaker before and after the $\text{div} v < 0$ region (figures 4.6b and 4.6c), which indicates that the $\text{div} v < 0$ corresponds to a slow shock formed by magnetic reconnection. The slow shock and the reconnection rate in our simulation imply that this reconnection has similar properties to those of the Petschek model (Petschek, 1964).

From figures 4.5e–h, we can observe that the slow shock is displaced upward and the plasma is accelerated approximately in the z-direction in the upper atmosphere. This can certainly be confirmed by the one-dimensional (1D) distribution displayed in figure 4.7, which indicates both the upward and downward slow shocks formed by reconnection.
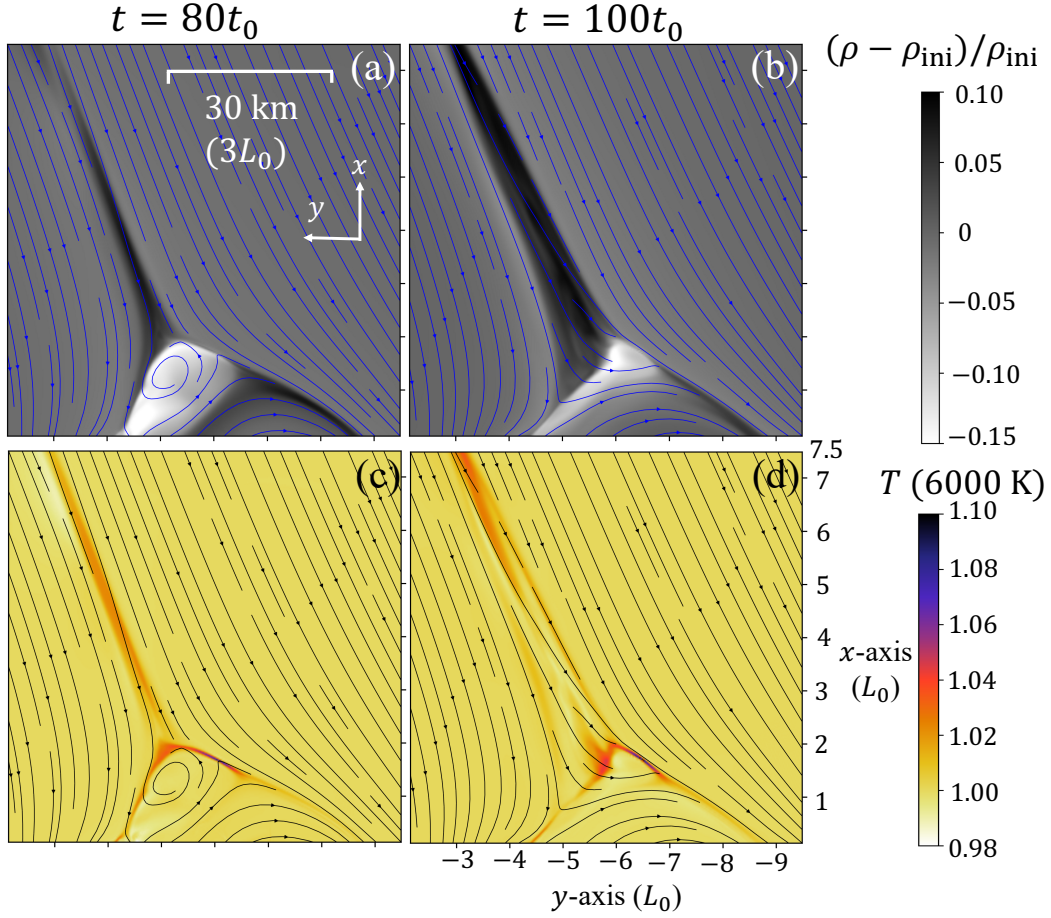
Figure 4.3: Rate of increase in density and temperature of the jet-like structure in $z = 0$ plane. The left and right columns indicate the same time as in figures 4.2c and 4.2d, respectively. ρ_{ini} is the initial density. The upper boundary is the $x = 7.5L_0$ plane, where we measure the MHD wave energy fluxes in figures 4.14 and 4.17.

Note that this displacement of the slow shock is not a result of the upward propagation of the slow shock in this plane. Figure 4.8 presents the time development of the $\mathrm{div}v < 0$ region and gas pressure in the $z = 0$ and $y = -4.95L_0$ planes. From this figure, we can observe that the region of $\mathrm{div}v < 0$ exists along the direction of the jet-like structure, that is, a uniform background magnetic field. Moreover, the strong $\mathrm{div}v < 0$ region extends from near the region where magnetic reconnection is occurring. These facts indicate that the $\mathrm{div}v < 0$ region is formed by the propagation of the slow shock produced in the process of magnetic reconnection along a uniform background field. Furthermore, from the figures 4.8a–c, we can observe that the sheared loop is displaced in the negative y-axis direction with time, and with it, the region of $\mathrm{div}v < 0$ is also displaced in the negative y-axis direction. It can be understood that the upward displacement of the slow shock in the $y = \mathrm{const}$ cross section observed in figures 4.5e-h corresponds to the negative y-axis
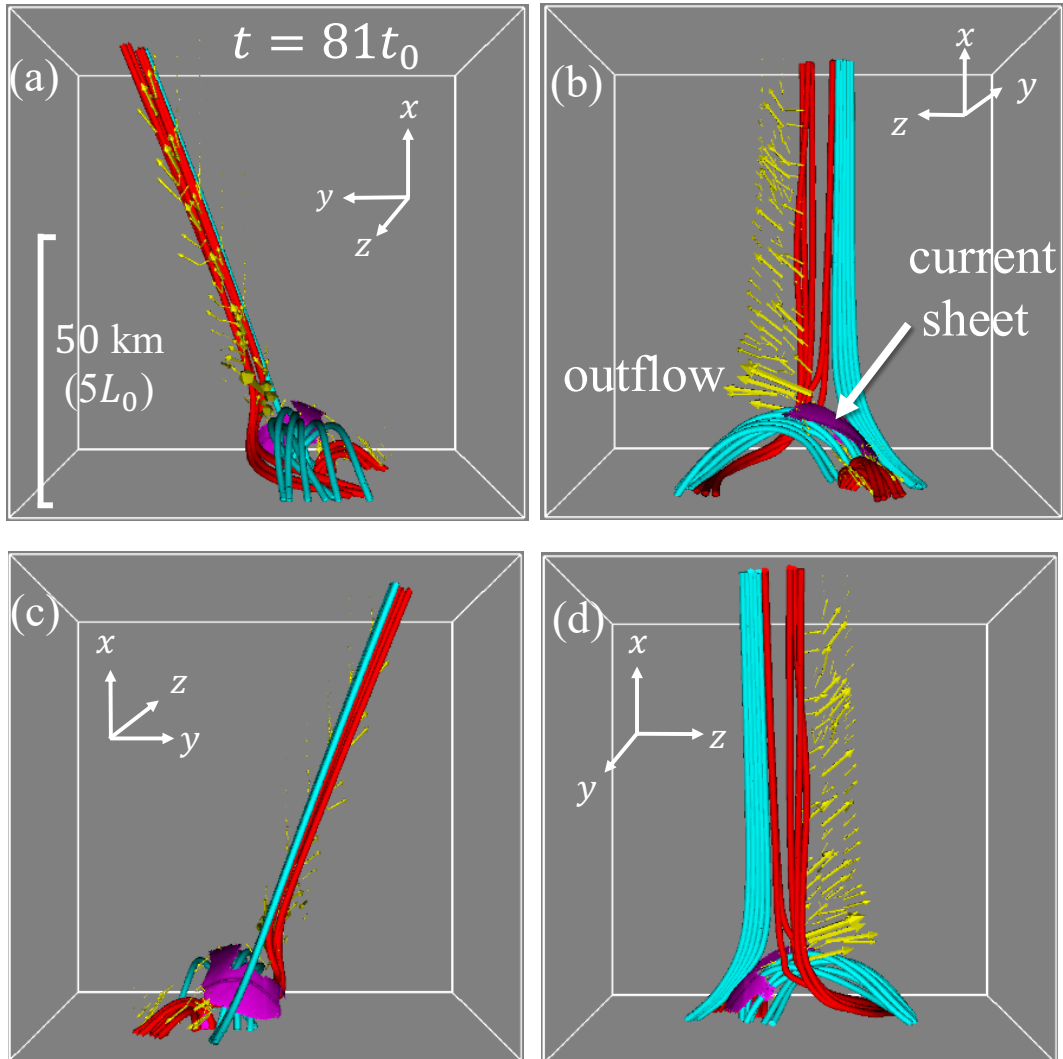
Figure 4.4: 3D view of the jet-like structure in $t = 81t_0$. Yellow arrows and pink surface are the velocity and current sheet. Light blue lines indicate twisted sheared loop and open fields before magnetic reconnection. Red lines indicate reconnected open fields and post-flare loop. The size of the largest arrow corresponds to $0.6v_0$.
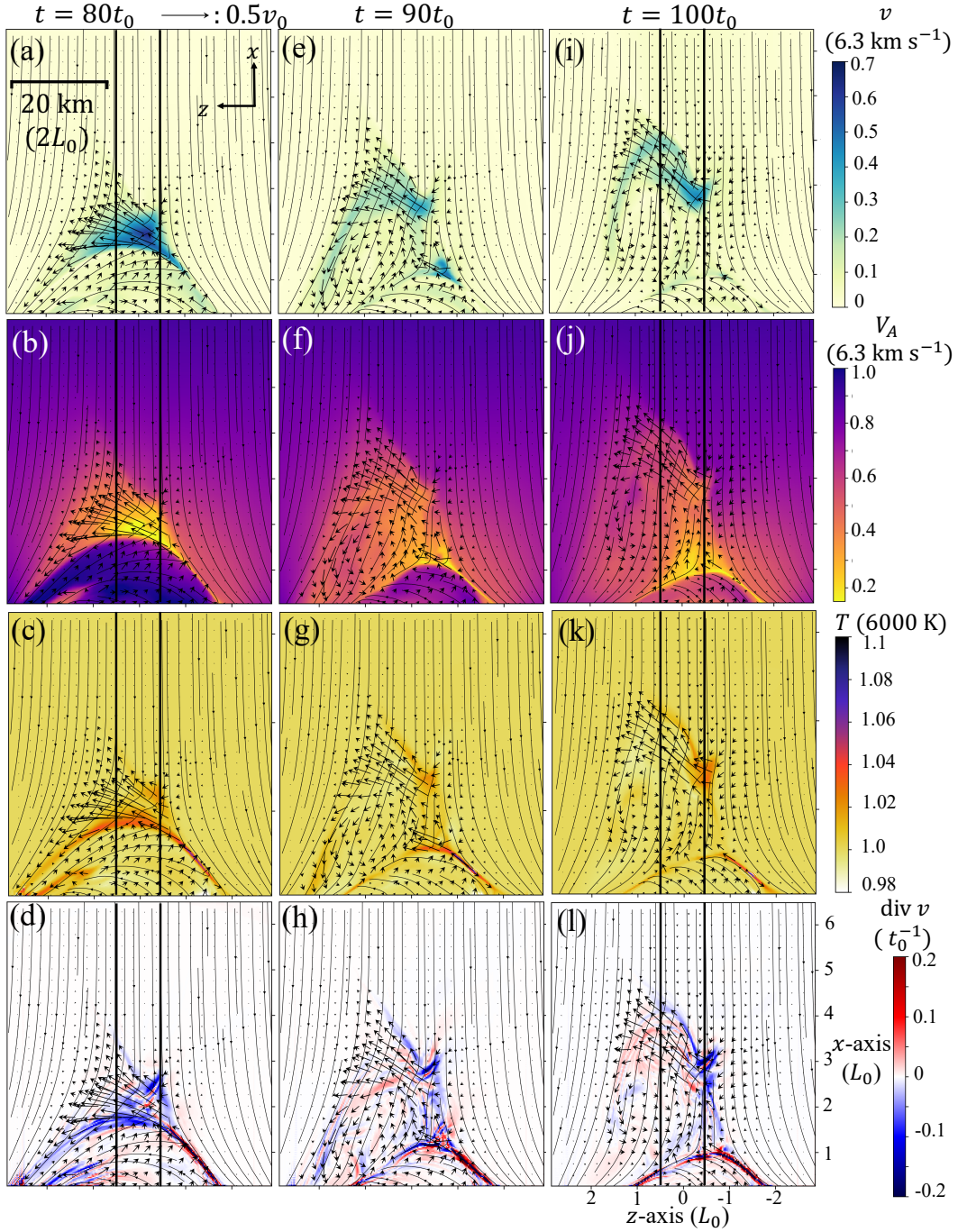
Figure 4.5: Physical values in $y = -4.985L_0$ plane at $t = 80t_0$ ((a)–(d)), $t = 90t_0$ ((e)–(h)), and $t = 100t_0$ ((i)–(l)). Each row shows velocity ((a), (e), and (i)), Alfvén velocity ((b), (f), and (j)), temperature ((c), (g), and (k)) and divergence of velocity ((d), (h), and (l)). Black arrows are velocity in the plane. Black lines show magnetic field lines integrated by x, z components in the plane. One dimensional distributions of some physical quantities along two black solid lines in $t = 80t_0$ and $100t_0$ are shown in figure 4.7.
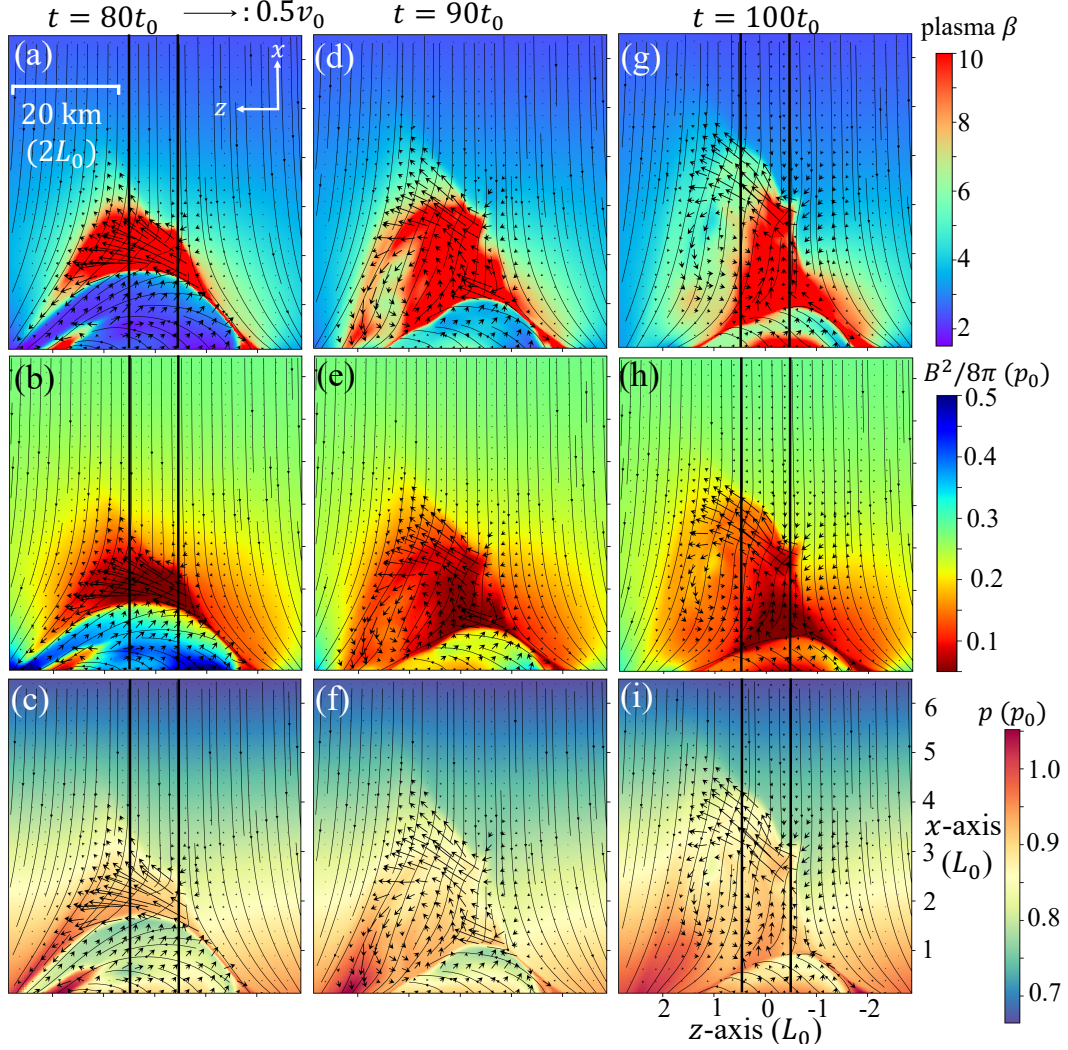
Figure 4.6: Physical values in $y = -4.985L_0$ plane at $t = 80t_0$ ((a)–(c)), $t = 90t_0$ ((d)–(f)), and $t = 100t_0$ ((g)–(i)). Each row shows plasma β ((a), (d), and (g)), magnetic pressure ((b), (e), and (h)), and gas pressure ((c), (f), and (i)). Black arrows are velocity in the plane. Black lines show magnetic field lines integrated by x, z components in the plane. One dimensional distributions of some physical quantities along two black solid lines in $t = 80t_0$ and $100t_0$ are shown in figure 4.7.
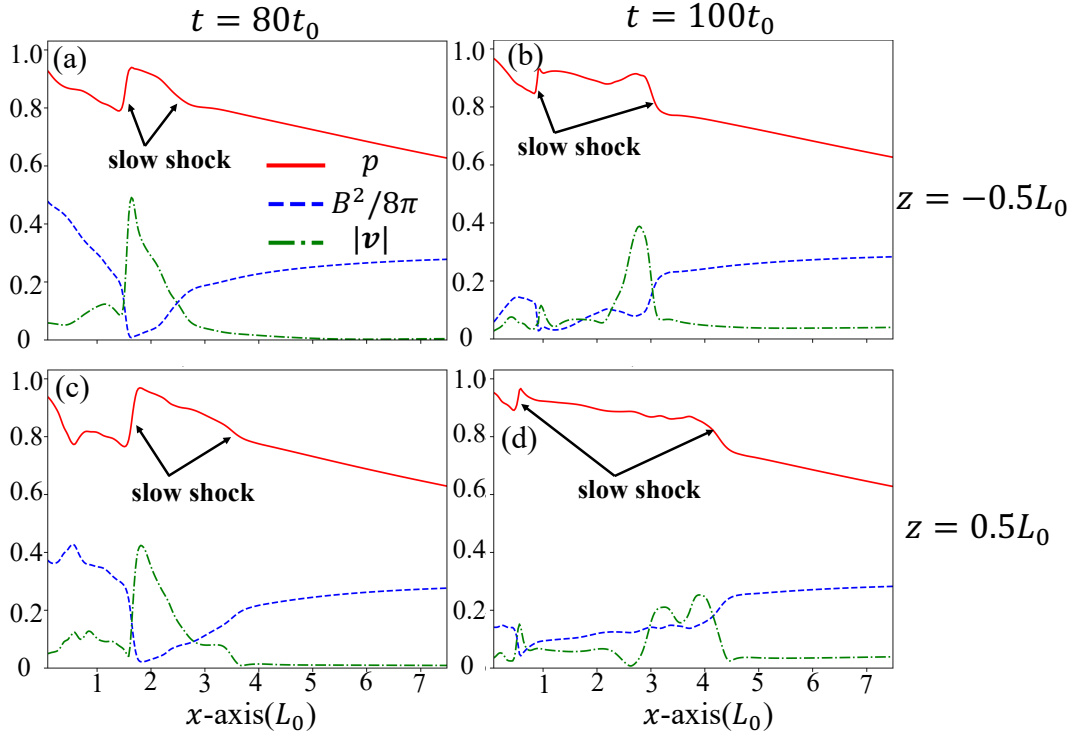
Figure 4.7: One-dimensional (1D) distribution of gas pressure, magnetic pressure, and velocity along the solid black lines at $z = 0.5$ and -0.5 shown in figures 4.5 and 4.6. The solid red lines indicate gas pressure, the dashed blue lines indicate magnetic pressure, and the dash-dot green lines indicate speed. The left column shows the distributions at $t = 80$, and the right column shows the distributions at $t = 100$. (a) and (b) correspond to distributions at z = -0.5, and (c) and (d) correspond to distributions at $z = 0.5$. The units are $3.97 \times 10^4 \, \mathrm{erg \, cm^{-3}}$ for gas and magnetic pressure and $6.32 \times 10^5 \, \mathrm{cm \, s^{-1}}$ for plasma speed.

displacement of the slow shock propagating through a uniform background magnetic field. In fact, the slow shock rising speed in figure 4.5 is less than $0.1v_0$, which corresponds to the sheared loop speed, namely the reconnection inflow.

4.4 Discussion

4.4.1 Formation mechanism of the jet-like structure

To determine the formation mechanism of the jet-like structure, we display in figure 4.9a, the Lagrangian trajectories of typical fluid particles on the same reconnected magnetic field line. For determining a reconnected field line, we select a point where the total force in the x-direction is greater than $0.1\rho_0 v_0^2 L_0^{-1}$ at $t = 82t_0$. Then, we select four points on the
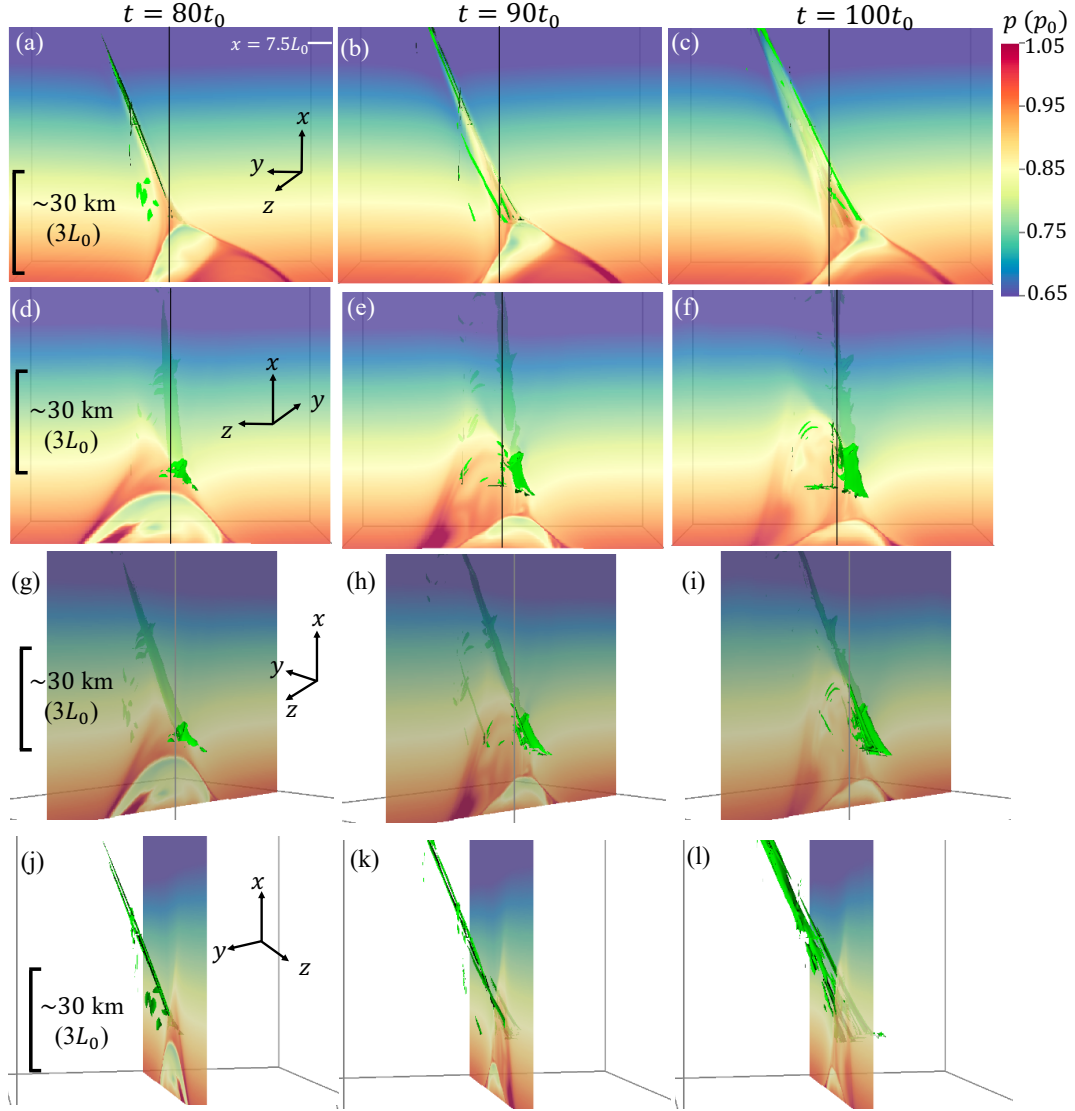
Figure 4.8: Time development of the $\mathrm{div}v < 0$ region and the gas pressure distribution shown in 2D planes. In each figure, the green surface indicates the regions of $\mathrm{div}v = -0.09t_0^{-1}$ and $-0.07t_0^{-1}$. (a)–(c): Gas pressure in the $z = 0$ plane. The solid black line shown in the center of each figure shows the $y = -4.95L_0$ plane. (d)–(f): Gas pressure in the $y = -4.95L_0$ plane. The solid black line shown in the center of each figure shows the $z = 0L_0$ plane. (g)–(i): Gas pressure in the $y = -4.95L_0$ plane and the 3D isosurfaces of $\mathrm{div}v$ from an oblique view.
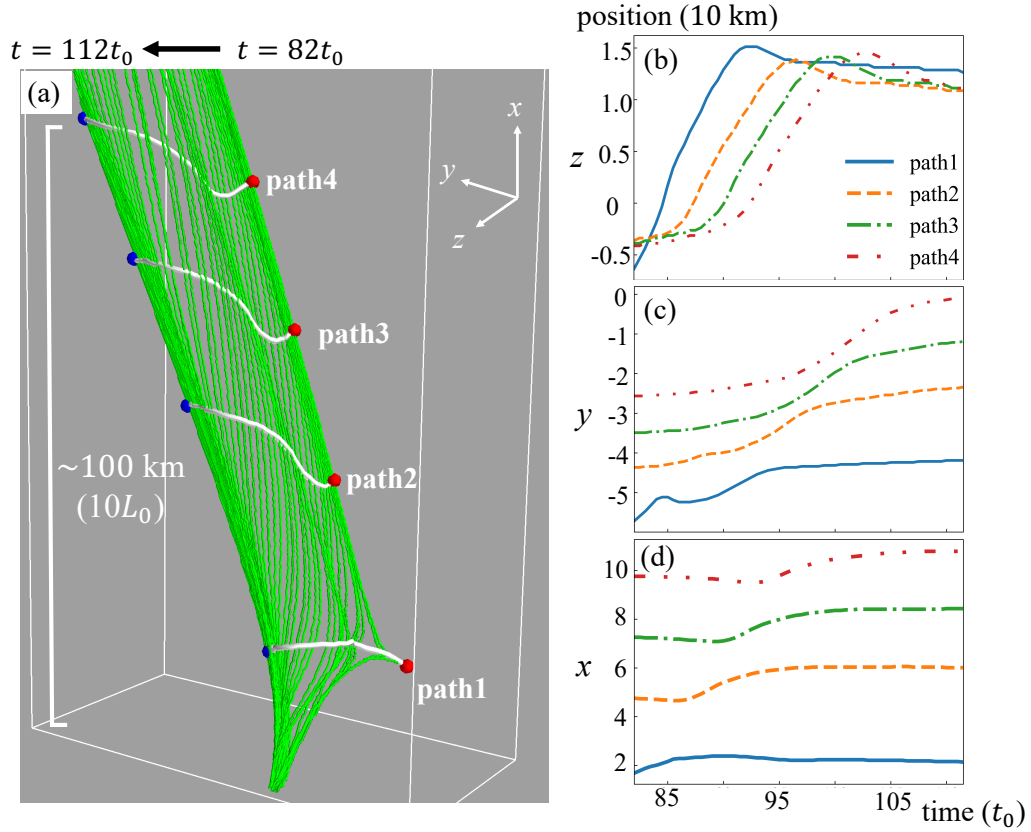
Figure 4.9: (a) 3D view of the paths traced by Lagrangian methods. Red and blue points show the start and endpoints of time development. White lines mean each path and green lines show magnetic field lines passing through path 2 at each time. (b)-(d) Time development of z, y, and x components of each path. The same type of lines indicates the same paths.

magnetic line passing through the point. We assume the time interval dt is $0.5t_0$. In figures 4.9b–d, we indicate the position (x, y, z) of those fluid particles on these as a function of time. From these figures, we can observe that the plasma rises; however, they do not move significantly when the magnetic tension attempts to straighten the reconnected field lines. In each path, the plasma particle is displaced only approximately $10\,\mathrm{km}$. This indicates that the jet-like structure of approximately $100\,\mathrm{km}$ observable in figures 4.2 and 4.3 is not formed by plasma motion; rather, it is formed by some wave propagation.

Figure 4.10 displays the time development of the gas pressure, magnetic pressure, and plasma speed along the trajectories indicated in figure 4.9. In figures 4.10b, 4.10c, and 4.10d, we can observe that gas pressure increases and the magnetic pressure decreases when the plasma speed increases rapidly. Furthermore, we can observe that this is the only time when the gas pressure increases in the time evolution of each path. From these facts, it can be understood that the gas compression is caused by the slow shock and the jet-like
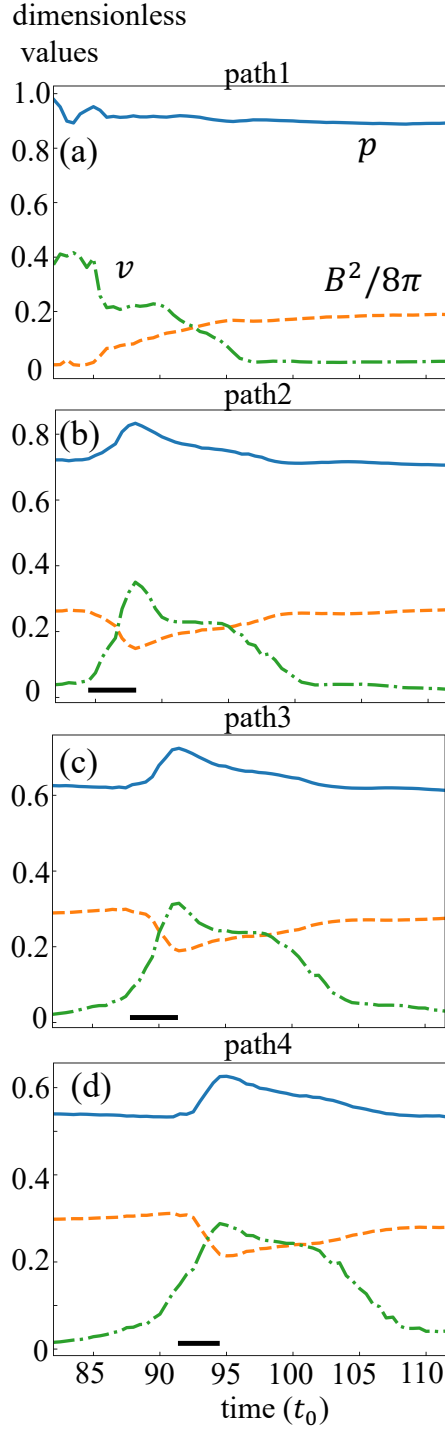
Figure 4.10: Time development of physical values in each path tracked by the Lagrangian method. Solid blue, dashed orange, and dash-dot green lines mean gas pressure p, magnetic pressure $B^2/8\pi$, and plasma speed $|\boldsymbol{v}|$. The units are $3.97 \times 10^4 \, \mathrm{erg}\, \mathrm{cm}^{-3}$ for gas and magnetic pressure and $6.32 \times 10^5 \, \mathrm{cm}\, \mathrm{s}^{-1}$ for plasma speed. The black lines shown in (b), (c), and (d) indicate the time when the gas pressure increases in each path.
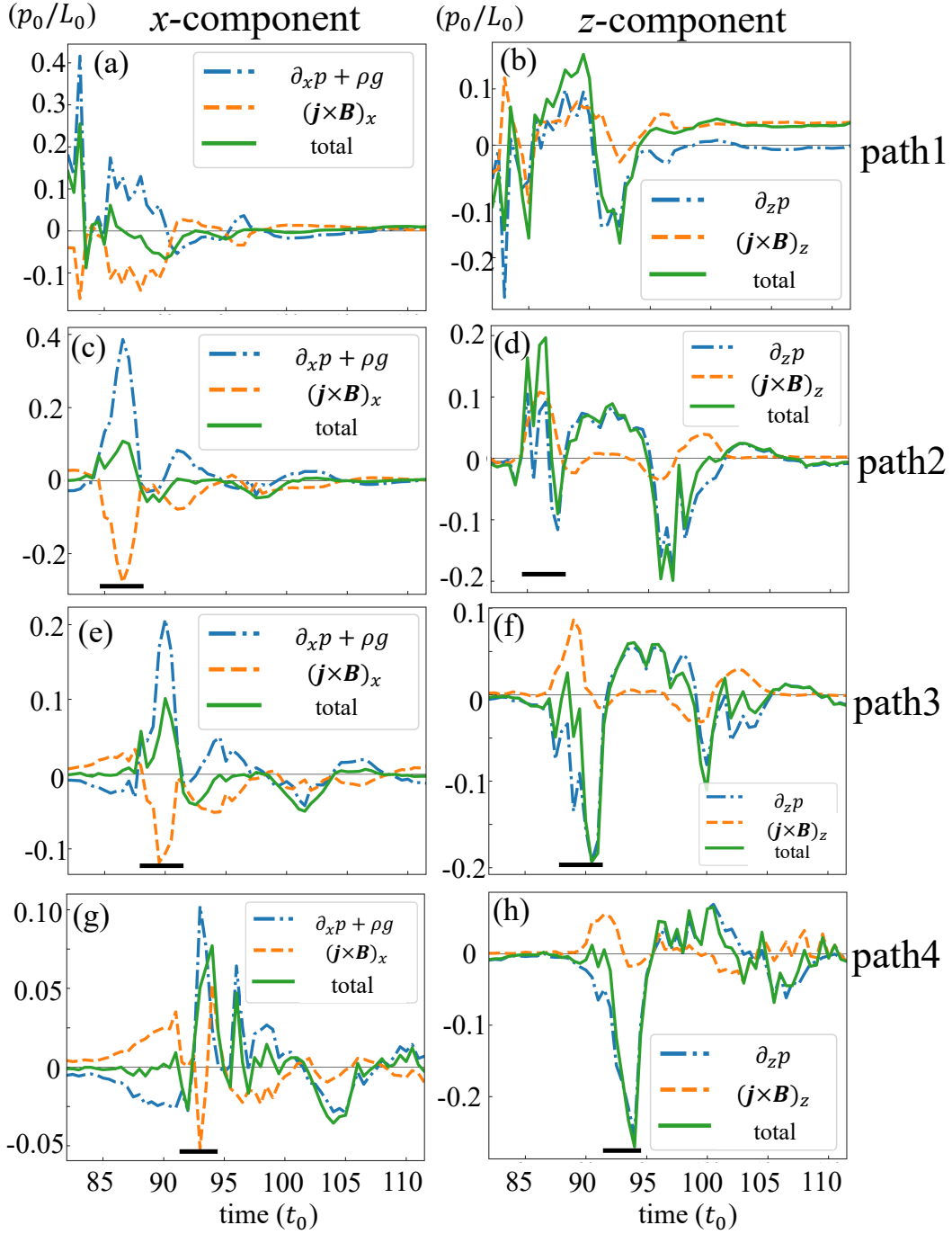
Figure 4.11: Time evolution of the forces acting on the plasma on each path. The left column shows the x-component of the force, and the right column shows the z-component. Each row shows the respective path shown in Figure 4.9. Dash-dot blue, dashed orange, and solid green lines mean gas pressure gradient and gravity, Lorentz force, and total force. The black lines shown in (c)–(h) indicate the time when the gas pressure increases in each path in figure 4.10.

structure is the result of the slow shock propagating along a uniform background magnetic field observable in figures 4.5d, 4.5h, 4.5l, 4.8, and 4.12.

Figure 4.11 displays the temporal evolution of the forces acting on each path indicated in figure 4.9. We can observe that the upward gas pressure gradient is predominant in the x-component of the force when the gas pressure is increased. Conversely, in the z-component, the positive Lorentz force functions mainly at first; however, the difference with the gas pressure gradient is small, and the negative gas pressure gradient ultimately prevails. Considering that the magnetic field and gas pressure change rapidly in the slow shock and the value of plasma β is approximately one, the behavior of these forces is consistent with the behavior when passing through the slow shock. After passing through the slow shock, the force acting on the plasma becomes increasingly less and settles into a new equilibrium state. These facts also indicate that the jet-like structure is not formed by reconnection outflow re-accelerated in the direction of the background magnetic field; rather, it is formed by compression due to the slow shock propagating in the background field's direction. That is, this jet-like structure is not mass motion; rather, it is a slow shock propagation.

Note that this formation mechanism is different from previous studies regarding coronal and chromospheric cases. In the coronal 2D simulation by Yokoyama & Shibata (1996), hot jets are created by gas pressure increasing with a fast shock formed when reconnection outflow collides with the background field. In the 2D simulation in both the corona and chromosphere (Yokoyama & Shibata, 1996; Takasao et al., 2013), the magnetic centrifugal force working in reconnected field lines drives cool jets. In these cases, a slow shock propagates approximately in the direction of the reconnection outflow, and the outflow is re-accelerated in the direction of the background field by the gas pressure gradient or Lorentz force. These mechanisms are different from our photospheric case, where the slow shock propagates approximately along the reconnected field lines and the reconnection outflow is not re-accelerated. 3D simulation in the corona (e.g., Pariat et al., 2009) shows that jets are accelerated by nonlinear torsional Alfvén waves released from the twisted sheared loop. In this case, the jets are accelerated by the magnetic pressure gradient. In our simulation, a twist of the reconnected field lines can be observed (figure 4.4) and Alfvén waves are generated (figure 4.14); however, they do not function well regarding the compression and acceleration of the plasma.

These differences from previous studies are due to our reconnection occurring in the region $\beta \sim 3 - 4$. In the $\beta \sim 3 - 4$ case, the reconnection outflow is subsonic; hence, a fast shock cannot be created where the outflow collides with the background field. Furthermore, because the magnetic energy is not dominant, it is difficult to accelerate the plasma using only the Lorentz force. However, a slow shock can be made if reconnection occurs.

There are several possible causes for the slow shock immediately propagating in the
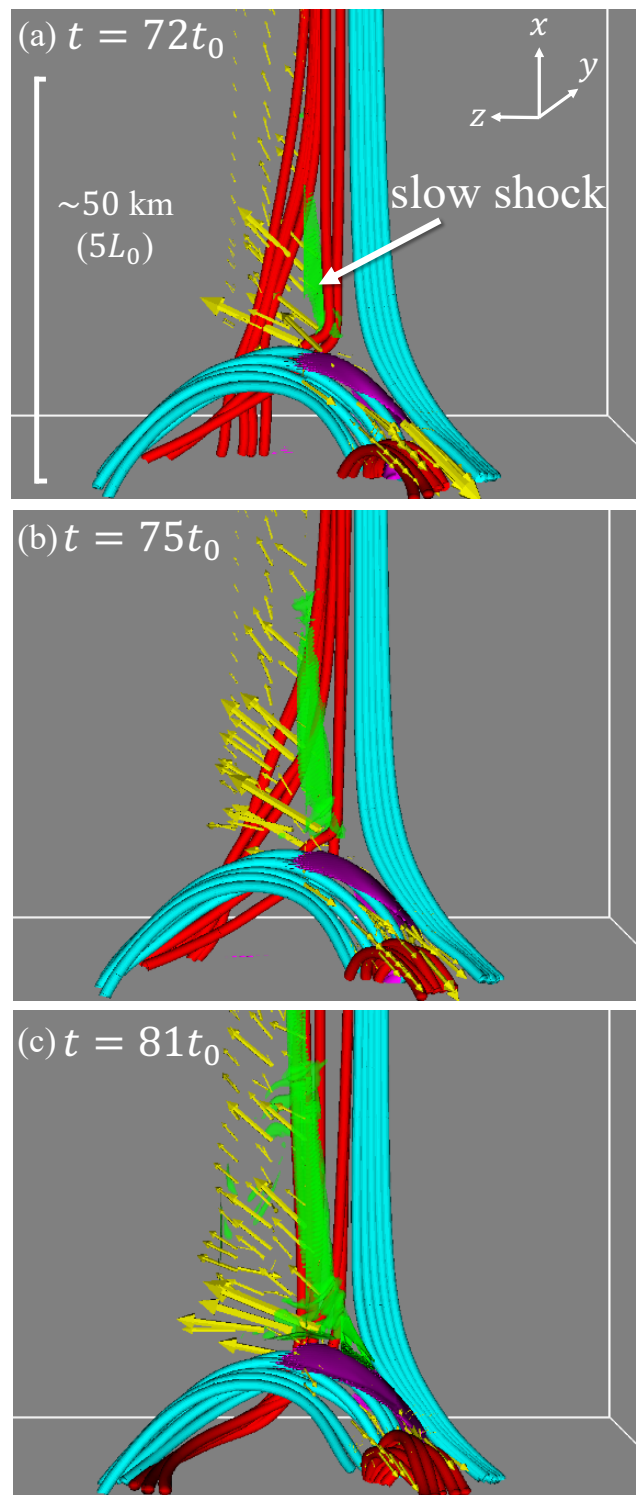
Figure 4.12: 3D diagrams where the slow shock created by reconnection propagates in the direction of the background magnetic field. Green surface means $\mathrm{div}v = -0.09/t_0$ and $-0.07/t_0$, which corresponds to a slow shock created by reconnection. (a), (b), and (c) show $t = 72t_0$, $75t_0$, and $81t_0$ cases. the color of magnetic field lines, the pink surface, and the yellow arrows indicate the same as figure 4.4.

background direction. First, our reconnection outflow is subsonic; hence, it can bend before it collides with the background field. Secondly, the phase speed of the slow shock in the direction of the magnetic fields is Alfvén speed when $\beta \gg 1$. Therefore, the slow shock is unlikely to propagate in the outflow direction, unlike in the case of $\beta \ll 1$. Consequently, the slow shock is bent immediately after being formed on the current sheet and propagating in the background magnetic field (see figure 4.13).

Note that if these photospheric jet-like phenomena are observed, it is expected that the apparent speed obtained from the imaging observation and the line-of-sight speed obtained from the spectroscopic observation are different. In our simulation, the jet-like structure propagates at approximately $0.8v_0 = 5.04\,\mathrm{km\,s^{-1}}$, corresponding to Alfvén speed. Conversely, the speed of the plasma accelerated by the slow shock is approximately $0.35v_0 = 2.2\,\mathrm{km\,s^{-1}}$, which is approximately half the propagation speed of the slow shock.

4.4.2 MHD wave propagation toward upper atmosphere

To determine the energy flux of Alfvén wave F_A, slow mode wave F_slow, and fast mode wave F_fast are passing through the $x = \mathrm{const}$ plane, we calculate these as follows:

$$F_\mathrm{A} = \frac{1}{4\pi} \frac{\int B_{0x}\boldsymbol{v}_\perp \cdot \boldsymbol{\delta B}_\perp dS}{\int dS} \tag{4.17}$$

$$F_\mathrm{slow} = \frac{\int \frac{B_{0x}}{B_0} v_\parallel \delta p dS}{\int dS} \tag{4.18}$$

$$F_\mathrm{fast} = \frac{1}{4\pi} \frac{\int B_{0x}\delta B_\parallel v_\perp dS}{\int dS} \tag{4.19}$$

$$F_\mathrm{kin} = \frac{\int \rho v^2 v_x dS}{\int dS}. \tag{4.20}$$

In the above equations, $\boldsymbol{\delta B} = \boldsymbol{B} - \boldsymbol{B}_0$ and $\delta p = p - p_0$. The subscript "0", $\perp$, and $\parallel$ are the values in the initial condition, direction normal, and parallel to the initial magnetic fields, respectively. F_kin is the kinetic energy flux passing through the $x = \mathrm{const}$ plane.† We set an integration range as the region where the absolute value of each energy flux exceeds 25% of the maximum value of the absolute value of the energy flux. We measure these values in the $x = 7.5L_0$, $15L_0$, and $22.5L_0$ planes, where plasma $\beta \simeq 2.0$, 1.25, and 0.8. Note that equations (4.18) and (4.19) correspond to magnetosonic waves in the region where β is less than one, and do not strictly correspond to the wave's energy flux. This is because the direction of the magnetosonic wave oscillation changes when β is greater than one. However, regardless of the β value, equations (4.17) and (4.18) correspond approximately to the components of the Poynting and enthalpy fluxes in the direction of the initial magnetic field, and equation (4.19) corresponds to the component normal to the initial field of the Poynting flux.

photospheric case ($\beta > 2/\gamma = 1.2$)

**coronal/chromospheric case
($\beta < 2/\gamma = 1.2$)**

$\cdot$ − − − : **slow shock** ——— : **fast shock**

⇨ : **reconnection outflow**

✖ : **reconnection point**
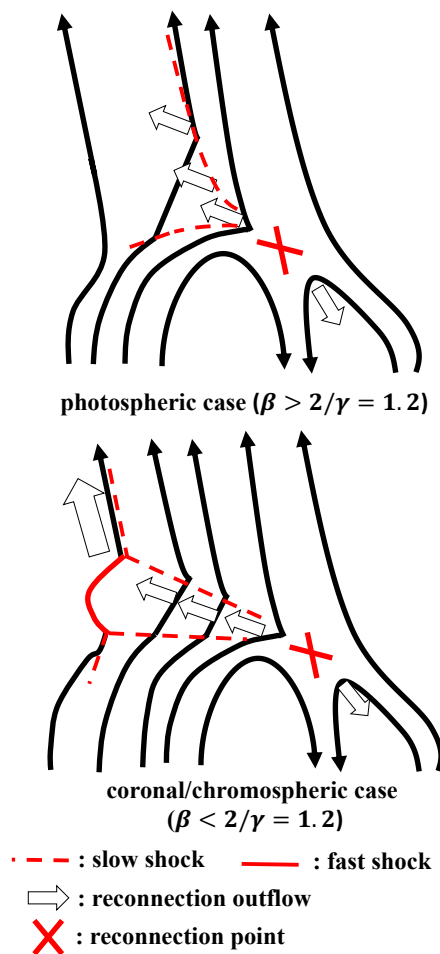
Figure 4.13: Schematic diagrams of the difference in slow shock propagation direction due to the difference in plasma β. $\gamma = 5/3$ is the specific heat ratio.

Figures 4.14a, 4.14c, and 4.14e display the result. At first, all mode waves are released, which corresponds to the sheared loop rising phase (figure 4.2b). The release of all modes in reconnection is the same as the results of Kigure et al. (2010). The reason for Alfvén wave dominance at $x = 7.5L_0$ is that the velocity in the z-direction, which is perpendicular to the initial background magnetic field, is the greatest. Subsequently, the twist of the sheared loop is released by magnetic reconnection, and the energy flux of the Alfvén mode becomes dominant in all planes. These features indicate that the jet-like structure is in Alfvénic motion, and also suggest that the reconnection process is similar to previous studies of coronal jets (e.g., Pariat et al., 2009; Archontis & Hood, 2013; Wyper et al., 2018). In each plane, all modes have approximately $10^8 \, \mathrm{erg \, cm^{-2} \, s^{-1}}$ in the $x = 22.5L_0$ plane. Moreover, the kinetic energy flux is smaller than the energy flux of the waves. This indicates that the nonlinearity of the plasma's motion forming the jet-like structure is not

strong.

Figures 4.14b, 4.14d, and 4.14f display the mean value of the Mach number $M_s = v_\parallel/c_s$ and Alfvén Mach number $M_A = v_\perp/V_A$ in the area where slow and Alfvén mode is passing at each time. From these figures, we can observe that the peak value of each Mach number is approximately 0.1; this value is consistent with the case of the coronal jets (Yokoyama & Shibata, 1999). Furthermore, the Alfvén Mach number decreases with height, yet the Mach number of sound waves remains virtually unchanged. This is because, in our numerical settings, the Alfvén speed increases with height and the sound speed is uniform.

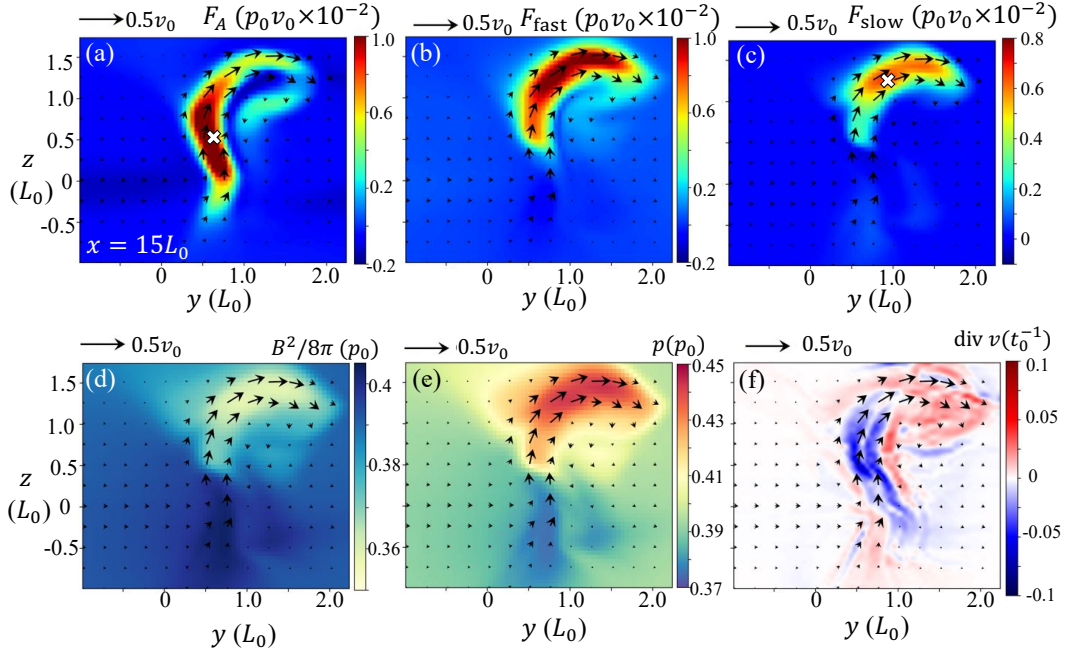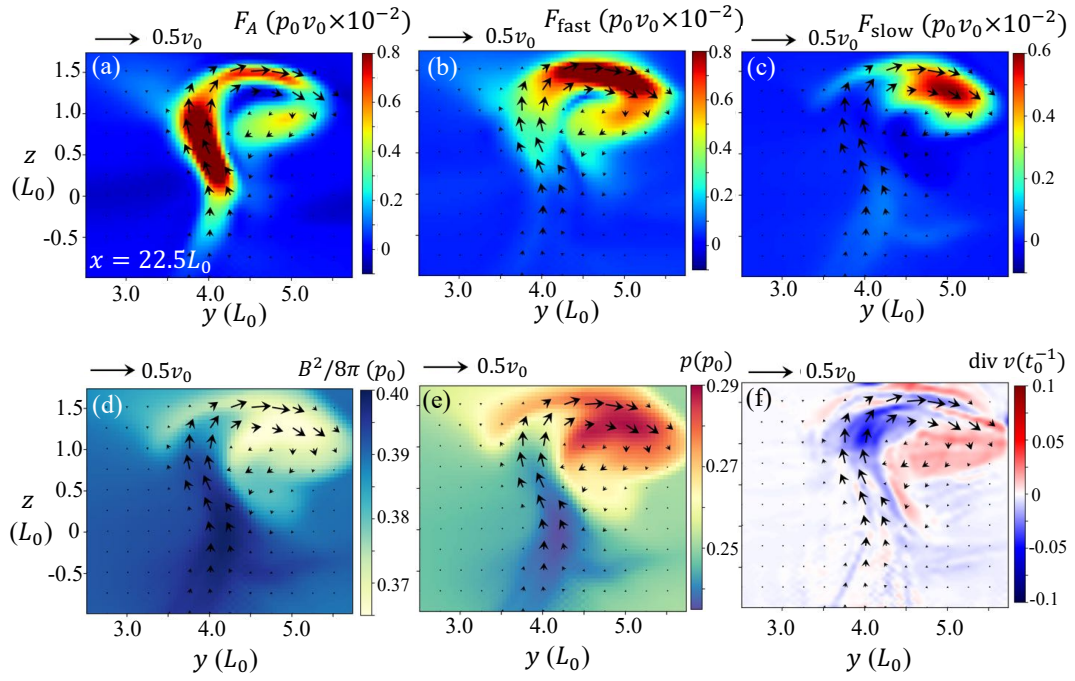Figures 4.15, 4.16, and 4.17 display the energy flux of each wave and the distribution of the magnetic and gas pressures and $\mathrm{div}v$ in the $x = 7.5L_0$ and $x = 15L_0$ planes at $t = 110t_0$ and $x = 22.5L_0$ plane at $t = 122t_0$. From these figures, we can observe that the gas pressure increases and magnetic pressure decreases in the region of intense slow mode energy flux. Moreover, the jet-like structure can be observed to be in vortex motion. In figure 4.15, the region with strong wave energy flux is in virtually the same place, adjacent to the region with strong $\mathrm{div}v < 0$. In figures 4.16 and 4.17, the regions with strong wave fluxes differ from each mode. In particular, it can be observed that the strong Alfvén wave region is where the magnetic pressure is strong, which is different from the region of the strong slow mode. Moreover, the strength of $\mathrm{div}v$ is weaker than in the $x = 7.5L_0$ plane.

The reason the position of the peak of each mode is shifted as it rises is that the propagation speed of the slow mode and the Alfvén mode is different in the upper region. Figure 4.18 displays the 3D relationship between the yz planes indicateing the distribution of the energy fluxes and magnetic field lines at $t = 110t_0$. Considering the vortex motion observable in figures 4.15, 4.16, and 4.17, we can observe that a magnetic field line, along which waves propagate, moves in the order of the green, light blue, and red line with time. Figure 4.19 displays the time evolution of the distribution of energy fluxes along the magnetic field lines passing through a region with a strong slow mode in the $x = 7.5L_0$ plane. From this figure, we can observe that the positions of the peaks of the Alfvén mode and slow modes are virtually the same in the lower part, and that the Alfvén mode precedes in slow mode in the upper part. This is because where β is greater than $2/\gamma$, the slow mode propagates at the Alfvén velocity along the magnetic field line; however, below $2/\gamma$, it propagates at the sound speed. From these facts, the position of the energy flux peaks appearing in the yz cross section is different in the upper part because the slow mode passes after the Alfveń mode along the vortex-moving magnetic field lines.

We also investigated the effects of MHD waves generated from photospheric anemone jet-like structures on the upper atmosphere. From a simple estimate, we determined that the MHD wave's energy flux achieving a height of $500\,\mathrm{km}$ was approximately $4 \times$
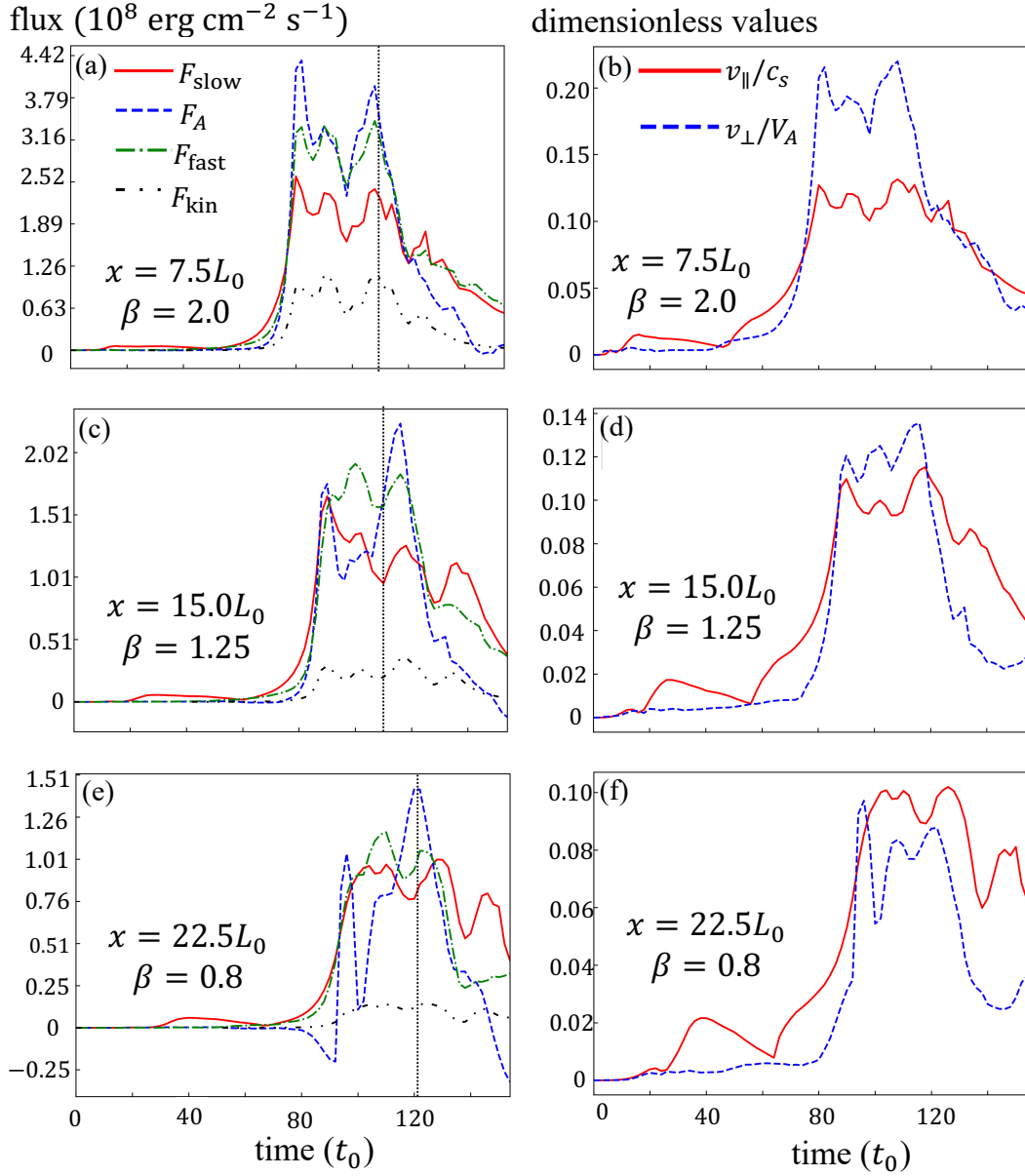
Figure 4.14: (a), (c), (e): Time development of MHD wave energy flux passing through $x = 7.5L_0$, $15L_0$, and $22.5L_0$ plane. Dashed blue, solid red, and dash-dot green lines show Alfvén, slow, and fast mode. Dash-dot-dot black lines indicate kinematic energy flux. The dotted line shown in (a) and (c) indicates $t = 110t_0$, the time shown in figures 4.15 and 4.16. The dotted line indicated by (e) denotes $t = 122t_0$, which is the time indicated in figure 4.17. (b), (d), (f): Time development of Mach number of Alfvén and sound wave. Blue dashed and red solid lines show Alfvén and sound waves.
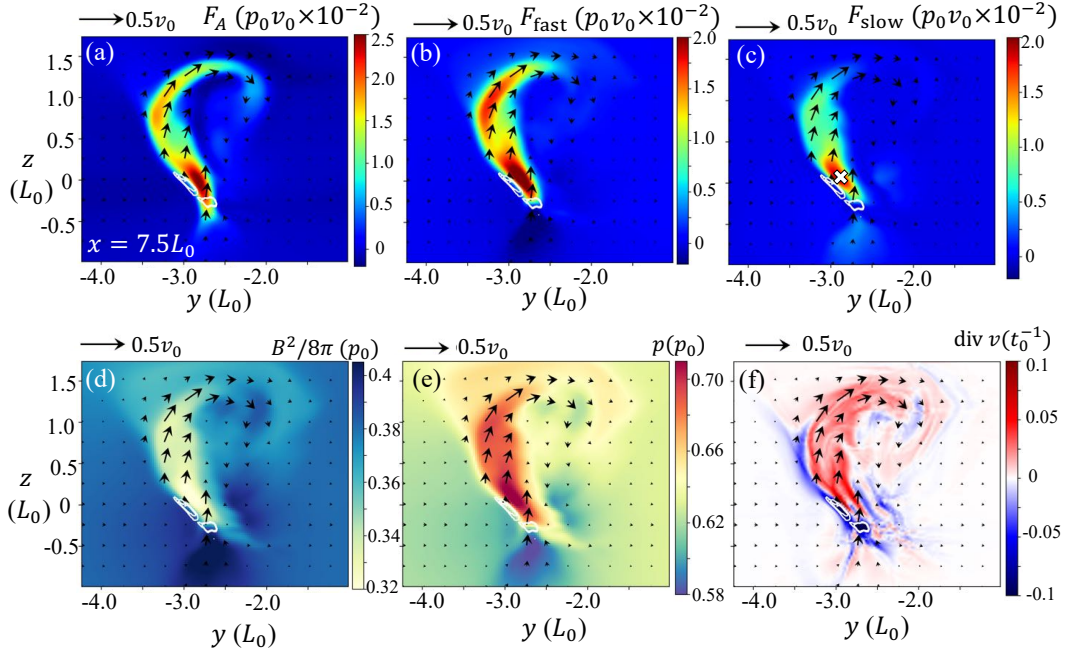
Figure 4.15: Energy flux of each wave and the distribution of magnetic and gas pressures and $\text{div}v$ in the $x = 7.5L_0$ plane at $t = 110t_0$. Black arrows show velocity in the plane. White contours indicate $\text{div}v = -0.07t_0^{-1}$ and $-0.09t_0^{-1}$. The white x mark in (c) indicates the area where the magnetic field line is passing through in figure 4.18.

$10^7 \, \text{erg}\,\text{cm}^{-2}\,\text{s}^{-1}$ (see Appendix B.1). This value is marginally greater than the amount required for chromospheric heating (Withbroe & Noyes, 1977). Because of the small lifetime of the phenomenon, these waves are high frequency, and we can observe from figure 4.14 that the period is approximately $20t_0 \sim 30\,\text{s}$. This implies that the photospheric anemone jet-like structure could be one of the origins of the high-frequency Alfvén waves that have been observed in the spicules (He et al., 2009; Okamoto & De Pontieu, 2011), though other candidates exist, such as mode conversions of longitudinal to transverse waves (Shoda & Yokoyama, 2018). Furthermore, we extended the computational domain to the corona and performed 1D hydrodynamic simulations. From the results of the simulations, we determined that the photospheric jet-like structure can also influence the spicule formation (see Appendix B.2). Note that these estimates are simplistic and should be studied in more detail in future papers.

4.5 Conclusion

We performed 3D MHD simulation of anemone jet-like structures in the solar photospheric parameter. From the results of the simulation, a jet-like structure was induced by magnetic

Figure 4.16: Energy flux of each wave and the distribution of magnetic and gas pressures and $\mathrm{div}v$ in the $x = 15L_0$ plane at $t = 110t_0$. Black arrows show velocity in the plane. The white x mark in (c) indicates the area where the magnetic field line is passing through in figure 4.18.

reconnection. The length, width, lifetime, and apparent velocity of the jet-like structure were extensions of the coronal and chromospheric anemone jets. This jet-like structure was formed by the propagation of the slow shock generated by magnetic reconnection. These facts indicate that the anemone jet-like structure, which can be explained by the unified model (Shibata, 1999; Shibata et al., 2007), is expected to exist in the solar photosphere; however, the formation process of the jet-like structure is different from that in the low β environment of the chromosphere and corona. In the present study, we simulated a jet-like structure with a length of approximately $100\,\mathrm{km}$. However, such a jet-like structure is expected to be formed in an environment where the plasma β is greater than one, even though the scales are different.

We also confirmed, for the first time, that the magnetosonic and Alfvén waves are generated by magnetic reconnection in the solar photospheric parameters in a 3D manner. These waves are high frequency, and their non-dimensional amplitudes are comparable with those of the coronal case. Furthermore, the MHD wave energy fluxes were generated to the degree that could influence the local chromospheric heating and the formation of spicules.

Figure 4.17: Energy flux of each wave and the distribution of magnetic and gas pressures and $\mathrm{div}v$ in the $x = 22.5L_0$ plane at $t = 122t_0$. Black arrows show velocity in the plane.
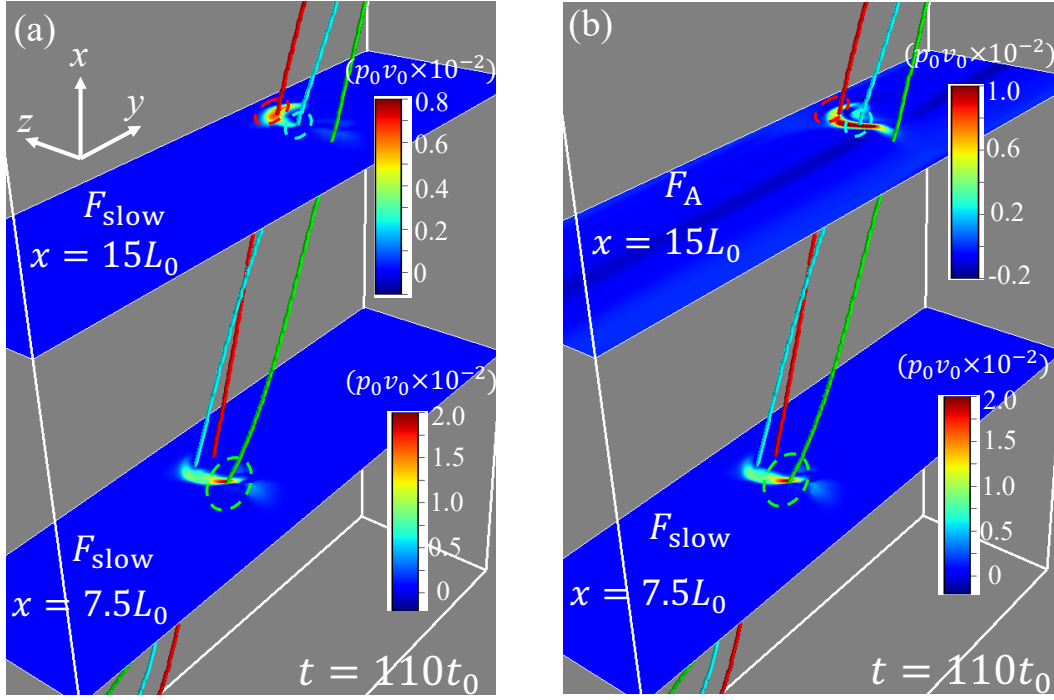
Figure 4.18: 3D relationship between the yz plane showing the distribution of energy fluxes and magnetic field lines at $t = 110t_0$. In (a), we show the distribution of slow mode energy flux in the $x = 15L_0$ plane shown in figure 4.16c, and in (b), we show that of Alfvén mode shown in figure 4.16a. In both figures, the $x = 7.5L_0$ plane shows the distribution of slow mode energy flux shown in figure 4.15c. The green line indicates a magnetic field line passing through a region with a strong energy flux in the $x = 7.5L_0$ plane. The light blue line shows a magnetic field line passing through a region with a strong energy flux of Alfvén mode in the $x = 15L_0$ plane, and the red lines show a magnetic field line passing through a region with a strong energy flux of slow mode in the same plane. The three dashed lines surrounding the magnetic field lines indicate the region through which each magnetic field line passes.
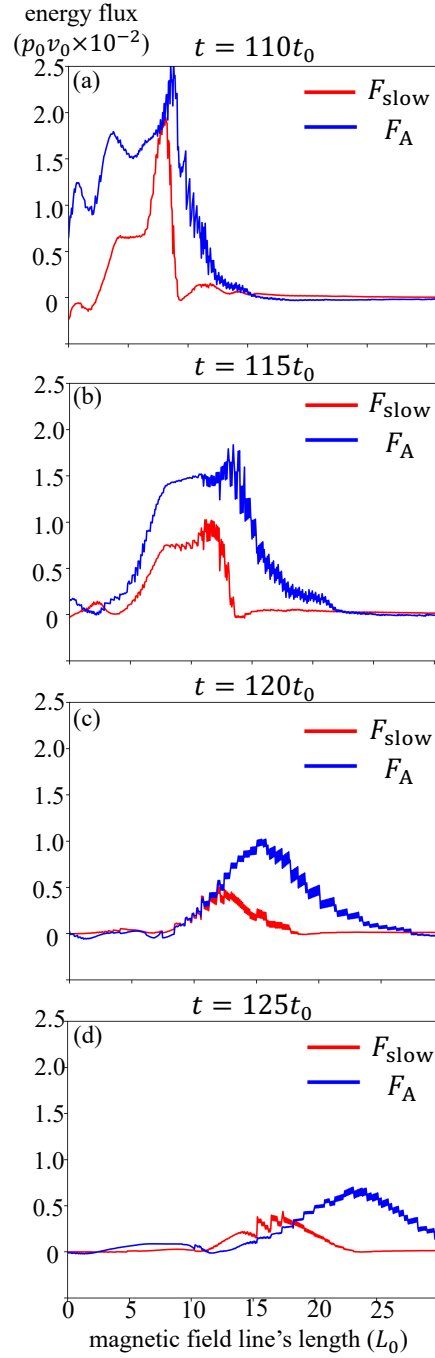
Figure 4.19: Time evolution of the distribution of energy fluxes along the green magnetic field line shown in figure 4.18, which is passing through a region with a strong slow mode in the $x = 7.5L_0$ plane. The time evolution is calculated by tracking the magnetic field line in a Lagrangian way. The horizontal axis shows the length of the magnetic field line when the bottom surface is set to zero. The red and blue lines show the slow and Alfvén mode energy fluxes, respectively. (a), (b), (c), and (d) show the distribution at $t = 110t_0$, $115t_0$, $120t_0$, and $125t_0$, respectively.

Concluding Remarks

5.1   Conclusion

In this thesis, I studied small flares and their associated dynamics on the Sun to understand their unified relationship with large-scale solar flares. I summarize below the results obtained in this thesis.

As an important thermal property of small flares in the quiet Sun of the corona, I have found the following observational evidence of chromospheric evaporation/condensation (Chapter 2):

· Redshifts associated with line center brightening are found in the Hα line.

· Observed emission measures (EM) and temperatures follow the scaling law suggested by Shibata & Yokoyama (1999, 2002).

· In the time evolution of temperature and density during a small flare, the temperature reaches its maximum value before the density.

These results suggest that the chromosphere plays a significant role in the thermal response of some small flares in the quiet Sun, similar to its role in large flares. The existence of chromospheric evaporation/condensation also significantly impacts theoretical models of nanoflare heating and its proper verification methods in observations (see details for Section 2.5).

I obtained the physical quantities of the cold ejecta associated with the small flares that occur in the solar corona for the first time in many events (Chapter 3). By comparing large solar flares and stellar flares with their associated cold ejecta, I have found a correlation between the physical quantities of the ejecta and the total flare energy over more than ten orders of magnitude. The key results for the correlations found in this study are as follows:

(i) The mass of the ejecta is roughly proportional to the $2/3$ power of the total flare energy. This power-law index is similar to the case of coronal mass ejections (CMEs) (Aarnio et al., 2011; Drake et al., 2013; Takahashi et al., 2016).

(ii) I derive a theoretical scaling law between the mass of cold ejecta and the total flare energy from simple assumptions. This scaling law explains the distribution discrepancy between small flares in the quiet Sun of the corona and large solar/stellar flares due to differences in the coronal magnetic field strength.

(iii) I also find correlations between the ejecta's velocity/kinetic energy and total flare energy. The upper limit of the velocity is proportional to approximately $1/6$ power of the total flare energy. The kinetic energy is proportional to approximately $2/3$ power of the total flare energy.

These results quantitatively support the interpretation that minifilament eruptions associated with small flares in the corona are miniature versions of filament eruptions associated with large flares. The correlations found in this study will be helpful in quantitatively understanding the properties of the smaller reconnection events and associated plasma eruptions below the solar chromosphere (e.g., Shibata et al., 2007). These correlations also include flares in M-type stars. Hence, it can also be used to provide quantitative support for detecting associated stellar filament eruptions for a wide range of stellar flares in both G- and M-type stars.

One of the primary goals of this thesis is a unified understanding of the dynamics resulting from flares (magnetic reconnection) in the photosphere, chromosphere, and corona. For this purpose, I performed the first 3D magnetohydrodynamics (MHD) simulations of magnetic reconnection in an environment assuming the solar photosphere (Chapter 4). The key results obtained from the numerical simulations are as follows:

(I) Magnetic reconnection occurs in the photosphere in a similar way to the coronal case.

(II) In contrast to the coronal case, a collimated flow along the ambient magnetic field (jet) does not occur due to the interaction between the flow or shock associated with reconnection and the ambient plasma.

(III) The slow shock formed by magnetic reconnection propagates through the ambient magnetic field, causing an elongated structure with enhanced density.

The key word to understand the results of (II) and (III) is "plasma β." As the plasma β is typically greater than 1 in the photosphere, a terminal fast shock cannot form, nor can the Lorentz force strongly accelerate the ambient plasma. On the other hand, because Alfvén

velocity is subsonic, slow shocks propagating at Alfvén velocity can easily bend in the direction of the ambient magnetic field. Thus, a density increase structure is easily formed in the direction of the ambient field. My research has clearly shown that differences in plasma β cause changes in jet dynamics. In addition, waves generated by the reconnection in this simulation have enough energy to affect spicule formation and chromospheric heating. This result suggests that photospheric magnetic reconnection could affect other dynamics/heating in the upper chromosphere.

Through the study of small flares on the Sun performed in this thesis, I have provided positive evidence for the idea that flares of various sizes and their associated dynamics are connected through magnetic reconnection (Figures 1.17 and 1.19). In Chapters 2 and 3, I found much new observational evidence that small flares with cool chromospheric mass ejections in the quiet Sun of the corona are caused by a similar physical mechanism as large solar flares. From my observational studies, I can infer that small flares in the quiet Sun differ from large flares only in the magnetic field strength and spatial scale. In Chapter 4, I found by numerical simulation that the dynamics of magnetic reconnection in the solar photosphere differ from those in the chromosphere and corona. Based on the previous numerical simulations in the corona and chromosphere (e.g., Yokoyama & Shibata, 1996; Shimojo et al., 2001; Takasao et al., 2013), I conclude that the essential factors that determine the dynamics due to magnetic reconnection are "the height at which reconnection occurs," that is, "plasma β" and "positional relationship with the contact discontinuity (transition region)." When reconnection occurs in $\beta < 1$, Lorentz force and the gas pressure enhanced by the terminal fast shock can accelerate jets (Yokoyama & Shibata, 1996; Pariat et al., 2009; Takasao et al., 2013). In contrast, when reconnection occurs in $\beta > 1$, jets are not accelerated and only elongated structures are formed due to slow shocks, as shown in results (II) and (III) above. Regarding the location of the transition region, when reconnection occurs above the transition region (corona), chromospheric evaporation flow forms a dense jet (Shimojo et al., 2001). The dynamics of reconnection occurring below the transition region depend on the distance between the transition region and the site of reconnection. When reconnection occurs near the transition region, such as in the upper chromosphere, the slow shock formed by reconnection interacts with the transition region to form a low-temperature, high-density jet (Takasao et al., 2013). When reconnection occurs in the lower chromosphere/photosphere far below the transition region, the slow shock formed by the reconnection does not directly affect the upper atmosphere. However, the waves generated by the reconnection can grow into a shock and form a new chromospheric jet (this thesis and Takasao et al., 2013). As the above picture depends on only two fundamental factors - the presence of a transition region and the variation of plasma β with height - it would be reasonable to expect it to apply to other stellar atmospheres.

5.2 Future perspective

- Thermal properties of small flares in the quiet Sun of the corona -

In Chapter 2, I found evidence of chromospheric evaporation/condensation in some small flares in the quiet Sun of the corona, similar to large solar flares. However, some mysteries remain in the complete understanding of its physical mechanism, as follows:

· The present observation may not correctly diagnose temperatures in the steady state or decay phase of small flares (Section 2.4.3). This may be because the AIA temperature response functions have their peak roughly above $10^{5.8}$ K (Landi et al., 2013). Thus, I have not been able to conclude in this thesis how the small loops in the quiet Sun exist under a steady state. Whether small flares in the quiet Sun can also form post-flare loops is an interesting question but remains a mystery.

· Because 25 events were visually selected for our observations, the discussion of the percentage of those undergoing chromospheric evaporation/condensation is incomplete. The conditions under which the temperature peak precedes the density peak in the flare time evolution are also unresolved. Resolving these problems would be essential to solving the nanoflare heating problem.

· Although I found evidence of chromospheric condensation in this observation, the actual amount of energy transported to the chromosphere has not been quantitatively determined. This problem would be important in discussing flare energy partition and the nanoflare heating problem.

· Recent Solar Orbiter/EUI observations have revealed small flares in the quiet Sun with smaller spatial scales ($< 1000\,\mathrm{km}$) than our observation. Whether chromospheric evaporation/condensation occurs in those smaller flares is still unresolved.

The first way to solve these problems is to examine them with 3D radiative magneto-hydrodynamics (RMHD) simulations. In recent years, 3D RMHD simulations have been actively performed to reproduce small flares in the quiet Sun and have succeeded in reproducing their observed properties (e.g., Chen et al., 2021; Tiwari et al., 2022; Panesar et al., 2022a). Numerical simulations can provide direct information on temperature and density variations, which is expected to provide robust insights into the above problems. To observationally verify the above problem, an instrument capable of high resolution (spatial resolution: < 0.5 arcsec, temporal resolution: < 12 sec) over a wide range of temperatures from 10^4 K to 10^6 K would be required. Because the Solar-C/EUV High-throughput Spectroscopic Telescope (EUVST) meets all of these conditions, the Solar-C/EUVST observations would make significant progress in understanding small flares in the quiet Sun.

In addition to the above problems, the physical mechanisms related to nonthermal particles that can cause chromospheric evaporation and condensation are currently unknown in small flares in the quiet Sun. There are many challenging and unexplored issues related to nonthermal particles, even in large solar flares. Specifically, the following issues remain:

- Heat transporting mechanism to the chromosphere

  The mechanism for transporting heat generated by reconnection in the corona to the chromosphere is not yet understood. This problem is also controversial in large flares. The prevailing theory is that nonthermal particles transport them (e.g., Syrovatskii & Shmeleva, 1972; Masuda et al., 2001), but some observations suggest that thermal conduction transports them (Czaykowska et al., 2001; Battaglia et al., 2009). Another theory proposes that they are transported by Alfvén waves (Emslie & Sturrock, 1982). In Chapter 2, transport by thermal conduction was assumed, but the actual transport mechanism in small flares remains an issue to be validated.

- Particle acceleration mechanism

  Does particle acceleration occur in small flares in the quiet Sun? If it occurs, what is its physical mechanism? The acceleration mechanism of nonthermal particles has not been determined at all, even in large flares (see the reviews Aschwanden, 2002; Benz, 2017). For small flares in the quiet Sun, the acceleration mechanism for nonthermal particles and observational evidence of their presence are still unknown. Recently, the *Nuclear Spectroscopic Telescope ARray* (NuSTAR: Harrison et al., 2013) captured small flares in the quiet Sun for the first time through X-ray imaging spectroscopic observations (Kuhar et al., 2018). Further events are expected to be observed by the NuSTAR and by higher-resolution telescopes.

- Blue asymmetry in the chromospheric lines

  Can we observe blue asymmetry in the chromospheric lines even for small flares in the quiet Sun? Blue asymmetry in the chromospheric lines is sometimes observed in large flares (e.g., Švestka et al., 1962; Tei et al., 2018). Tei et al. (2018) proposed that the blue asymmetry may be caused by nonthermal electrons being injected deep into the chromosphere, resulting in the formation of a hot plasma layer under a cold plasma layer. While we could not observe them in Chapter 2 of this thesis, searching for evidence of blue asymmetry in small flares in the quiet Sun as a possible indication of the presence of nonthermal electrons is an intriguing topic.

Investigating the questions above using small flares in the quiet Sun may help to constrain theories about nonthermal particles in flares, as these events can be studied under different parameters such as spatial scale and magnetic field strength. In addition, due to the higher occurrence rate of small energy flares, future high-sensitivity observations may be able to shed light on the previously mentioned questions through the analysis of their statistical properties.

- Correlation between physical quantities of the ejecta at the chromospheric temperature and flare energy -

In Chapter 3, I found the correlations between the physical quantities of the ejecta and the flare energies over ten orders of magnitude. The remaining issues on this topic are as follows:

(a) Statistical analysis with larger sample sizes

> In this study, I analyzed 25 small flares in the quiet Sun and ten solar flares greater than GOES A-class. These sample sizes are much smaller than in the statistical studies of CMEs (e.g., Yashiro & Gopalswamy, 2009). In addition, I visually detected small flares in the quiet Sun, and future work should involve attempting automatic detection to perform more statistical analysis.

(b) Justification of the definition of total flare energy

> In section 3.4.3, it was mentioned that the present analysis estimates the total flare energy using a large set of assumptions. The method of defining the total flare energy should be reexamined more carefully in the future.

For issue (a), future studies should include an analysis of minifilament eruptions in active regions (e.g., Sterling et al., 2019) and giant arcades in the quiet Sun. Including these events would allow us to complete the correlation for all flares observed in the solar corona in the present. New trends may be discovered by analyzing phenomena with the same spatial scale as the present analysis but with different magnetic field strengths, as shown in Figure 2.8 in Chapter 2 of this thesis. The magnetic field strength of stellar flares is thought to be stronger than those of solar flares (e.g., Namekata et al., 2017b; Maehara et al., 2021). Hence, investigating how the physical quantities of various solar flares vary with the strength of the magnetic field would also be important for stellar flare studies.

Issue (b) is highly related to the flare energy partition problem (see the review of Warmuth & Mann, 2020), which is a fundamental problem and challenging to verify. This problem is important not only for the current study, but also for any future studies that aim to discuss correlations across a wide range of flare energies. For example, as discussed in Section 2.5, this problem will be important for the nanoflare heating problem. I have

proposed using coronal field extrapolation to estimate the magnetic energy released by reconnection to determine total flare energies. By considering the magnetic energy thus estimated as the total flare energy and examining the correlation between the energy and GOES X-ray flux or bolometric energy, a beneficial relationship may be obtained for estimating the total flare energy. Emslie et al. (2012) performed a similar analysis. However, recent progress in coronal field extrapolation methods, such as nonlinear force-free field modeling (e.g., Moraitis et al., 2014; Jing et al., 2018; Wiegelmann & Sakurai, 2021), has been remarkable, and new findings could be obtained. Through these analyses, it may be possible to make quantitative estimates of the magnetic energy released by reconnection, even if the problem of flare energy partition is not solved.

- Dynamics resulting from magnetic reconnection in the photosphere -

In Chapter 4, I performed 3D MHD simulations and clarified the magnetic reconnection properties and resulting dynamics in the solar photosphere. However, this simulation only calculates the toy model for a specific set of parameters, and further studies will be necessary to validate the results. Specifically, the following developments are possible:

(A) Parameter survey in a toy model,

(B) More realistic numerical simulation incorporating the convective motion of the Sun and the effects of partially ionized plasma,

(C) Observational validation with high-resolution telescopes.

In particular, we plan to study issue (C) using the Daniel K. Inouye Solar Telescope (DKIST: Rimmele et al., 2020), a 4-meter solar telescope that has begun scientific observations. With the DKIST/Visible Broadband Imager (VBI: Wöger et al., 2021), it is possible to image the solar photosphere with a spatial resolution of about $20\,\mathrm{km}$. This resolution allows the exploration of reconnection and resulting dynamics in the solar photosphere with unprecedented spatial resolution. This observation may allow us to understand the dynamics resulting from reconnection in the solar photosphere and its statistical properties, as in the case of chromosphere and corona (Shibata et al., 1992, 2007; Shimojo et al., 1996; Nishizuka et al., 2011). Because the DKIST/VBI can simultaneously observe the chromosphere, the effect of photospheric reconnection on the chromosphere, such as spicule formations and chromospheric heating, can also be investigated. Furthermore, high-resolution imaging spectroscopic observations by the DKIST/Visible Tunable Filter (VTF) will start in the future, obtaining the line-of-sight velocity information of photospheric reconnection. That information may provide observational evidence of the formation process of the apparent jet-like structure caused by slow shock, which is found in this thesis. Through the above studies, our understanding of the physical mechanisms of solar photospheric reconnection will be significantly enhanced over the next decade.

Supplementary materials in Chapter 3

A.1 Derivation of the scaling law for filament mass and total flare energy

In this section, we attempt to establish a theoretical relationship between the filament's mass and the total flare energy. For this purpose, we evaluate the approximate values of the filament mass and total flare energy in the form of the filament length L. We begin to discuss the formula for evaluating the stably existing filament mass.

We assume that the filament is approximated by a rectangle of length L, height R, and width l (Figure 3.9). A stable helical magnetic field supports the filament. The radius of the helical field gives the height R of the filament.

For this helical spiral to be stable against the kink instability, R should be greater than that determined by the following Kruskal–Shafranov limit (Kruskal & Schwarzschild, 1954; Priest, 2014).

$$R > \frac{L^{'}}{2\pi} \frac{B_\psi}{B_y},\tag{A.1}$$

where $L^{'}$ is the length required for the helical magnetic field lines to make one rotation. From inequality (A.1), we assume that R is proportional to L for the filament to exist stably. $L^{'}$ should be proportional to the filament length L. Thus, we assume that the radius

R of a stably existing helical field can be expressed using the filament length L as follows:

$$R = a\frac{L}{2\pi}\frac{B_\psi}{B_y} = \frac{a}{4}\frac{L}{\pi/2}\frac{B_\psi}{B_y}, \tag{A.2}$$

where $a > 1$, B_y, and B_ψ are a constant, magnetic field strength in the filament axial direction, and an azimuthal component of the magnetic field, respectively. If we assume that $B_\psi/B_y = 0.3$ is constant in the helical field and $L \sim 5 \times 10^4\,\mathrm{km}$, we obtain $R \sim 9.6 \times 10^3 \times a/4\,(\mathrm{km})$. Thus, we set a to four to be consistent with the typical prominence height.

To estimate the filament width l, we use the analytical solution of the Kippenhahn–Schlüter model (Kippenhahn & Schlüter, 1957) only near the bottom of the helical magnetic field. Kippenhahn–Schlüter model assumes that the filament is in hydrostatic equilibrium and B_x, B_y, and temperature T are constant in the x direction. In this model, the filament gas pressure p and the vertical component of magnetic field B_z are expressed as follows (Priest, 2014):

$$p \quad = \frac{B_{z\infty}^2 - B_z^2}{8\pi} \tag{A.3}$$

$$B_z \quad = B_{z\infty} \tanh \frac{B_{z\infty}x}{2B_xH}, \tag{A.4}$$

where H is the scale height of the filament and $B_{z\infty} = B_z(x = +\infty)$. We assume that the filament width l can be approximated by the typical spatial scale of gas pressure distribution (A.3).

$$l = \frac{2B_xH}{B_{z\infty}}. \tag{A.5}$$

Based on $B_z(x = 0) = 0$, $B_x/B_{z\infty}$ can be represented using equation (A.3) as follows:

$$\frac{B_x}{B_{z\infty}} = \left(\frac{B_x^2}{8\pi p(x=0)}\right)^{1/2} = \beta_x^{-1/2}(x=0), \tag{A.6}$$

where $\beta_x^{-1/2}(x = 0)$ is the plasma β calculated from only B_x in the filament center. Thus, the filament width can be written as follows:

$$l = 2\beta_x^{-1/2}(x=0)H. \tag{A.7}$$

From the above discussion, using the filament typical density ρ, the filament mass M can be expressed as follows:

$$M = LRl\rho = \frac{4\beta_x^{-1/2}(x=0)H}{\pi}\frac{B_\psi}{B_y}\rho L^2 = \alpha L^2, \qquad (A.8)$$

$$\alpha = \frac{4\beta_x^{-1/2}(x=0)H}{\pi}\frac{B_\psi}{B_y}\rho, \qquad (A.9)$$

where α is the coefficient when rewritten in the form $M \propto L^2$ and corresponds to the coefficient of the solid black line in Figure 3.10.

By eliminating L from equations (A.8) and (3.11) and assuming the parameter values, the following relationship between filament mass M (g) and total flare energy E_{tot} (erg) can be obtained.

$$M = 9.0 \times 10^{12} \left(\frac{f}{0.1}\right)^{-2/3} \left(\frac{B_\psi/B_y}{0.3}\right) \left(\frac{\beta_x(x=0)}{10^{-3}}\right)^{-1/2}$$
$$\left(\frac{H}{250\,\text{km}}\right) \left(\frac{\rho}{3 \times 10^{-14}\,\text{g cm}^{-3}}\right) \left(\frac{B_{\text{corona}}}{50\,\text{G}}\right)^{-4/3} \left(\frac{E_{\text{tot}}}{10^{28}\,\text{erg}}\right)^{2/3} \quad (A.10)$$

We determined the parameters f of the above equation (A.10) from the ratio between the magnetic energy related to the flare and the bolometric energy (Emslie et al., 2012). In addition, for the above parameters, α in equation (A.9) takes the following values.

$$\alpha = 9.1 \times 10^{-6} \left(\frac{B_\psi/B_y}{0.3}\right) \left(\frac{\beta_x(x=0)}{10^{-3}}\right)^{-1/2} \left(\frac{H}{250\,\text{km}}\right) \left(\frac{\rho}{3 \times 10^{-14}\,\text{g cm}^{-3}}\right) (A.11)$$

The range of parameters B_ψ/B_y, $\beta_x(x=0)$, H, and ρ is estimated to be approximately the following degrees, from which we select appropriate values. As for the orientation between the filament axis and the magnetic field orientation, Hanaoka & Sakurai (2017) said that it is concentrated between $10°$ and $30°$ in both active and quiet regions. From this relationship, we can infer that $B_\psi/B_y \sim \tan 10°–30° \sim 0.176$–$0.577$. Previous studies have reported prominence electron temperatures T (K), electron density n_e (cm^{-3}), hydrogen ionization ratio χ, and gas pressure p (dyn cm^{-2}) of $4000 < T < 10000$, $10^9 < n_e < 10^{11}$, $0.2 < \chi < 0.9$, and $0.02 < p < 1$ (Labrosse et al., 2010). Assuming mean molecular weight $1/\mu = 1.5$, we can estimate scale height $H = R_g T/\mu g = 180 - 450$ (km), where $R_g = 8.31 \times 10^7$ (erg mol^{-1} K^{-1}) is the gas

constant and $g = 2.74 \times 10^4 \, (\mathrm{cm \, s}^{-1})$ is the solar gravitational acceleration. In addition, $\rho = \mu m_\mathrm{H} n \simeq \mu m_\mathrm{H} (n_\mathrm{H} + n_\mathrm{He} + n_e) = \mu m_\mathrm{H} (n_\mathrm{H}/n_e + n_\mathrm{He}/n_\mathrm{H} \times n_\mathrm{H}/n_e + 1) n_e$. Assuming $n_\mathrm{He}/n_\mathrm{H} = 0.08$ and $n_\mathrm{H}/n_e \simeq \chi$, we can derive $\rho \simeq 1.11 \times 10^{-24} (1.08\chi + 1) n_e$. The above equation shows that the ionization ratio affects only about factor 2, so assuming $\chi = 0.5$, we can estimate $\rho \simeq 1.7 \times 10^{-15} - 1.7 \times 10^{-13} \, (\mathrm{g \, cm}^{-3})$. The magnetic field strength of the quiescent prominence is estimated to be about $10 - 80$ G (Casini et al., 2003, 2005). Assuming that the horizontal component is $B_x(x = 0) = 5 - 40 \, \mathrm{G}$, we can estimate $\beta_x(x = 0) = 0.02/(40^2/8\pi) - 1.0/(5^2/8\pi) \simeq 3 \times 10^{-4}$–$1.0$ in the quiet region. On the other hand, the magnetic field strength of the active region prominence is estimated to be around $100 - 800$ G (Kuckein et al., 2009; Sasso et al., 2011; Xu et al., 2012). Thus, assuming that the horizontal component is $B_x(x = 0) = 50 - 400 \, \mathrm{G}$, we can estimate $\beta_x(x = 0) = 0.02/(400^2/8\pi) - 1.0/(50^2/8\pi) \simeq 3 \times 10^{-6}$–$1.0 \times 10^{-2}$ in the active region. A more precise determination of these parameters in future filament observations would increase the reliability of our scaling law.

Supplementary materials in Chapter 4

B.1 Photospheric reconnection effect for the chromospheric heating

Figure 4.14e indicates that each mode has approximately $10^8 \, \mathrm{erg \, cm^{-2} \, s^{-1}}$ in the $x = 22.5L_0 = 225 \, \mathrm{km}$ plane. To discuss the effect of chromospheric heating, we estimate the amount of energy flux that can reach the chromosphere at a height of $\sim 500 \, \mathrm{km}$ as follows. We consider an Alfvén wave and slow mode wave propagating along a vertical magnetic flux tube with cross section S. First, we assume a pressure balance between the inside and outside flux tube, $B^2/8\pi \sim p \propto e^{-x/H}$; then, $B \propto e^{-x/2H}$. Secondly, we assume a magnetic flux conservation $BS = \mathrm{const}$; then, $S \propto e^{x/2H}$. Finally, we assume energy conservation $FS = \mathrm{const}$, where F is the energy flux. Considering that a wave flux passing through the $x = 225 \, \mathrm{km}$ plane $F_{x=225 \, \mathrm{km}}$ is approximately $10^8 \, \mathrm{erg \, cm^{-2} \, s^{-1}}$, then a wave flux passing through the $x = 500 \, \mathrm{km}$ plane $F_{x=500 \, \mathrm{km}}$ can be estimated.

$$
\begin{aligned}
F_{x=500 \, \mathrm{km}} &\sim F_{x=225 \, \mathrm{km}} \times e^{(225 \, \mathrm{km} - 500 \, \mathrm{km})/2H} \\
&\sim 4 \times 10^7 \, \mathrm{erg \, cm^{-2} \, s^{-1}}
\end{aligned}
\tag{B.1}
$$

This value is approximately the energy flux required for heating the chromosphere in the active region $1.5 \times 10^7 \, \mathrm{erg \, cm^{-2} \, s^{-1}}$ and greater than $4 \times 10^6 \, \mathrm{erg \, cm^{-2} \, s^{-1}}$ in the quiet region (Withbroe & Noyes, 1977). Because these waves are high frequency, the transverse waves are easily converted to longitudinal waves by mode conversion, and the majority of these are dissipated in the chromosphere (Matsumoto & Shibata, 2010). Assuming the loop-like geometry found in the active regions, Antolin & Shibata (2010) found that active regions may not be heated by Alfvén waves, based on the expansion factor of the loop and other observed facts. Therefore, the waves released from the photospheric anemone jet-

time (1.57 s) density $(10^{-7}\ \mathrm{g\ cm^{-3}})$ velocity $(6.3\ \mathrm{km\ s^{-1}})$
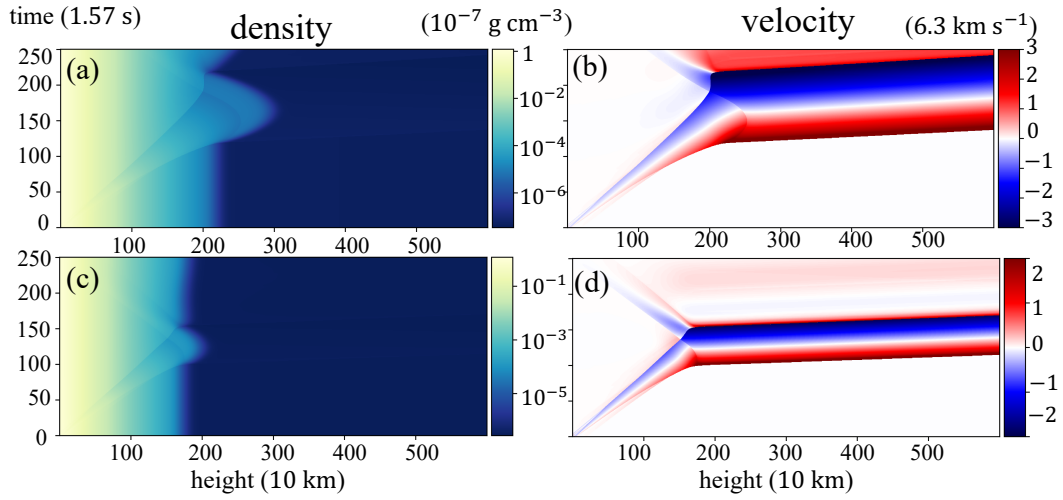
Figure B.1: Results of 1D simulation. (a), (c): time-height plot of density. (b), (d): time-height plot of velocity. (a), (b) and (c), (d) correspond to quiet region and active region cases.

height (10 km)

time (1.57 s)
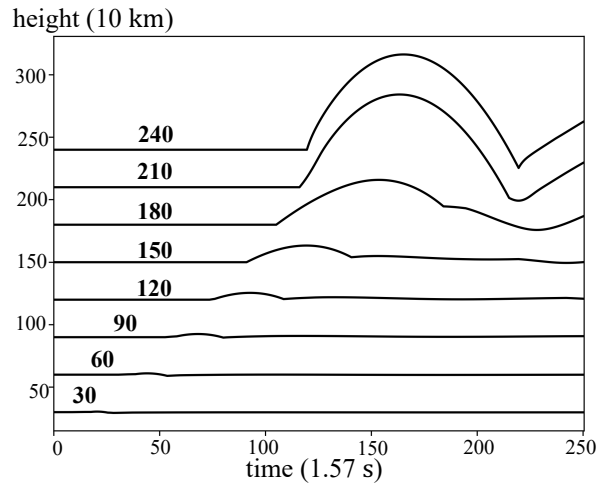
Figure B.2: Trajectories of the fluid particles in the case of the quiet region. The number above each curve indicates the initial position of each fluid particle.

like structure are expected to contribute mainly to the heating of the chromosphere. Note that we must consider the frequency of the jet-like structure to discuss the contribution to global chromospheric heating because these energy fluxes originate from a photospheric jet-like structure.

B.2   1D simulation for the spicule formation

To investigate how slow mode waves generated from the photospheric anemone jet-like structures propagate to the upper atmosphere along a vertical magnetic flux tube, we perform 1D non-magnetic hydrodynamic simulations.

For the numerical simulation, we use Athena++ code with the van Leer predictor-corrector scheme and Piecewise Linear Method (Stone et al., 2020). We solve the compressive hydrodynamic equation including uniform gravity. The basic equations are as follows.

$$\frac{\partial \rho}{\partial t} + \frac{\partial}{\partial s}(\rho v_\parallel) = 0 \tag{B.2}$$

$$\frac{\partial \rho v_\parallel}{\partial t} + \frac{\partial}{\partial s}(\rho v_\parallel^2) = -\frac{\partial}{\partial s}p + \rho g_\parallel \tag{B.3}$$

$$\frac{\partial}{\partial t}(e + \frac{1}{2}\rho v_\parallel^2) + \frac{\partial}{\partial s}[(h + \frac{1}{2}\rho v_\parallel^2)v_\parallel] = \rho g_\parallel v_\parallel$$

$$p = \frac{\rho R T}{\mu} \tag{B.4}$$

, where e is the internal fluid energy and $h = p + e$ is the enthalpy.

For the coordinates of the 1D calculation, a parallel straight line is taken in the background field of the 3D calculation. We set the height of the upper boundary as $12,000\,\mathrm{km}$ from the bottom of the photosphere. The number of the mesh is $24,000$, and the grid spacing is uniform. The normalization of the numerical calculation is performed in the same manner as the 3D calculation. We use only the background field component for the gravitational acceleration.

As the initial condition, we assume hydrostatic equilibrium with initial temperature T_{ini}.

$$T_{\mathrm{ini}} = T_{\mathrm{pho}} + \frac{1}{2}(T_{\mathrm{cor}} - T_{\mathrm{pho}})(1 + \tanh(\frac{x - x_{\mathrm{tr}}}{w_{\mathrm{tr}}})) \tag{B.5}$$

$T_{\mathrm{pho}}, T_{\mathrm{cor}}, x_{\mathrm{tr}}$, and w_{tr} are the temperature of the photosphere and corona, and the height and the thickness of the transition layer. We set $T_{\mathrm{pho}} = 6000\,\mathrm{K}, w_{\mathrm{tr}} = 80\,\mathrm{km}$. Then, along a reconnected field line in 3D simulation, we take out the thermodynamic quantity and velocity components parallel to the field and consider them as a perturbation. For the parameters T_{cor} and x_{tr}, we perform two cases, $T_{\mathrm{cor}} = 170 T_{\mathrm{pho}} = 1.02 \times 10^6\,\mathrm{K}, x_{\mathrm{tr}} = 2300\,\mathrm{km}$ (quiet region case) and $T_{\mathrm{cor}} = 400 T_{\mathrm{pho}} = 2.4 \times 10^6\,\mathrm{K}, x_{\mathrm{tr}} = 1850\,\mathrm{km}$ (active region case). The coronal pressure in the initial condition is a approximate agreement with the values reported in the observations (quiet region: Ito et al. (2010), active region: Winebarger et al. (2011)).

For the boundary condition, we set the reflected boundary at the bottom and open boundary at the top. Note that in order to maintain the hydrostatic pressure equilibrium

at the upper boundary, we set the gravitational acceleration to zero smoothly above the height of $11,000\,\mathrm{km}$. This height is sufficiently greater than that at which the contact discontinuity surface obtained from the calculation results rises, and thus this assumption does not substantially influence the calculation.

Figure B.1 displays the results. We can observe that the contact discontinuity is launched by shocks. Figures B.1a and B.1b display the quiet region case, and we can observe that the maximum height is approximately $3200\,\mathrm{km}$, the maximum velocity is approximately $20\,\mathrm{km\,s^{-1}}$, and the lifetime is approximately $160\,\mathrm{s}$. Pereira et al. (2012) and Zhang et al. (2012) performed a statistical study of spicules, and many of their results are consistent with our simulation. Figures B.1c and B.1d display the active region case. We can observe that the maximum height is approximately $2100\,\mathrm{km}$ (the maximum length is approximately $300\,\mathrm{km}$), the maximum velocity is approximately $15\,\mathrm{km\,s^{-1}}$, and the lifetime is approximately $100\,\mathrm{s}$. De Pontieu et al. (2007a) and Anan et al. (2010) performed statistical studies of dynamic fibrils. Their studies are consistent with our results regarding the maximum length and the maximum velocity. The maximum length and lifetime in our results are marginally shorter than their study, yet reasonably consistent with theirs. These results suggest that photospheric anemone jet-like structures can be one of the origins of spicules and dynamic fibrils.

Figure B.2 displays the trajectories of the fluid particles. From this figure, we can observe that the fluid particles do not move to a great degree in the lower layer, yet near the transition region, they are significantly launched by the shock to form a jet. Note that the behavior of the fluid particles in the lower layers in this figure is similar to that of those observable in figure 4.9. This is consistent with the result that the photospheric anemone jet-like structure is not a plasma flow.

Bibliography

Aarnio, A. N., Stassun, K. G., Hughes, W. J., & McGregor, S. L. 2011, SoPh, 268, 195, doi: 10.1007/s11207-010-9672-7

Alvarado-Gómez, J. D., Drake, J. J., Cohen, O., Moschou, S. P., & Garraffo, C. 2018, ApJ, 862, 93, doi: 10.3847/1538-4357/aacb7f

Anan, T., Kitai, R., Kawate, T., et al. 2010, PASJ, 62, 871, doi: 10.1093/pasj/62.4.871

Antolin, P., Pagano, P., Testa, P., Petralia, A., & Reale, F. 2021, Nature Astronomy, 5, 54, doi: 10.1038/s41550-020-1199-8

Antolin, P., & Shibata, K. 2010, ApJ, 712, 494, doi: 10.1088/0004-637X/712/1/494

Antolin, P., Shibata, K., Kudoh, T., Shiota, D., & Brooks, D. 2008, ApJ, 688, 669, doi: 10.1086/591998

Archontis, V., & Hood, A. W. 2013, ApJL, 769, L21, doi: 10.1088/2041-8205/769/2/L21

Argiroffi, C., Reale, F., Drake, J. J., et al. 2019, Nature Astronomy, 3, 742, doi: 10.1038/s41550-019-0781-4

Asai, A., Ishii, T. T., Kurokawa, H., Yokoyama, T., & Shimojo, M. 2003, ApJ, 586, 624, doi: 10.1086/367694

Aschwanden, M. J. 2002, SSRv, 101, 1, doi: 10.1023/A:1019712124366

—. 2016, ApJ, 831, 105, doi: 10.3847/0004-637X/831/1/105

—. 2020, ApJ, 903, 23, doi: 10.3847/1538-4357/abb946

Aschwanden, M. J., Stern, R. A., & Güdel, M. 2008, ApJ, 672, 659, doi: 10.1086/523926

Aschwanden, M. J., Tarbell, T. D., Nightingale, R. W., et al. 2000, ApJ, 535, 1047, doi: 10.1086/308867

Ashfield, W. H., & Longcope, D. W. 2021, ApJ, 912, 25, doi: 10.3847/1538-4357/abedb4

Athay, R. G. 1976, The solar chromosphere and corona: Quiet sun, Vol. 53, doi: 10.1007/978-94-010-1715-2

Aurass, H., Klein, K. L., & Martens, P. C. H. 1994, SoPh, 155, 203, doi: 10.1007/BF00670741

Bakke, H., Carlsson, M., Rouppe van der Voort, L., et al. 2022, A&A, 659, A186, doi: 10.1051/0004-6361/202142842

Barnes, W. T., Cheung, M. C. M., Bobra, M. G., et al. 2020, Journal of Open Source Software, 5, 2801, doi: 10.21105/joss.02801

Battaglia, M., Fletcher, L., & Benz, A. O. 2009, A&A, 498, 891, doi: 10.1051/0004-6361/200811196

Beckers, J. M. 1964, PhD thesis, Sacramento Peak Observatory, Air Force Cambridge Research Laboratories, Mass., USA

—. 1972, ARA&A, 10, 73, doi: 10.1146/annurev.aa.10.090172.000445

Benz, A. O. 2017, Living Reviews in Solar Physics, 14, 2, doi: 10.1007/s41116-016-0004-3

Benz, A. O., & Krucker, S. 1999, A&A, 341, 286

—. 2002, ApJ, 568, 413, doi: 10.1086/338807

Berdyugina, S. V. 2005, Living Reviews in Solar Physics, 2, 8, doi: 10.12942/lrsp-2005-8

Berger, T. A., Huber, D., Gaidos, E., & van Saders, J. L. 2018, ApJ, 866, 99, doi: 10.3847/1538-4357/aada83

Berghmans, D., Clette, F., & Moses, D. 1998, A&A, 336, 1039

Berghmans, D., Auchère, F., Long, D. M., et al. 2021, A&A, 656, L4, doi: 10.1051/0004-6361/202140380

Bharti, L., Solanki, S. K., & Hirzberger, J. 2017, A&A, 597, A127, doi: `10.1051/0004-6361/201629656`

Brueckner, G. E., & Bartoe, J. D. F. 1983, ApJ, 272, 329, doi: `10.1086/161297`

Canfield, R. C., Penn, M. J., Wulser, J.-P., & Kiplinger, A. L. 1990, ApJ, 363, 318, doi: `10.1086/169345`

Carmichael, H. 1964, A Process for Flares, Vol. 50, 451

Carrington, R. C. 1859, MNRAS, 20, 13, doi: `10.1093/mnras/20.1.13`

Casini, R., Bevilacqua, R., & López Ariste, A. 2005, ApJ, 622, 1265, doi: `10.1086/428283`

Casini, R., López Ariste, A., Tomczyk, S., & Lites, B. W. 2003, ApJL, 598, L67, doi: `10.1086/380496`

Chae, J., Yun, H. S., & Poland, A. I. 1998, ApJS, 114, 151, doi: `10.1086/313064`

Chen, H., Hong, J., Yang, B., Xu, Z., & Yang, J. 2020, ApJ, 902, 8, doi: `10.3847/1538-4357/abb1c1`

Chen, Y., Przybylski, D., Peter, H., et al. 2021, A&A, 656, L7, doi: `10.1051/0004-6361/202140638`

Chitta, L. P., Peter, H., & Young, P. R. 2021a, A&A, 647, A159, doi: `10.1051/0004-6361/202039969`

Chitta, L. P., Peter, H., Solanki, S. K., et al. 2017, ApJS, 229, 4, doi: `10.3847/1538-4365/229/1/4`

Chitta, L. P., Solanki, S. K., Peter, H., et al. 2021b, A&A, 656, L13, doi: `10.1051/0004-6361/202141683`

Christe, S., Glesener, L., Buitrago-Casas, C., et al. 2016, Journal of Astronomical Instrumentation, 5, 1640005, doi: `10.1142/S2251171716400055`

Christian, D. J., Jess, D. B., Antolin, P., & Mathioudakis, M. 2015, ApJ, 804, 147, doi: `10.1088/0004-637X/804/2/147`

Cirtain, J. W., Golub, L., Winebarger, A. R., et al. 2013, Nature, 493, 501, doi: `10.1038/nature11772`

Cliver, E. W., Schrijver, C. J., Shibata, K., & Usoskin, I. G. 2022, Living Reviews in Solar Physics, 19, 2, doi: `10.1007/s41116-022-00033-8`

Czaykowska, A., Alexander, D., & De Pontieu, B. 2001, ApJ, 552, 849, doi: 10.1086/320553

Danilovic, S. 2017, A&A, 601, A122, doi: 10.1051/0004-6361/201730403

De Pontieu, B., Erdélyi, R., & James, S. P. 2004, Nature, 430, 536, doi: 10.1038/nature02749

De Pontieu, B., Hansteen, V. H., Rouppe van der Voort, L., van Noort, M., & Carlsson, M. 2007a, ApJ, 655, 624, doi: 10.1086/509070

De Pontieu, B., McIntosh, S., Hansteen, V. H., et al. 2007b, PASJ, 59, S655, doi: 10.1093/pasj/59.sp3.S655

Drake, J. J., Cohen, O., Yashiro, S., & Gopalswamy, N. 2013, ApJ, 764, 170, doi: 10.1088/0004-637X/764/2/170

Edlén, B. 1943, ZA, 22, 30

Ellerman, F. 1917, ApJ, 46, 298, doi: 10.1086/142366

Emslie, A. G., & Sturrock, P. A. 1982, SoPh, 80, 99, doi: 10.1007/BF00153426

Emslie, A. G., Dennis, B. R., Shih, A. Y., et al. 2012, ApJ, 759, 71, doi: 10.1088/0004-637X/759/1/71

Fang, F., Fan, Y., & McIntosh, S. W. 2014, ApJL, 789, L19, doi: 10.1088/2041-8205/789/1/L19

Feldman, U., Laming, J. M., & Doschek, G. A. 1995, ApJL, 451, L79, doi: 10.1086/309695

Fisher, G. H. 1989, ApJ, 346, 1019, doi: 10.1086/168084

Fisher, G. H., Canfield, R. C., & McClymont, A. N. 1985, ApJ, 289, 434, doi: 10.1086/162903

Galsgaard, K., Madjarska, M. S., Mackay, D. H., & Mou, C. 2019, A&A, 623, A78, doi: 10.1051/0004-6361/201834329

Gary, G. A. 2001, SoPh, 203, 71, doi: 10.1023/A:1012722021820

Georgoulis, M. K., Rust, D. M., Bernasconi, P. N., & Schmieder, B. 2002, ApJ, 575, 506, doi: 10.1086/341195

Glesener, L., Krucker, S., Christe, S., et al. 2016, in Society of Photo-Optical Instrumentation Engineers (SPIE) Conference Series, Vol. 9905, Space Telescopes and Instrumentation 2016: Ultraviolet to Gamma Ray, ed. J.-W. A. den Herder, T. Takahashi, & M. Bautz, 99050E, doi: 10.1117/12.2232262

Gopalswamy, N., Shimojo, M., Lu, W., et al. 2003, ApJ, 586, 562, doi: 10.1086/367614

Güdel, M. 2004, A&A Rv, 12, 71, doi: 10.1007/s00159-004-0023-2

Hanaoka, Y., & Sakurai, T. 2017, ApJ, 851, 130, doi: 10.3847/1538-4357/aa9cf1

Hanaoka, Y., Kurokawa, H., Enome, S., et al. 1994, PASJ, 46, 205

Hannah, I. G., Christe, S., Krucker, S., et al. 2008, ApJ, 677, 704, doi: 10.1086/529012

Hannah, I. G., Hudson, H. S., Battaglia, M., et al. 2011, SSRv, 159, 263, doi: 10.1007/s11214-010-9705-4

Hannah, I. G., & Kontar, E. P. 2012, A&A, 539, A146, doi: 10.1051/0004-6361/201117576

Harrison, F. A., Craig, W. W., Christensen, F. E., et al. 2013, ApJ, 770, 103, doi: 10.1088/0004-637X/770/2/103

He, J. S., Tu, C. Y., Marsch, E., et al. 2009, A&A, 497, 525, doi: 10.1051/0004-6361/200810777

Hermans, L. M., & Martin, S. F. 1986, in NASA Conference Publication, Vol. 2442, NASA Conference Publication, 369–375

Hertzsprung, E. 1924, BAN, 2, 87

Hirayama, T. 1974, SoPh, 34, 323, doi: 10.1007/BF00153671

Hodgson, R. 1859, MNRAS, 20, 15, doi: 10.1093/mnras/20.1.15

Hollweg, J. V., Jackson, S., & Galloway, D. 1982, SoPh, 75, 35, doi: 10.1007/BF00153458

Honda, S., Notsu, Y., Namekata, K., et al. 2018, PASJ, 70, 62, doi: 10.1093/pasj/psy055

Houdebine, E. R., Foing, B. H., & Rodono, M. 1990, A&A, 238, 249

Hudson, H. S. 1991, SoPh, 133, 357, doi: 10.1007/BF00149894

Ichimoto, K., & Kurokawa, H. 1984, SoPh, 93, 105, doi: `10.1007/BF00156656`

Ichimoto, K., Ishii, T. T., Otsuji, K., et al. 2017, SoPh, 292, 63, doi: `10.1007/s11207-017-1082-7`

Iijima, H., & Yokoyama, T. 2015, ApJL, 812, L30, doi: `10.1088/2041-8205/812/2/L30`

Innes, D. E., Genetelli, A., Attie, R., & Potts, H. E. 2009, A&A, 495, 319, doi: `10.1051/0004-6361:200811011`

Inoue, S., Hayashi, K., Magara, T., Choe, G. S., & Park, Y. D. 2014, ApJ, 788, 182, doi: `10.1088/0004-637X/788/2/182`

Ishikawa, S.-n., Glesener, L., Krucker, S., et al. 2017, Nature Astronomy, 1, 771, doi: `10.1038/s41550-017-0269-z`

Isobe, H., Tripathi, D., & Archontis, V. 2007, ApJL, 657, L53, doi: `10.1086/512969`

Ito, H., Tsuneta, S., Shiota, D., Tokumaru, M., & Fujiki, K. 2010, ApJ, 719, 131, doi: `10.1088/0004-637X/719/1/131`

Jain, R., & Sorathia, B. 1987, Journal of Astrophysics and Astronomy, 8, 295, doi: `10.1007/BF02714894`

Jakimiec, J., Sylwester, B., Sylwester, J., et al. 1992, A&A, 253, 269

Jiang, C., Feng, X., Wu, S. T., & Hu, Q. 2013, ApJL, 771, L30, doi: `10.1088/2041-8205/771/2/L30`

Jin, C. L., Zhou, G. P., & Wang, J. X. 2021, ApJL, 914, L35, doi: `10.3847/2041-8213/ac097c`

Jing, J., Liu, C., Lee, J., et al. 2018, ApJ, 864, 138, doi: `10.3847/1538-4357/aad6e4`

Joshi, J., Rouppe van der Voort, L. H. M., & de la Cruz Rodríguez, J. 2020, A&A, 641, L5, doi: `10.1051/0004-6361/202038769`

Joulin, V., Buchlin, E., Solomon, J., & Guennou, C. 2016, A&A, 591, A148, doi: `10.1051/0004-6361/201526254`

Kamio, S., Curdt, W., Teriaca, L., & Innes, D. E. 2011, A&A, 529, A21, doi: `10.1051/0004-6361/201015715`

Kane, S. R. 1974, in Coronal Disturbances, ed. G. A. Newkirk, Vol. 57, 105

Kigure, H., Takahashi, K., Shibata, K., Yokoyama, T., & Nozawa, S. 2010, PASJ, 62, 993, doi: 10.1093/pasj/62.4.993

Kippenhahn, R., & Schlüter, A. 1957, ZA, 43, 36

Kitai, R. 1983, SoPh, 87, 135, doi: 10.1007/BF00151165

Koch, D. G., Borucki, W. J., Basri, G., et al. 2010, ApJL, 713, L79, doi: 10.1088/2041-8205/713/2/L79

Kontogiannis, I., Dineva, E., Diercke, A., et al. 2020, ApJ, 898, 144, doi: 10.3847/1538-4357/aba117

Kopp, R. A., & Pneuman, G. W. 1976, SoPh, 50, 85, doi: 10.1007/BF00206193

Kosugi, T., Matsuzaki, K., Sakao, T., et al. 2007, SoPh, 243, 3, doi: 10.1007/s11207-007-9014-6

Kotani, Y., Ishii, T. T., Yamasaki, D., et al. 2022, submitted

Kotani, Y., & Shibata, K. 2020, PASJ, 72, 75, doi: 10.1093/pasj/psaa064

Kotani, Y., Shibata, K., Ishii, T. T., et al. 2022, arXiv e-prints, arXiv:2212.08850. https://arxiv.org/abs/2212.08850

Koyama, K., Hamaguchi, K., Ueno, S., Kobayashi, N., & Feigelson, E. D. 1996, PASJ, 48, L87, doi: 10.1093/pasj/48.5.L87

Kretzschmar, M. 2011, A&A, 530, A84, doi: 10.1051/0004-6361/201015930

Krucker, S., & Benz, A. O. 1998, ApJL, 501, L213, doi: 10.1086/311474

Krucker, S., Benz, A. O., Bastian, T. S., & Acton, L. W. 1997, ApJ, 488, 499, doi: 10.1086/304686

Krucker, S., Christe, S., Lin, R. P., Hurford, G. J., & Schwartz, R. A. 2002, SoPh, 210, 445, doi: 10.1023/A:1022404512780

Kruskal, M., & Schwarzschild, M. 1954, Proceedings of the Royal Society of London Series A, 223, 348, doi: 10.1098/rspa.1954.0120

Kuckein, C., Centeno, R., Martínez Pillet, V., et al. 2009, A&A, 501, 1113, doi: 10.1051/0004-6361/200911800

Kudoh, T., & Shibata, K. 1999, ApJ, 514, 493, doi: 10.1086/306930

Kuhar, M., Krucker, S., Glesener, L., et al. 2018, ApJL, 856, L32, doi: 10.3847/2041-8213/aab889

Kulander, J. L., & Jefferies, J. T. 1966, ApJ, 146, 194, doi: 10.1086/148868

Kumar, P., Karpen, J. T., Antiochos, S. K., Wyper, P. F., & DeVore, C. R. 2019, ApJL, 885, L15, doi: 10.3847/2041-8213/ab45f9

Kundu, M. R., Raulin, J. P., Nitta, N., et al. 1995, ApJL, 447, L135, doi: 10.1086/309567

Kuniyoshi, H., Yokoyama, T., & Iijima, H. 2021, in AGU Fall Meeting Abstracts, Vol. 2021, SH12B–08

Kurita, M., Kino, M., Iwamuro, F., et al. 2020, PASJ, 72, 48, doi: 10.1093/pasj/psaa036

Labonte, B. J. 1979, SoPh, 61, 283, doi: 10.1007/BF00150413

Labrosse, N., Heinzel, P., Vial, J. C., et al. 2010, SSRv, 151, 243, doi: 10.1007/s11214-010-9630-6

Landi, E., Young, P. R., Dere, K. P., Del Zanna, G., & Mason, H. E. 2013, ApJ, 763, 86, doi: 10.1088/0004-637X/763/2/86

Leake, J. E., & Arber, T. D. 2006, A&A, 450, 805, doi: 10.1051/0004-6361:20054099

Lee, E. J., Archontis, V., & Hood, A. W. 2015, ApJL, 798, L10, doi: 10.1088/2041-8205/798/1/L10

Leitzinger, M., Odert, P., & Heinzel, P. 2022, MNRAS, 513, 6058, doi: 10.1093/mnras/stac1284

Lemen, J. R., Title, A. M., Akin, D. J., et al. 2012, SoPh, 275, 17, doi: 10.1007/s11207-011-9776-8

Lin, R. P., Schwartz, R. A., Kane, S. R., Pelling, R. M., & Hurley, K. C. 1984, ApJ, 283, 421, doi: 10.1086/162321

Lin, R. P., Dennis, B. R., Hurford, G. J., et al. 2002, SoPh, 210, 3, doi: 10.1023/A:1022428818870

Liu, C., Qiu, J., Gary, D. E., Krucker, S., & Wang, H. 2004, ApJ, 604, 442, doi: 10.1086/381799

Longcope, D. W. 2014, ApJ, 795, 10, doi: 10.1088/0004-637X/795/1/10

Mackay, D. H., Karpen, J. T., Ballester, J. L., Schmieder, B., & Aulanier, G. 2010, SSRv, 151, 333, doi: 10.1007/s11214-010-9628-0

Madjarska, M. S. 2019, Living Reviews in Solar Physics, 16, 2, doi: 10.1007/s41116-019-0018-8

Madjarska, M. S., Galsgaard, K., Mackay, D. H., Koleva, K., & Dechev, M. 2020, A&A, 643, A19, doi: 10.1051/0004-6361/202038287

Madjarska, M. S., Mackay, D. H., Galsgaard, K., Wiegelmann, T., & Xie, H. 2022, A&A, 660, A45, doi: 10.1051/0004-6361/202142439

Maehara, H., Shibayama, T., Notsu, Y., et al. 2015, Earth, Planets and Space, 67, 59, doi: 10.1186/s40623-015-0217-z

Maehara, H., Shibayama, T., Notsu, S., et al. 2012, Nature, 485, 478, doi: 10.1038/nature11063

Maehara, H., Notsu, Y., Namekata, K., et al. 2021, PASJ, 73, 44, doi: 10.1093/pasj/psaa098

Maltby, P., Avrett, E. H., Carlsson, M., et al. 1986, ApJ, 306, 284, doi: 10.1086/164342

Masuda, S., Kosugi, T., Hara, H., Tsuneta, S., & Ogawara, Y. 1994, Nature, 371, 495, doi: 10.1038/371495a0

Masuda, S., Kosugi, T., & Hudson, H. S. 2001, SoPh, 204, 55, doi: 10.1023/A:1014230629731

Matsumoto, T., & Shibata, K. 2010, ApJ, 710, 1857, doi: 10.1088/0004-637X/710/2/1857

McAllister, A., Uchida, Y., Tsuneta, S., et al. 1992, PASJ, 44, L205

McAllister, A. H., Dryer, M., McIntosh, P., Singer, H., & Weiss, L. 1996, J. Geophys. Res., 101, 13497, doi: 10.1029/96JA00510

Mein, P., & Mein, N. 1988, A&A, 203, 162

Mierla, M., Zhukov, A. N., Berghmans, D., et al. 2022, A&A, 662, L5, doi: 10.1051/0004-6361/202244020

Miyagoshi, T., & Yokoyama, T. 2004, ApJ, 614, 1042, doi: 10.1086/423731

Moore, R. L., Tang, F., Bohlin, J. D., & Golub, L. 1977, ApJ, 218, 286, doi: 10.1086/155681

Moraitis, K., Tziotziou, K., Georgoulis, M. K., & Archontis, V. 2014, SoPh, 289, 4453, doi: 10.1007/s11207-014-0590-y

Moreno-Insertis, F., & Galsgaard, K. 2013, ApJ, 771, 20, doi: 10.1088/0004-637X/771/1/20

Moreno-Insertis, F., Galsgaard, K., & Ugarte-Urra, I. 2008, ApJL, 673, L211, doi: 10.1086/527560

Moriyasu, S., Kudoh, T., Yokoyama, T., & Shibata, K. 2004, ApJL, 601, L107, doi: 10.1086/381779

Moschou, S.-P., Drake, J. J., Cohen, O., et al. 2019, ApJ, 877, 105, doi: 10.3847/1538-4357/ab1b37

Müller, D., St. Cyr, O. C., Zouganelis, I., et al. 2020, A&A, 642, A1, doi: 10.1051/0004-6361/202038467

Nagai, F. 1980, SoPh, 68, 351, doi: 10.1007/BF00156874

Namekata, K., Ichimoto, K., Ishii, T. T., & Shibata, K. 2022a, ApJ, 933, 209, doi: 10.3847/1538-4357/ac75cd

Namekata, K., Sakaue, T., Watanabe, K., Asai, A., & Shibata, K. 2017a, PASJ, 69, 7, doi: 10.1093/pasj/psw111

Namekata, K., Sakaue, T., Watanabe, K., et al. 2017b, ApJ, 851, 91, doi: 10.3847/1538-4357/aa9b34

Namekata, K., Maehara, H., Notsu, Y., et al. 2019, ApJ, 871, 187, doi: 10.3847/1538-4357/aaf471

Namekata, K., Davenport, J. R. A., Morris, B. M., et al. 2020, ApJ, 891, 103, doi: 10.3847/1538-4357/ab7384

Namekata, K., Maehara, H., Honda, S., et al. 2022b, Nature Astronomy, 6, 241, doi: 10.1038/s41550-021-01532-8

Nelson, C. J., Doyle, J. G., Erdélyi, R., et al. 2013, SoPh, 283, 307, doi: 10.1007/s11207-012-0222-3

Nelson, C. J., Freij, N., Bennett, S., Erdélyi, R., & Mathioudakis, M. 2019, ApJ, 883, 115, doi: 10.3847/1538-4357/ab3a54

Neupert, W. M. 1968, ApJL, 153, L59, doi: 10.1086/180220

Nishizuka, N., Nakamura, T., Kawate, T., Singh, K. A. P., & Shibata, K. 2011, ApJ, 731, 43, doi: 10.1088/0004-637X/731/1/43

Nishizuka, N., Shimizu, M., Nakamura, T., et al. 2008, ApJL, 683, L83, doi: `10.1086/591445`

Nisticò, G., Bothmer, V., Patsourakos, S., & Zimbardo, G. 2009, SoPh, 259, 87, doi: `10.1007/s11207-009-9424-8`

Notsu, Y., Maehara, H., Honda, S., et al. 2019, ApJ, 876, 58, doi: `10.3847/1538-4357/ab14e6`

Ogawara, Y., Takano, T., Kato, T., et al. 1991, SoPh, 136, 1, doi: `10.1007/BF00151692`

Ohyama, M., & Shibata, K. 1998, ApJ, 499, 934, doi: `10.1086/305652`

Ohyama, M., & Shibata, K. 1999, in Proceedings of the Nobeyama Symposium, ed. T. S. Bastian, N. Gopalswamy, & K. Shibasaki, 367–370

Okamoto, S., Notsu, Y., Maehara, H., et al. 2021, ApJ, 906, 72, doi: `10.3847/1538-4357/abc8f5`

Okamoto, T. J., & De Pontieu, B. 2011, ApJL, 736, L24, doi: `10.1088/2041-8205/736/2/L24`

Otsu, T., Asai, A., Ichimoto, K., Ishii, T. T., & Namekata, K. 2022, ApJ, 939, 98, doi: `10.3847/1538-4357/ac9730`

Panesar, N. K., Hansteen, V. H., Tiwari, S. K., et al. 2022a, arXiv e-prints, arXiv:2211.06529. `https://arxiv.org/abs/2211.06529`

Panesar, N. K., Tiwari, S. K., Berghmans, D., et al. 2021, ApJL, 921, L20, doi: `10.3847/2041-8213/ac3007`

Panesar, N. K., Tiwari, S. K., Moore, R. L., Sterling, A. C., & De Pontieu, B. 2022b, ApJ, 939, 25, doi: `10.3847/1538-4357/ac8d65`

Parenti, S. 2014, Living Reviews in Solar Physics, 11, 1, doi: `10.12942/lrsp-2014-1`

Pariat, E., Antiochos, S. K., & DeVore, C. R. 2009, ApJ, 691, 61, doi: `10.1088/0004-637X/691/1/61`

Pariat, E., Aulanier, G., Schmieder, B., et al. 2004, ApJ, 614, 1099, doi: `10.1086/423891`

Pariat, E., Dalmasse, K., DeVore, C. R., Antiochos, S. K., & Karpen, J. T. 2015, A&A, 573, A130, doi: `10.1051/0004-6361/201424209`

—. 2016, A&A, 596, A36, doi: `10.1051/0004-6361/201629109`

Parker, E. N. 1988, ApJ, 330, 474, doi: `10.1086/166485`

—. 1991, ApJ, 372, 719, doi: `10.1086/170015`

Parnell, C. E., & Jupp, P. E. 2000, ApJ, 529, 554, doi: `10.1086/308271`

Pereira, T. M. D., De Pontieu, B., & Carlsson, M. 2012, ApJ, 759, 18, doi: `10.1088/0004-637X/759/1/18`

Pesnell, W. D., Thompson, B. J., & Chamberlin, P. C. 2012, SoPh, 275, 3, doi: `10.1007/s11207-011-9841-3`

Petschek, H. E. 1964, in NASA Special Publication, Vol. 50, 425

Podladchikova, O., Vourlidas, A., Van der Linden, R. A. M., Wülser, J. P., & Patsourakos, S. 2010, ApJ, 709, 369, doi: `10.1088/0004-637X/709/1/369`

Priest, E. 2014, Magnetohydrodynamics of the Sun, doi: `10.1017/CBO9781139020732`

Purkhart, S., & Veronig, A. M. 2022, A&A, 661, A149, doi: `10.1051/0004-6361/202243234`

Raassen, A. J. J., Mitra-Kraev, U., & Güdel, M. 2007, MNRAS, 379, 1075, doi: `10.1111/j.1365-2966.2007.11983.x`

Reale, F. 2007, A&A, 471, 271, doi: `10.1051/0004-6361:20077223`

—. 2014, Living Reviews in Solar Physics, 11, 4, doi: `10.12942/lrsp-2014-4`

Rempel, M. 2017, ApJ, 834, 10, doi: `10.3847/1538-4357/834/1/10`

Ren, D. B., Jiang, Y. C., Yang, J. Y., et al. 2008, Ap&SS, 318, 141, doi: `10.1007/s10509-008-9908-2`

Rimmele, T. R., Warner, M., Keil, S. L., et al. 2020, SoPh, 295, 172, doi: `10.1007/s11207-020-01736-7`

Rochus, P., Auchère, F., Berghmans, D., et al. 2020, A&A, 642, A8, doi: `10.1051/0004-6361/201936663`

Rosner, R., Tucker, W. H., & Vaiana, G. S. 1978, ApJ, 220, 643, doi: `10.1086/155949`

Rouppe van der Voort, L. H. M., Rutten, R. J., & Vissers, G. J. M. 2016, A&A, 592, A100, doi: `10.1051/0004-6361/201628889`

Sakajiri, T., Brooks, D. H., Yamamoto, T., et al. 2004, ApJ, 616, 578, doi: `10.1086/424823`

Sakaue, T., & Shibata, K. 2021, ApJ, 919, 29, doi: `10.3847/1538-4357/ac0e34`

Sako, N., et al. 2014

Samanta, T., Tian, H., Yurchyshyn, V., et al. 2019, Science, 366, 890, doi: `10.1126/science.aaw2796`

Sasso, C., Lagg, A., & Solanki, S. K. 2011, A&A, 526, A42, doi: `10.1051/0004-6361/200912956`

Schadee, A., de Jager, C., & Svestka, Z. 1983, SoPh, 89, 287, doi: `10.1007/BF00217252`

Scharmer, G. B., Bjelksjo, K., Korhonen, T. K., Lindberg, B., & Petterson, B. 2003, in Society of Photo-Optical Instrumentation Engineers (SPIE) Conference Series, Vol. 4853, Innovative Telescopes and Instrumentation for Solar Astrophysics, ed. S. L. Keil & S. V. Avakyan, 341–350, doi: `10.1117/12.460377`

Scharmer, G. B., Narayan, G., Hillberg, T., et al. 2008, ApJL, 689, L69, doi: `10.1086/595744`

Scherrer, P. H., Schou, J., Bush, R. I., et al. 2012, SoPh, 275, 207, doi: `10.1007/s11207-011-9834-2`

Schrijver, C. J. 2010, ApJ, 710, 1480, doi: `10.1088/0004-637X/710/2/1480`

Schwarzschild, M. 1948, ApJ, 107, 1, doi: `10.1086/144983`

Secchi, A. 1875, Le Soleil, doi: `10.3931/e-rara-14748`

See, V., Jardine, M., Vidotto, A. A., et al. 2017, MNRAS, 466, 1542, doi: `10.1093/mnras/stw3094`

Seki, D., Otsuji, K., Ishii, T., et al. 2019, Sun and Geosphere, 14, 95, doi: `10.31401/SunGeo.2019.02.01`

Serio, S., Reale, F., Jakimiec, J., Sylwester, B., & Sylwester, J. 1991, A&A, 241, 197

Shibata, K. 1997, in ESA Special Publication, Vol. 404, Fifth SOHO Workshop: The Corona and Solar Wind Near Minimum Activity, ed. A. Wilson, 103

Shibata, K. 1999, Ap&SS, 264, 129, doi: `10.1023/A:1002413214356`

Shibata, K., & Magara, T. 2011, Living Reviews in Solar Physics, 8, 6, doi: 10.12942/lrsp-2011-6

Shibata, K., Masuda, S., Shimojo, M., et al. 1995, ApJL, 451, L83, doi: 10.1086/309688

Shibata, K., Nitta, N., Strong, K. T., et al. 1994, ApJL, 431, L51, doi: 10.1086/187470

Shibata, K., & Uchida, Y. 1985, PASJ, 37, 31

—. 1986, SoPh, 103, 299, doi: 10.1007/BF00147831

Shibata, K., & Yokoyama, T. 1999, ApJL, 526, L49, doi: 10.1086/312354

—. 2002, ApJ, 577, 422, doi: 10.1086/342141

Shibata, K., Ishido, Y., Acton, L. W., et al. 1992, PASJ, 44, L173

Shibata, K., Nakamura, T., Matsumoto, T., et al. 2007, Science, 318, 1591, doi: 10.1126/science.1146708

Shibata, K., Isobe, H., Hillier, A., et al. 2013, PASJ, 65, 49, doi: 10.1093/pasj/65.3.49

Shibayama, T., Maehara, H., Notsu, S., et al. 2013, ApJS, 209, 5, doi: 10.1088/0067-0049/209/1/5

Shimizu, T. 1995, PASJ, 47, 251

Shimojo, M., Hashimoto, S., Shibata, K., et al. 1996, PASJ, 48, 123, doi: 10.1093/pasj/48.1.123

Shimojo, M., & Shibata, K. 2000, ApJ, 542, 1100, doi: 10.1086/317024

Shimojo, M., Shibata, K., & Harvey, K. L. 1998, SoPh, 178, 379, doi: 10.1023/A:1005091905214

Shimojo, M., Shibata, K., Yokoyama, T., & Hori, K. 2001, ApJ, 550, 1051, doi: 10.1086/319788

Shoda, M., & Yokoyama, T. 2018, ApJ, 854, 9, doi: 10.3847/1538-4357/aaa54f

Singh, K. A. P., Shibata, K., Nishizuka, N., & Isobe, H. 2011, Physics of Plasmas, 18, 111210, doi: 10.1063/1.3655444

Sterling, A. C., Harra, L. K., Moore, R. L., & Falconer, D. A. 2019, ApJ, 871, 220, doi: 10.3847/1538-4357/aaf1d3

Sterling, A. C., & Moore, R. L. 2016, ApJL, 828, L9, doi: `10.3847/2041-8205/828/1/L9`

Sterling, A. C., Moore, R. L., Falconer, D. A., & Adams, M. 2015, Nature, 523, 437, doi: `10.1038/nature14556`

Stone, J. M., Tomida, K., White, C. J., & Felker, K. G. 2020, ApJS, 249, 4, doi: `10.3847/1538-4365/ab929b`

Strassmeier, K. G. 2009, A&A Rv, 17, 251, doi: `10.1007/s00159-009-0020-6`

Sturrock, P. A. 1966, Nature, 211, 695, doi: `10.1038/211695a0`

Suematsu, Y. 1990, in Progress of Seismology of the Sun and Stars, ed. Y. Osaki & H. Shibahashi, Vol. 367, 211, doi: `10.1007/3-540-53091-6_83`

Suematsu, Y., Shibata, K., Neshikawa, T., & Kitai, R. 1982, SoPh, 75, 99, doi: `10.1007/BF00153464`

Sun, X., Török, T., & DeRosa, M. L. 2022, MNRAS, 509, 5075, doi: `10.1093/mnras/stab3249`

Svestka, Z. 1976, Solar Flares

Sylwester, B., Sylwester, J., Serio, S., et al. 1993, A&A, 267, 586

Syrovatskii, S. I., & Shmeleva, O. P. 1972, Soviet Ast., 16, 273

Takahashi, T., Mizuno, Y., & Shibata, K. 2016, ApJL, 833, L8, doi: `10.3847/2041-8205/833/1/L8`

Takasao, S., Asai, A., Isobe, H., & Shibata, K. 2012, ApJL, 745, L6, doi: `10.1088/2041-8205/745/1/L6`

Takasao, S., Isobe, H., & Shibata, K. 2013, PASJ, 65, 62, doi: `10.1093/pasj/65.3.62`

Tei, A., Sakaue, T., Okamoto, T. J., et al. 2018, PASJ, 70, 100, doi: `10.1093/pasj/psy047`

Tian, H., Yurchyshyn, V., Peter, H., et al. 2018, ApJ, 854, 92, doi: `10.3847/1538-4357/aaa89d`

Tiwari, S. K., Hansteen, V. H., De Pontieu, B., Panesar, N. K., & Berghmans, D. 2022, ApJ, 929, 103, doi: `10.3847/1538-4357/ac5d46`

Török, T., Aulanier, G., Schmieder, B., Reeves, K. K., & Golub, L. 2009, ApJ, 704, 485, doi: 10.1088/0004-637X/704/1/485

Tousey, R. 1973, in Space Research Conference, Vol. 2, 713–730

Tsiropoula, G., & Schmieder, B. 1997, A&A, 324, 1183

Tsuboi, Y., Koyama, K., Murakami, H., et al. 1998, ApJ, 503, 894, doi: 10.1086/306024

Tsuneta, S. 1996, ApJ, 456, 840, doi: 10.1086/176701

Tsuneta, S., Hara, H., Shimizu, T., et al. 1992a, PASJ, 44, L63

Tsuneta, S., Takahashi, T., Acton, L. W., et al. 1992b, PASJ, 44, L211

Tsuneta, S., Acton, L., Bruner, M., et al. 1991, SoPh, 136, 37, doi: 10.1007/BF00151694

Tsuneta, S., Ichimoto, K., Katsukawa, Y., et al. 2008, SoPh, 249, 167, doi: 10.1007/s11207-008-9174-z

UeNo, S., Nagata, S.-i., Kitai, R., Kurokawa, H., & Ichimoto, K. 2004, in Society of Photo-Optical Instrumentation Engineers (SPIE) Conference Series, Vol. 5492, Ground-based Instrumentation for Astronomy, ed. A. F. M. Moorwood & M. Iye, 958–969, doi: 10.1117/12.550304

Veronig, A., Temmer, M., Hanslmeier, A., Otruba, W., & Messerotti, M. 2002, A&A, 382, 1070, doi: 10.1051/0004-6361:20011694

Veronig, A. M., Odert, P., Leitzinger, M., et al. 2021, Nature Astronomy, 5, 697, doi: 10.1038/s41550-021-01345-9

Vida, K., Leitzinger, M., Kriskovics, L., et al. 2019, A&A, 623, A49, doi: 10.1051/0004-6361/201834264

Vida, K., Kriskovics, L., Oláh, K., et al. 2016, A&A, 590, A11, doi: 10.1051/0004-6361/201527925

Vievering, J. T., Glesener, L., Athiray, P. S., et al. 2021, ApJ, 913, 15, doi: 10.3847/1538-4357/abf145

Švestka, Z., Kopecký, M., & Blaha, M. 1962, Bulletin of the Astronomical Institutes of Czechoslovakia, 13, 37

Wang, Y., & Yokoyama, T. 2020, ApJ, 891, 110, doi: 10.3847/1538-4357/ab70b2

Warmuth, A., & Mann, G. 2020, A&A, 644, A172, doi: `10.1051/0004-6361/202039529`

Watanabe, H., Vissers, G., Kitai, R., Rouppe van der Voort, L., & Rutten, R. J. 2011, ApJ, 736, 71, doi: `10.1088/0004-637X/736/1/71`

Wiegelmann, T., & Sakurai, T. 2021, Living Reviews in Solar Physics, 18, 1, doi: `10.1007/s41116-020-00027-4`

Winebarger, A. R., Schmelz, J. T., Warren, H. P., Saar, S. H., & Kashyap, V. L. 2011, ApJ, 740, 2, doi: `10.1088/0004-637X/740/1/2`

Withbroe, G. L., & Noyes, R. W. 1977, ARA&A, 15, 363, doi: `10.1146/annurev.aa.15.090177.002051`

Wöger, F., Rimmele, T., Ferayorni, A., et al. 2021, SoPh, 296, 145, doi: `10.1007/s11207-021-01881-7`

Wyper, P. F., DeVore, C. R., & Antiochos, S. K. 2018, ApJ, 852, 98, doi: `10.3847/1538-4357/aa9ffc`

Xu, Z., Lagg, A., Solanki, S., & Liu, Y. 2012, ApJ, 749, 138, doi: `10.1088/0004-637X/749/2/138`

Yadav, R., de la Cruz Rodríguez, J., Kerr, G. S., Díaz Baso, C. J., & Leenaarts, J. 2022, A&A, 665, A50, doi: `10.1051/0004-6361/202243440`

Yamamoto, T. T., Shiota, D., Sakajiri, T., et al. 2002, ApJL, 579, L45, doi: `10.1086/345076`

Yamasaki, D., Inoue, S., Bamba, Y., Lee, J., & Wang, H. 2022, arXiv e-prints, arXiv:2210.14563. `https://arxiv.org/abs/2210.14563`

Yang, H., Chae, J., Lim, E.-K., et al. 2014, ApJL, 790, L4, doi: `10.1088/2041-8205/790/1/L4`

Yashiro, S., & Gopalswamy, N. 2009, in Universal Heliophysical Processes, ed. N. Gopalswamy & D. F. Webb, Vol. 257, 233–243, doi: `10.1017/S1743921309029342`

Yokoyama, T., & Shibata, K. 1996, PASJ, 48, 353, doi: `10.1093/pasj/48.2.353`

Yokoyama, T., & Shibata, K. 1999, in American Institute of Physics Conference Series, Vol. 471, Solar Wind Nine, ed. S. R. Habbal, R. Esser, J. V. Hollweg, & P. A. Isenberg, 61–66, doi: `10.1063/1.58705`

Yurchyshyn, V. B., Goode, P. R., Abramenko, V. I., & Steiner, O. 2011, ApJL, 736, L35, doi: `10.1088/2041-8205/736/2/L35`

Zhang, Y. Z., Shibata, K., Wang, J. X., et al. 2012, ApJ, 750, 16, doi: `10.1088/`
`0004-637X/750/1/16`

Zhukov, A. N., Mierla, M., Auchère, F., et al. 2021, A&A, 656, A35, doi: `10.1051/`
`0004-6361/202141010`

Zirin, H. 1988, Astrophysics of the sun